

530
Q05

7.335

**Optical and magnetic properties of CdO and CdSe
nanoparticles in Pristine and Doped form and of the
combined structure on insertion of CdO
Nanoparticles into nanoporous
freshwater Diatoms**

**A thesis submitted in partial fulfillment of the
requirements for the degree of**

Doctor of Philosophy

Bondita Goswami

Registration number- 003 of 2011



**Department of Physics
School of Science
Napaam, Tezpur-784028
Assam, India**

June 2014

Dedicated

To

My parents

Pradip Ch. Goswami

&

Runu Goswami

ABSTRACT

Nanoparticles show unique, unexpected and divergent optical, electronic and magnetic properties than their bulk form. A bulk material has constant physical properties regardless of its size but at the nanoscale, size dependent properties are observed. Nanoparticles have larger surface to volume ratio compared with the bulk materials which makes them great catalyst. The energy band structure and charge carrier density in the materials can be modified quite differently from their bulk counterpart and in turn will modify the electronic and optical properties of the materials. Now a day, nanoparticles are used in many practical applications for example, fuel cell, catalysis, light emitting devices, phosphors for high definition television, next generation computer chips, elimination of pollutants, sun screen lotion, sensors, biological label, drug delivery etc. Among all other nanoparticles, II-VI semiconductor nanoparticles like CdSe, shows good luminescence properties following quantum confinement effect but does not show magnetic properties. It is an n-type semiconductor. Cadmium oxide (CdO) is also II-VI semiconductor. In the form of nanoparticle, it does not show good optical properties due to its highly non-stoichiometric structure but in pristine form it shows room temperature ferromagnetism. In recent years, extensive research has been focused on CdSe nanoparticles because of their vast technological applications in light-emitting diodes, lasers etc. CdO belongs to the big family of transparent conducting oxides (TCO) like In_2O_3 , SnO_2 , and ZnO etc. TCOs have enormous practical applications in devices in which a transparent contact is required, eg, LEDs, solar cells, LCDs etc. Transition metal doping in CdSe and CdO can bring changes to their optical and magnetic properties. Transition metal 'Manganese' is used as dopant since Mn^{2+} has got many interesting properties in comparison to others. Manganese is remarkable as a luminescent activator. It expands the range of luminescence of the host material. The main aim of the work is to find a material which works both as luminescent as well as magnetic material. Combining basic materials, such as diatom porous silica (DPS) with best suitable semiconductor nanoparticles between the two mentioned above, change in optical properties of DPS is

expected. Also, production of low-cost light emitting materials can be synthesized using DPS which is economically useful and important nowadays.

Chapter I is an introductory chapter that gives brief description on different basic properties of CdSe and CdO nanoparticles as well as of DPS. It shows systematically the importance of different systems on which work has been done, that is, pristine and doped CdSe, CdO nanoparticles and fresh water nanoporous Diatoms, their structure and applications.

Chapter II discusses about the synthesis methods that have been adopted and some very important characterization methods that have been used. Both pristine and doped CdSe and CdO nanoparticles are synthesized by chemical method. Diatoms were collected from a pond and they were cultured using W.C. media. Transmission electron microscopy (TEM) was used to take images of the samples. Energy dispersive X-ray spectroscopy (EDX) was used for elemental analysis. Morphological study was done by X-ray diffraction (XRD). Oxidation states of the elements were tested by electron paramagnetic resonance (EPR) spectroscopy and X-ray photoelectron spectroscopy (XPS). Fourier transform infrared (FTIR) spectroscopy was also done to observe the bonds formed.

Chapter III focuses on pH dependent optical properties and dopant induced changes in optical and magnetic properties of CdSe nanoparticles. CdSe nanoparticles were synthesized by a one pot synthesis method at three different pH levels. They show highest luminescence at pH 11. Manganese was doped into CdSe in diluted amounts that were in 1 %, 2.5 % and 5 % molar concentrations. Electron paramagnetic resonance (EPR) spectra confirm presence of manganese as Mn^{2+} ions. Magnetic properties were studied by superconducting quantum interference device (SQUID).

Chapter IV describes influence of different annealing temperatures and effect of doping manganese on the optical and magnetic properties of CdO nanoparticles. CdO nanoparticles were annealed at three different temperatures; 400 °C, 600 °C and 800 °C. From diffuse reflectance spectra (DRS) and PL spectra, it was found that with increase in temperature cadmium interstitial defects move towards the surface and after receiving

enough energy they get oxidized. So, blue luminescence intensity corresponding to Cd-interstitials decreases with increase in temperature. Number of oxygen vacancies increase with ascending temperature resulting in increase of green luminescence intensity. From SQUID measurements, room temperature ferromagnetism (RTFM) was found whose origin can be assigned to formation of bound magnetic polarons (BMP).

Chapter V is based on discussion about oxygen vacancy generated optical and magnetic properties of CdO nanoparticles. CdO nanoparticles do not show good luminescence properties due to its small band gap. Good luminescence in CdO nanoparticles was realized by annealing them in vacuum environment (760 mm Hg). Annealing in vacuum creates more oxygen vacancies than annealing in air. Increase in oxygen vacancies is responsible for enhanced green photoluminescence in CdO nanoparticles. EPR spectra confirm presence of Cd^+ ions in pure CdO nanoparticles. Origin of RTFM in CdO nanoparticles can be attributed to BMP model.

Chapter VI discusses insertion of nanoparticles in diatom porous silica. Analyzing both CdSe and CdO nanoparticles, it was found that vacuum annealed CdO nanoparticles show enhanced luminescence as well as magnetic properties. Insertion of these nanoparticles into diatom frustule which are made up of porous silica can bring new possibilities of manufacturing devices like low cost light emitting diodes. A simple and cost effective method is proposed to combine DPS with nanoparticles. The combined structure of DPS with CdO nanoparticles shows good luminescence properties as well as good magnetic properties. This kind of combined structure is being studied for the first time.

Chapter VII summarizes the results that have been obtained and also discusses about possible future applications of the work done.

DECLARATION

I hereby declare that the thesis entitled “Optical and magnetic properties of CdO and CdSe nanoparticles in Pristine and Doped form and of the combined structure on insertion of CdO nanoparticles into nanoporous freshwater Diatoms” being submitted to Tezpur University, Tezpur, Assam in partial fulfillment of the requirements of the award of the Degree of Doctor of Philosophy is a record of research work done by me during the Ph.D. course. Any text, figures, theories that are not of own formulated are appropriately referenced in order to give credit to the original author(s). I also declare that the work has not been submitted in part or full for the award of any degree, diploma, fellowship or any other similar title or recognition from any other institute or organization.

Date: 30/06/14

Place: Tezpur University

Bondita Goswami
(Bondita Goswami)

Department of Physics
Tezpur University
Tezpur-784028 (Assam)



TEZPUR UNIVERSITY
(A Central University by an Act of Parliament)
Napaam, Tezpur-784028
DISTRICT: SONITPUR::ASSAM::INDIA

Ph. 03712-273006(O) 9435181498 (M)
Email: ajc@tezu.ernet.in

CERTIFICATE

This is to certify that the thesis entitled “Optical and magnetic properties of CdO and CdSe nanoparticles in Pristine and Doped form and of the combined structure on insertion of CdO nanoparticles into nanoporous freshwater Diatoms” submitted to the School of Science, Tezpur University in partial fulfilment for the award of the Degree of Doctor of Philosophy (Ph.D.) in Physics is a record of research work carried out by Ms. Bondita Goswami under my supervision and guidance.

All helps received by her from various sources have been duly acknowledged.

No part of the thesis has been reproduced elsewhere for award of any other degree.

Date: 24.6.14
Place: TEZPUR UNIVERSITY



Prof. Amarjyoti Choudhury
(Professor)
School of Science
Department of Physics
Tezpur University

TABLE OF CONTENTS

ABSTRACT	i
DECLARATION	iv
CERTIFICATE	v
TABLE OF CONTENTS	vi
LIST OF TABLES	x
LIST OF FIGURES	xi
LIST OF ABBREVIATIONS	xv
LIST OF SYMBOLS	xvi
ACKNOWLEDGEMENT	xvii

Chapter I: Introduction

1.1 Significance of Nanomaterials	1.1
1.2 Wide-bandgap II-VI semiconductor nanoparticles	1.3
1.3 Doping semiconductor nanoparticles	1.4
1.4 Making bifunctional CdSe and CdO nanoparticles	1.5
1.4.1 Pristine CdSe nanoparticles	1.6
1.4.2 The role of ligands in nanoparticle synthesis	1.7
1.4.3 Doping CdSe nanoparticles	1.8
1.4.4 Pristine CdO nanoparticles	1.9
1.4.5 Doping CdO nanoparticles	1.10
1.5 Nanoparticles in natural Porous silica	1.10
1.5.1 Diatom: Natural blue luminescent nanoporous silica	1.11
1.5.2 Insertion of Nanoparticles inside Diatom frustule	1.13
1.6 Objective of the thesis	1.13

Chapter II: Material Synthesis and Characterization Methods	
2.1 Synthesis of pristine and manganese doped CdSe nanoparticles	2.1
2.1.1 Preparation of pristine CdSe nanoparticles by one pot synthesis method using water as solvent	2.1
2.1.2 Preparation of manganese doped CdSe nanoparticles	2.2
2.2 Synthesis of pristine and manganese doped CdO nanoparticles	2.2
2.2.1 Preparation of pristine CdO nanoparticles	2.2
2.2.2 Preparation of manganese doped CdO nanoparticles	2.2
2.3 Transmission electron microscopy (TEM), Selected area electron diffraction (SAED/SAD) and Energy dispersive X-Ray (EDX) studies	2.3
2.3.1 TEM, SAED and EDX study of pristine and manganese doped CdSe nanoparticles	2.5
2.3.2 TEM, SAED and EDX study of pristine and manganese doped CdO nanoparticles	2.6
2.4 X-Ray diffraction studies	2.8
2.5 Fourier Transform Infrared (FTIR) Spectroscopy	2.10
2.6 X-Ray photoelectron spectroscopy study	2.11
2.7 Electron paramagnetic resonance spectroscopy	2.12
Chapter III: Effect of pH and Dopant on Cadmium Selenide Nanoparticles	
3.1 Effect of pH on structural and optical properties of CdSe nanoparticles	3.1
3.2 Effect of dopant on structural and optical properties of CdSe nanoparticles	3.5
3.3 Origin of ferromagnetism in doped CdSe nanoparticles	3.14
3.4 Conclusion	3.17
Chapter IV: Changes in structural, optical & magnetic properties of Cadmium Oxide nanoparticles induced by annealing and doping	
4.1 Enhanced visible luminescence and modification in morphological	

properties of Cadmium Oxide nanoparticles induced by annealing	4.1
4.1.1 Diffuse reflectance spectroscopy	4.1
4.1.2 Photoluminescence (PL) spectroscopy	4.4
4.1.3 X-ray diffraction studies	4.5
4.1.4 I-V measurements	4.7
4.1.5 Hall-effect	4.9
4.2 Optical and Magnetic properties of Manganese doped CdO nanoparticles	4.10
4.2.1 X-Ray diffraction Studies	4.11
4.2.2 Diffuse Reflectance and Photoluminescence spectroscopy of pristine and manganese doped CdO nanoparticles	4.13
4.2.3 Electron paramagnetic resonance spectroscopy (EPR)	4.17
4.2.4 Origin of room temperature ferromagnetism	4.18
4.3 Conclusion	4.20
Chapter V: Enhanced luminescence and realization of ferromagnetism in Vacuum annealed CdO nanoparticles	
5.1 Structural and Morphological Properties of CdO Nanoparticles	5.1
5.2 Study of Diffuse Reflectance spectra and Photoluminescence spectra	5.4
5.3 Electron Paramagnetic resonance study	5.9
5.4 Study of Magnetic properties	5.10
5.5 Conclusion	5.12
Chapter VI: Luminescence and Magnetic properties of Pure Diatom Frustules and Diatom Frustules with inserted CdO Nanoparticles	
6.1 Luminescence properties of nanoporous fresh water Diatom	6.1
6.1.1 Culture of Diatoms	6.2
6.1.2 Structural and Morphological properties	6.3
6.1.3 Optical properties	6.4
6.2. Ferromagnetic CdO nanoparticles inserted in Diatom Frustule	6.8
6.2.1 Structural and Optical properties	6.10

6.2.2 Study of Magnetic property	6.12
6.3. Conclusion	6.12

Chapter VII: Concluding remarks and future directions

7.1 Thesis Conclusion	7.1
7.2 Future direction	7.4

List of publications

LIST OF TABLES

TABLE 3.1: Band gap of pristine and Mn doped CdSe nanoparticles	3.7
TABLE 3.2: Comparison table of crystallite size and strain for doped and undoped samples	3.9
TABLE 4.1: Comparison of direct band gap, indirect band gap and Urbach energy	4.3
TABLE 4.2: Comparison between lattice constant, interplanar spacing, crystallite size & Strain	4.7
TABLE 4.4: Hall co-efficient and charge density of the samples	4.10
TABLE 4.5: Comparison of crystallite size, strain, interplanar distance and lattice constant	4.13
TABLE 4.6: Table for bandgap and Urbach energy of pristine and Mn doped CdO nanoparticles	4.16
TABLE 5.1: Comparison of crystallite size, strain, interplanar spacing and lattice constant of CdO nanoparticles	5.3
TABLE 5.2: Urbach energy and band gap of CdO nanoparticles	5.6

LIST OF FIGURES

Figures	Page No.
Figure 1.1: Electronic density of states of 0D, 1D, 2D and 3D nanostructures	1.3
Figure 1.2: HOMO-LUMO electronic transition	1.4
Figure 3: Zinc blende CdSe nanoparticles	1.6
Figure 4: Cubic rocksalt structure of CdO nanoparticles	1.9
Figure 5: Schematic diagram of (A) Centric and (B) Pennate diatoms	1.11
Figure 2.1: Ray diagram of TEM	2.3
Figure 2.2: Principle of EDX	2.4
Figure 2.3: (A) HR-TEM, (B) EDX and (C) particle size calculation of CdSe nanoparticles	2.5
Figure 2.4: (A) Interplanar spacing and (B) SAED of CdSe nanoparticles	2.6
Figure 2.5: (A) HR-TEM, (B) particle size calculation, (C) EDX of Mn doped CdSe nanoparticles	2.6
Figure 2.6: (A) HR-TEM image, (B) EDX and (C) SAED of CdO nanoparticles	2.7
Figure 2.7: (A) HR-TEM, (B) SAED and (C) EDX of Mn doped CdO nanoparticles	2.7
Figure 2.8: XRD and W-H plot of CdSe nanoparticles	2.9
Figure 2.9: XRD and W-H plot for CdO nanoparticles	2.9
Figure 2.10: FTIR spectra of CdSe nanoparticles before and after dispersion in water	2.10
Figure 2.11: FTIR spectroscopy of CdO nanoparticles	2.11
Figure 2.12: XPS of CdO nanoparticles	2.12
Figure 2.13: EPR spectroscopy of CdO nanoparticles	2.13
Figure 3.1: XRD of the synthesized nanoparticles	3.1
Figure 3.2: Williamson-Hall plot of CdSe nanoparticles	3.2
Figure 3.3: UV-Vis absorption spectra	3.2
Figure 3.4: Tauc's plot of the CdSe samples at different pH	3.3
Figure 3.5: PL spectra of CdSe nanoparticles prepared in different pH	3.3
Figure 3.6: FTIR spectra of the CdSe nanoparticles prepared in pH 8, 9, 10 & 11	3.4
Figure 3.7: Diffuse reflectance spectra of pristine and doped CdSe nanoparticles	3.6
Figure 3.8: Band gap calculation of pristine and doped CdSe nanoparticles	3.6

Figure 3.9: XRD pattern of pristine and doped CdSe nanoparticles	3.8
Figure 3.10: Williamson-Hall plot for pristine and doped CdSe nanoparticles	3.8
Figure 3.11: PL spectra of pristine and doped CdSe nanoparticle	3.10
Figure 3.12: Schematic diagram of the splitting excited states of $3d^5$ level for a Mn^{2+} ion in presence of a tetrahedral crystal field	3.10
Figure 3.13: Scenarios of PL emission in different nanoparticles	3.11
Figure 3.14: PL emission in Mn doped CdSe dependent upon size of the nanocrystal	3.12
Figure 3.15: Raman spectra of Mn doped CdSe nanoparticles	3.13
Figure 3.16: EPR spectra of Mn doped CdSe nanoparticles	3.14
Figure 3.17: M-H curves for Mn doped CdSe nanoparticles	3.15
Figure 3.18: Zoomed image of M-H curves of Mn doped CdSe nanoparticles	3.16
Figure 4.1: Diffuse reflectance spectra of CdO nanoparticles annealed at three different temperatures	4.1
Figure 4.2 (a): Tauc's plot for determination of direct band gap of CdO nanoparticles	4.2
Figure 4.2 (b): Tauc's plot for determination of indirect band gap of CdO nanoparticles	4.2
Figure 4.3: $\ln [F(R)]$ versus incident photon energy $h\nu$ for CdO nanoparticles annealed at three different temperatures	4.3
Figure 4.4: (A) PL spectroscopy of CdO nanoparticle and (B) Comparison of PL spectra of CdO nanoparticles annealed at three different temperatures	4.4
Figure 4.5: XRD pattern of CdO nanoparticles annealed at different temperatures	4.5
Figure 4.6: Williamson-Hall plot of all three CdO nanoparticle samples annealed at different temperatures	4.6
Figure 4.7: Lattice constant vs NRF of CdO nanoparticles	4.6
Figure 4.8: Current vs Voltage plot of CdO nanoparticles	4.8
Figure 4.9: Schematic diagram of Hall-effect	4.9
Figure 4.10: Hall Voltage vs Magnetic field of all three CdO nanoparticle samples	4.9
Figure 4.11: Comparison of X-ray diffraction studies	4.11
Figure 4.12: Williamson-Hall plot of pristine and Mn doped CdO nanoparticles	4.12
Figure 4.13: Nelson-Riley plot of pristine and Mn doped CdO nanoparticles	4.12
Figure 4.14: Diffuse reflectance spectra of pristine and Mn doped CdO nanoparticles	4.14

Figure 4.15: Tauc's plot for pristine and Mn doped CdO nanoparticles	4.14
Figure 4.16: Urbach energy plot for pristine and Mn doped CdO nanoparticles	4.16
Figure 4.17: Normalized PL spectra of pristine and Mn doped CdO nanoparticles	4.16
Figure 4.18: EPR spectra of pristine and Mn doped CdO nanoparticles	4.18
Figure 4.19: Magnetization curve of pristine and Mn doped CdO nanoparticles	4.19
Figure 5.1: (A) HR-TEM of CdO nanoparticle, (B) SAED of CdO nanoparticle, (C) Lattice plane spacing of CdO nanoparticles	5.1
Figure 5.2: EDX spectrum of CdO nanoparticles	5.1
Figure 5.3: XRD spectra of CdO nanoparticles	5.2
Figure 5.4: (A) & (B) W-H plot and (C) & (D) NRF plot of air and vacuum annealed samples	5.3
Figure 5.5: Comparison of DRS of CdO nanoparticles annealed in air and vacuum	5.4
Figure 5.6: Tauc's plot for calculation of direct band gap of (A) air annealed and (B) vacuum annealed CdO nanoparticles, & indirect band gap of (C) air annealed, (D) vacuum annealed CdO nanoparticles	5.5
Figure 5.7: Urbach energy plot for (A) Air annealed CdO and (B) Vacuum annealed CdO nanoparticles	5.6
Figure 5.8: PL spectra of air and vacuum annealed CdO nanoparticles	5.7
Figure 5.9: Raman spectra of CdO nanoparticles annealed in air and vacuum	5.8
Figure 5.10: EPR spectra of Mn doped CdO nanoparticles	5.9
Figure 5.11: Comparison of M-H curves of CdO nanoparticle annealed in air and vacuum	5.10
Figure 6.1: Images of fresh water Diatom taken by Optical microscope	6.1
Figure 6.2: (A) SEM pictures of Cyclotella Meneghiniana of fresh water diatom, (B) , EDX of the same species, (C) Histogram of pore size distribution	6.3
Figure 6.3: XRD pattern of diatom Cyclotella Meneghiniana frustules	6.4
Figure 6.4: UV-Vis absorption spectroscopy of Diatom Cyclotella Meneghiniana frustules	6.4
Figure 6.5: PL spectra of Diatom Cyclotella Meneghiniana frustules	6.5
Figure 6.6: PL peak position for different excitations	6.6
Figure 6.7: PLE spectra of Diatom Cyclotella Meneghiniana	6.7

Figure 6.8: PL decay curves corresponding to emission wavelength 330 nm along with instrumental response function	6.8
Figure 6.9: TEM image of Diatom frustules with CdO nanoparticles	6.9
Figure 6.10: UV-Vis absorption Spectra of Diatom Frustules with and without CdO nanoparticles	6.10
Figure 6.11: Comparison of PL spectra of Diatom Frustules with and without CdO nanoparticles	6.11
Figure 6.12: M-H curve for Pure Diatom frustules and Diatom frustules with CdO nanoparticles	6.12

List of abbreviations

HR-TEM	High –resolution transmission electron microscope
TEM	Transmission electron microscope
SAED	Selected area electron diffraction
EDX	Energy dispersive X-ray spectroscopy
XRD	X-ray diffraction
FTIR	Fourier transform infrared spectroscopy
PL	Photoluminescence
DRS	Diffuse reflectance spectroscopy
TRPL	Time resolved photoluminescence
UV	Ultraviolet
Vis	Visible
IR	Infrared
XPS	X-ray photoelectron spectroscopy
EPR	Electron paramagnetic resonance
DPS	Diatom porous silica
PS	Porous silicon
QD	Quantum dot
LED	Light-emitting diode
DMS	Diluted magnetic semiconductor
NP	Nanoparticle
BMP	Bound magnetic polaron
FE	Free exciton
STE	Self-trapped exciton
SQUID	Superconducting quantum interference device
JCPDS	Joint committee for powder diffraction software
RKKY	Rudermann-Kittel-Kasuya-Yosida
TGA	Thioglycolic acid
TCO	Transparent conducting oxide
RTFM	Room temperature ferromagnetism

LIST OF SYMBOLS

eV	Electron volt
π	Pi
T	Temperature
K	Kelvin
a_{β}	Exciton Bohr radius
m^*	Effective mass of polaron
M	Effective mass of electron
C	Celsius
λ	Wavelength
pm	Picometer
nm	Nanometer
Oe	Oersted
θ	Diffraction angle
kV	Kilovolt
Å	Angstrom
h	Planck's constant

ACKNOWLEDGEMENT

This thesis is incomplete without mentioning names of those people whose support, advice, encouragement and companionship helped me accomplishing the work presented in the thesis. Foremost, I would like to express my sincere gratitude to my supervisor Prof. Amarjyoti Choudhury for his continuous support during my Ph.D. work. His guidance helped me during the research and writing of this thesis. I thank him for his confidence on me that helped me materializing the works presented in the thesis. I could not have imagined having a better advisor and mentor for my Ph.D study.

Besides my advisor, I would like to thank Dr. D. Mohanta and Dr. P. Deb for their encouragement, insightful comments throughout my Ph.D. period. I am also indebted to all the faculty members of Department of Physics for their inspiration. I also like to extend my thanks and gratitude to Prof. A. K. Buragohain, vice-chancellor Dibrugarh University and Department of M.B.B.T. for helping me during initial days of research work.

I would also like to acknowledge Department of Science and Technology (DST) for providing me the fellowship through the project SR/NM/NS-98/2010 (G). I like to acknowledge some instrumentation centres where I carried out a lot of my characterizations. First and foremost I would like to thank SAIF IIT Bombay, SAIF IIT Madras, CRF IIT Kharagpur, SAIF IIT Guwahati and SAIF NEHU for helping me in carrying out EPR, TRPL, SQUID and HR-TEM. I like to thank SAIC, Tezpur University and all the technical staff of Tezpur University without their help in different characterizations; this thesis would not have been completed.

I thank my fellow lab-mates Biswajit, Priyanka, Susmita and Pawan for their stimulating discussions on research and for all the fun we have had in the last five years. I would also like to thank Sikha, Sayan, Anoop, Prarthana, Anisha, Madhulekha, Kalpana, Deepak and Nibedita for being so good friend of mine and enlightening my mind during bad days. I like to thank Upamanyu, Runjun, Saurav, Nomita, Prakash, Madhurya, Jyoti, Ratan,

Anshuman, Somik, Kunal, Subasit, Nabanita, Smriti, Swati, Manasi, Nilakshi, Dhruvajyoti, Ranjan, Ankur, Koushik, Samiran, Manjit, Namita, Monalisa, Nilima, Shyamalima and Momina for your help, support and well wishes which I needed most during my Ph.D. period.

Most importantly, nothing would have been possible without the love, encouragement, support and patience of my parents. Without their faith on me I could not have done Ph.D. My thesis is solely dedicated to my mother, who has been a constant source of love, friendship, happiness for me and my father, whose inspiration, care, support, strength and guidance made me believe in myself. I would like to express my heart-felt gratitude to my elder sister Nabanita and rest of the family members. I thank God for bringing two angels Ashi and Nishi into my life through my sister. They have been constant source of joy in my life. And last but not the least I would like to thank my husband Dhruva for his constant support, encouragement and love.

Date: 30/06/14

Bondita Goswami
(Bondita Goswami)

Chapter I: Introduction

1.1 Significance of Nanomaterials

"There's Plenty of Room at the Bottom" was the talk given by Richard Feynman at an American Physical Society meeting at Caltech on December 29, 1959 [1]. Feynman believed the possibility of direct manipulation of individual atoms to be a very powerful concept. The content of the talk soon emerged as inspiration for conceptual beginning of nanotechnology. The history of nanotechnology started and developed through the synergy of the concepts and experimental work hand in hand. Although nanotechnology is a relatively recent development in scientific research, the development of its main concepts occurred over a longer period of time [2]. The development of nanotechnology in the 1980s was caused by the experimental advances such as the invention of the scanning tunneling microscope in 1981 [3] and discovery of fullerenes in 1985 [4]. The field of nanotechnology was subject to growing public awareness and controversies in the early 2000s when the first commercial applications were started [5]. Nanoparticles are of great scientific interest as they form a bridge between bulk materials and atomic or molecular structures. A bulk material should have constant physical properties regardless of its size but at the nanoscale, size dependent properties are observed. The word nano stems from the Greek word "nanos" which means dwarf [6]. Nanoparticles are ultrafine particles in the size range of nanometer range from 1 nm to 100 nm. In the narrower sense, these are the particles whose size range is 10-20 nm. Nanoparticles include fullerenes, metal clusters, large molecules such as proteins and even hydrogen bonded water molecules, which exist at ambient temperatures. They are very common in the physical world, for example, proteins exist in almost all biological systems. In describing nanostructures it is necessary to differentiate between the numbers of dimensions in the nanoscale. Nanostructures are classified into three categories: zero dimensional, one dimensional and two dimensional [7]. Materials wherein all dimensions are measured within the nanoscale are called zero dimensional nanoparticles. Spherical nanoparticles have three dimensions on the nanoscale, i.e., the particle is between 0.1 and 100 nm in each spatial dimension. Quantum dots are characterized by zero dimensionality. In one dimensional nanostructure, one dimension is outside the nanoscale. Nanotubes have two dimensions on the nanoscale, i.e., the diameter of the tube is between 0.1 and 100 nm; its length could be much greater. In two

Chapter I

dimensional nanostructures, two of the dimensions are not confined to nanoscale. Nanotextured surfaces have one dimension on the nanoscale, i.e., only the thickness of the surface of an object is between 0.1 and 100 nm.

One of the direct consequences of reducing size of materials to the nanometer range is the appearance of quantization effect due to confinement of the movement of electrons [8]. This leads to discrete energy levels depending on the size of the structure. In a semiconductor crystallite whose diameter is smaller than the size of its exciton Bohr radius, the excitons are squeezed, leading to quantum confinement. The energy levels can be modeled using particle in a box model in which the energy of different states is dependent upon length of the box. Quantum dots are said to be in weak confinement regime if their radii are on the order of exciton Bohr radius and quantum dots are said to be in strong confinement regime if their radii are smaller than the exciton Bohr radius. Quantum confinement effect in nanoparticles leads to quantization of energy states which relates to the fact that spacing between energy levels of electron states in atoms increases in inverse proportion to the square of nanoparticle size [9]. This gives rise to discrete energy levels instead of denser set of the levels commonly found in bulk materials. As the particle size becomes smaller, their surface to volume (S/V) ratio increases dramatically [10]. This is very interesting property of nanoparticles. High surface area means it has greater number of reaction sites than a particle with low surface area. High S/V in nanoparticles also provides tremendous driving force for diffusion and reduces the initial melting temperature. The density of states (DOS) refers to the number of quantum states per unit energy [11]. In other words, the density of states indicates how densely quantum states in a particular system are packed. For quantum wires, the DOS for certain energies actually becomes higher than the DOS for bulk semiconductors, and for quantum dots the electrons become quantized to certain energies as shown in Figure 1.1.

There are two design approaches in nanotechnology [12]. In top-down approach, nano-scale objects are made by processing larger objects in size. In some applications, larger scale materials are ground to the nanometer scale to increase the surface to volume ratio to enhance reactivity. Bottom-up approach in nanotechnology deals with making larger nanostructures from smaller building blocks such as atoms and molecules. Manufacturing of carbon Nanotubes using metal catalyzed polymerization method is a good example for bottom-up approach.

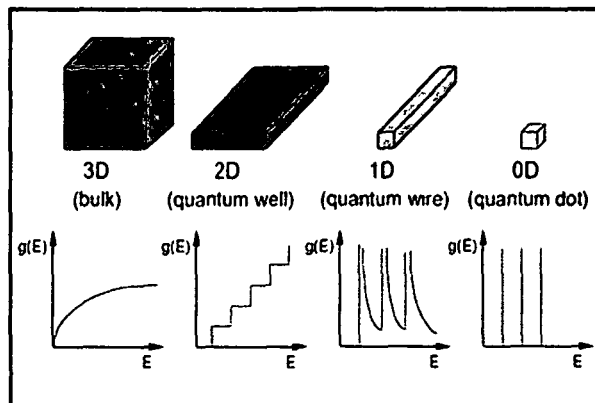


Figure 1.1: Electronic density of states of 0D, 1D, 2D and 3D nanostructures

1.2 Wide-bandgap II-VI semiconductor nanoparticles

Wide-bandgap semiconductors are semiconductor materials with electronic band gaps significantly larger than one electronvolt (eV) [13]. "Wide" bandgap usually refers to material with a band gap significantly greater than that of the commonly used semiconductors, for example Silicon (1.1 eV) or Gallium Arsenide (1.4 eV). Wide bandgap materials have several characteristics that make them beneficial compared to lower bandgap materials. Devices made up of higher bandgap materials give the ability to operate at higher temperatures, and for some applications, these devices can operate at larger voltages. The optical response of a semiconductor is critically controlled by its bandgap energy which gives the threshold energy for an electronic transition from the valence band to the conduction band. In molecular terms, such a transition would be analogous to the lowest energy electronic transition wherein an electron in the highest occupied molecular orbital (HOMO) is promoted to the lowest unoccupied molecular orbital (LUMO) [14]. Let us consider a very simple electronic system consisting of two levels, the ground state (the state before absorption) and the excited state (the state after the system absorbs the photon) then the HOMO-LUMO electronic transition will be like that shown in Figure 1.2.

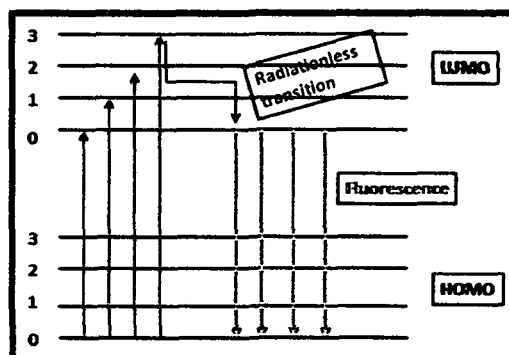


Figure 1.2: HOMO-LUMO electronic transition

Electronic transition energy in wide band gap materials fall in the energy of visible light, and hence light-emitting devices such as light-emitting diodes (LEDs) and semiconductor lasers can be made with wide bandgap materials that emit light in the visible spectrum, or even produce ultraviolet emission. There are many III–V and II–VI compound semiconductors with high bandgaps. II–VI compounds are the compounds formed from the elements of group II and VI of the periodic table. These are the sulphides, selenides, tellurides and oxides of zinc, cadmium, mercury and alkaline earth elements (e.g. beryllium, calcium, barium, magnesium and strontium) [15]. Most group II-VI materials are direct band gap semiconductors with high optical absorption and emission coefficients. Wide band gap II-VI compounds have been applied to optoelectronic devices, especially light emitting diodes in the short wavelength region of visible light.

1.3 Doping semiconductor nanoparticles

The intentional introduction of impurities into a material was done to control the fundamental properties of bulk semiconductors [16]. This has stimulated similar efforts to dope semiconductor nanocrystals. Dopants in nanocrystals lead to a phenomena that was not found in the bulk because in nanoscale, electronic states are

Chapter I

confined to a small volume. For example, n or p-type dopants can auto-ionize without thermal activation. This occurs because a carrier inside the crystallite must occupy one of the confined electronic states, which increase in energy with decreasing nanocrystal size. Below a critical radius, the confinement energy exceeds the Coulomb interaction between the ionized impurity and the carrier, which then automatically occupies a nanocrystal state [17]. The incorporation of dopants in semiconductor nanoparticles to control their behavior brought out many new technologies from nanoparticles. Research has been going on to investigate how incorporation of dopants can influence semiconductor nanocrystallites of a few nanometers in scale with size-dependent optical and electronic behavior. Impurities can strongly modify electronic, optical, and magnetic properties of bulk semiconductors but to witness the changes in nano scale is a new challenge.

One of the most interesting categories of dopants in semiconductors is that of magnetic ions. Semiconductors containing magnetic impurities have been studied for several decades [18]. Interest in these type of materials originally arose from the so-called “giant Zeeman effects”. Zeeman splitting of these magnetic ions doped semiconductors exceeds the splitting of the corresponding nonmagnetic semiconductors by over two orders of magnitude giving possible applications in optical gating. Recently, interest in these materials has turned toward their applications in spin-based electronic technologies, or “spintronics”. In spintronics, the giant Zeeman splitting is used to generate spin-determined conductivity channels in semiconductors [19].

An important category of dopants for semiconductor nanocrystals is luminescence activators [20]. Luminescent properties of pure semiconductor nanocrystals have driven much of the research interest recently. Manipulation of the luminescent properties of these nanocrystals by doping with ions such as Mn^{2+} or Eu^{2+} has the potential to expand the range of useful spectroscopic properties that can be achieved from this class of materials [21,22]. When a macroscopic semiconductor crystal is grown under conditions of thermal equilibrium, impurity atoms can be incorporated up to their solid solubility limit as much as 50% or more for Mn in II–VI semiconductors. This thermodynamic limit is completely determined by the Gibbs

Chapter I

free energy (approximately equal to the impurity formation energy) and the growth temperature.

1.3 Making bifunctional CdSe and CdO nanoparticles

CdSe nanoparticles exhibit good luminescence properties and CdO nanoparticles show good magnetic properties even without doping by any magnetic element. They both belong to the II-VI binary semiconductor group. For many practical applications semiconductor materials are needed which have both good luminescent and magnetic properties and in other words bifunctional materials. So by doping suitable impurity into these materials one can expect simultaneous exhibition of luminescence and magnetism in these otherwise single functional materials. CdSe is chosen as it shows only good luminescence and by incorporating manganese ions into it, luminescence and magnetic properties of this material will be studied. Again, CdO shows good magnetic properties in its pristine form. So, by doping manganese, good luminescence as well as magnetic property in the host material is expected.

1.4.1 Pristine CdSe nanoparticles

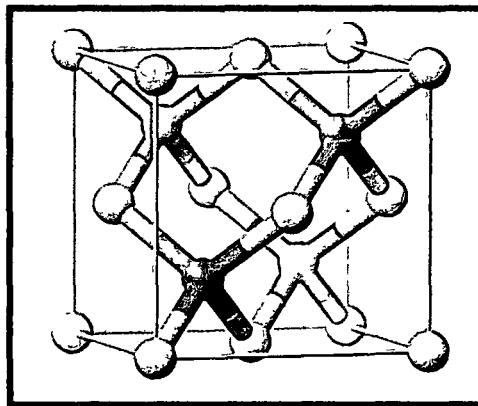


Figure 1.3: Zinc blende CdSe nanoparticles (Ref 25)

CdSe is an II-VI binary semiconductor having bulk band gap of 1.76 eV [23]. Size can be used as a variable in tailoring the desired properties of the nano scale system and this has made nanoparticles potentially strong materials. The size of such nanoparticles can be changed to tune the optical gap across a major portion of the visible spectrum. For example, in the case of CdSe nanoparticles, the optical gap can be tuned from deep red to green by reducing the nanoparticle diameter from 20 to 2 nm in accordance with quantum confinement effect [23,24]. Figure 1.3 shows Zinc blende CdSe [25]. In recent years, extensive research has been focused on Cadmium Selenide (CdSe) nanoparticles because of their vast technological applications in light-emitting diodes, lasers etc [26]. The absorbance and photoluminescence spectra of nanoparticles also allow them to act as wavelength conversion materials for light emitting diodes. Nanoparticles absorb light of wavelengths shorter than their absorbance edge and then emit light at their luminescence peak wavelength [27]. Commercially available gallium nitride (GaN, $\lambda=425$ nm) blue LEDs provide a convenient excitation source that can be converted to any wavelength in the visible spectrum using appropriately designed CdSe nanoparticles. Recently, researchers have considered using the wavelength conversion properties of nanoparticles for solid-state white lighting. Here the goal is to produce color-balanced white light with the highest possible energy efficiency and the lowest possible cost. One approach is to surround a blue LED with a quantum dot (QD) nanoparticle polymer composite that converts some of the blue light to yellow light so that the human eye perceives the emission as white light [28]. Theoretically, quantum dot nanoparticle lasers offer high prospective of better performance than bulk semiconductor lasers or quantum well lasers. In small, strongly confined quantum dot nanoparticles, the separation between energy states is greater than the thermal carrier energies, inhibiting thermal depopulation of the lowest, 'emitting' transition and resulting in a low, temperature-insensitive optical-gain threshold, a narrow emission line, and high-temperature stability [29]. CdSe quantum dot nanoparticles are commercially available to fill a growing demand in the field of biomedical imaging [30]. Conjugation of QDs with antibodies yields biomarkers. These biomarkers compete with traditional organic fluorescent tags in terms of biocompatibility, filtering simplicity, and photo-stability [31]. Focusing on the fact that QDs have narrow emission width, researchers are developing new emitters for applications that require carefully controlled color. One such application is the animated billboards on buildings and in sports arenas [32].

These large color displays contain millions of light emitting diodes (LEDs). The intensities of red, green, and blue LEDs are tuned to produce a color image. The cost of such displays could be reduced if discrete LEDs could be replaced by polymer films containing quantum dots with different emission wavelengths.

1.4.2 The role of ligands in nanoparticle synthesis

Highly luminescent II-VI nanocrystals (CdS/CdSe/CdTe) have been of great interest for fundamental research. These nanocrystals are metastable species in comparison to the corresponding bulk crystals and have to be stabilized. The most common method to keep them stable is chemically attaching a monolayer of organic molecules to the atoms on the surface of nanocrystals. These are called surfactant/ligand/capping agent [33,34]. Ligands play important roles in the stability and solubility of the nanoparticles. Ligands stabilize growth of the nanoparticles during synthesis to prevent aggregation and precipitation. These capping ligands also affect electronic and optical properties of nanoparticles by passivating dangling bonds on nanoparticle surface. The density of the ligands on the surface and the length of the ligand chain affect the separation between nanocrystal surface and cores. In order to investigate unique properties of the nanoparticles surface, understanding the ligand behavior on the quantum dot surface is required. Thiols are probably the most utilized ligands for stabilizing semiconductor [35]. Thiols form an important class of capping molecules and these with a polar head group are used to synthesize water soluble QDs that can serve as biological labels [36].

1.4.3 Doping CdSe nanoparticles

Doping can bring changes to the optical, electronic and magnetic properties of pristine nanoparticles. For magnetic dopants, confinement of the impurity within the nanocrystal can enhance its interactions with other carriers or quantum mechanical spins. Interesting consequences can be seen which include individual doped nanocrystals that behave as spin filters [37]. Carriers whose spins are aligned one way are conducted preferentially, while others are blocked. Major efforts have been given to the use of CdSe nanocrystals as the host material for doping transition metal ions to

synthesize a material with spintronics applications. Among the II-VI semiconductor materials such as CdS, ZnS, and ZnSe, manganese doping into CdSe nanocrystals is very difficult and controversial due to a process called “self-purification” [38]. Specifically, Manganese (Mn^{2+}) has a tendency to be expelled to the CdSe nanocrystal surface. Manganese is incorporated inside the CdSe nanoparticles in order to obtain high quality Diluted Magnetic Semiconductor (DMS) nanocrystals for use in spin electronics and quantum information technology [39]. In the Mn^{2+} -doped II-VI semiconductor nanostructures, an sp-d exchange interaction takes place between the electron/hole band states of the semiconductors and the Mn^{2+} $3d^5$ electron states, whereby Mn^{2+} acts as a paramagnetic center ($S=5/2$) [40]. From the practical application point of view, Cd-based nanostructures, especially CdSe, are highly toxic to biological tissue. Hence, to make them biocompatible and water-soluble, various surface modifications have been tried such as coating them with Thioglycolic acid, mercaptopropionic acid, polymers, and silica [41].

1.4.4 Pristine CdO nanoparticles

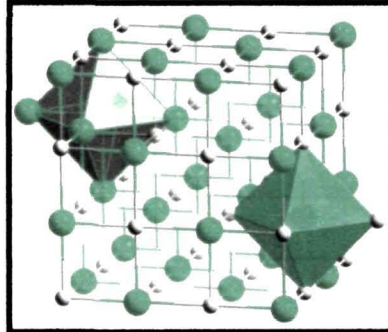


Figure 1.4: Cubic rocksalt structure of CdO nanoparticles (Ref 44)

Synthesis of binary II-VI semiconductor is a growing area of research nowadays because of their chemical, physical, optical and electrical properties. These semiconductors as zero dimensional nanoparticles are especially interesting due to their increased surface to volume ratio for which they gain size dependent optical properties. Pure bulk Cadmium Oxide (CdO) is n-type semiconductor with a direct band of 2.5 eV and an indirect band gap of 1.98 eV [42,43]. CdO is IIB-VI compound semiconductor. It adopts face-centred-cubic rocksalt structure where Cd is

octahedrally co-ordinated to its neighbors (shown in Figure 1.4 [44]). CdO has widely used applications like the preparation of cadmium coated baths and manufacture of paint, pigments etc [45]. It belongs to the big family of transparent conducting oxides (TCO) like In_2O_3 , SnO_2 , and ZnO etc. TCOs have enormous practical applications in devices in which a transparent contact is required, eg, LEDs, solar cells, LCDs etc [46]. Besides, CdO shows very high electrical conductivity even without doping due to the existence of shallow donors caused by intrinsic interstitial cadmium atoms and oxygen vacancies [47]. Most common TCOs in such applications is Sn doped In_2O_3 [48]. Since In is very costly and scarce material hence scientists are focusing their research in finding alternating material. CdO is such a capable alternate material. Badeker was the first to report CdO as transparent conducting films long back in 1990, yet it has not been extensively studied compared to other oxides like Tin dioxide (SnO_2), Zinc oxide (ZnO) and Indium oxide (In_2O_3) due to its relatively small band gap. CdO films are transparent in visible region of electromagnetic spectrum. CdO has many applications due to its low Ohmic resistivity and high optical transparency [49]. But so far it has been confined in making films. Exploring structural and optical properties of CdO nanostructures are new promising field for researchers.

1.4.5 Doping CdO nanoparticles

CdO has been identified as a latent candidate for host material for the realization of Dilute Magnetic semiconductor (DMSs) due to the prediction of possible ferromagnetism in CdO [50]. Recently, it has also been predicted that the ferromagnetism in this class of oxides can be induced by native defects, bringing new challenges for understanding the origin of ferromagnetism in these oxide compounds [51]. In previous studies, the synthesis of Sn-doped CdO thin films [52], Bi^{3+} -doped CdO thin films by sol-gel spin coating method [53], copper-doped CdO nanostructures [54], ZnO-doped CdO materials [55], titanium-doped CdO thin films [56], ZnO-CdO- TeO_2 system doped with the Tb^{3+} and Yb^{3+} ions [57], N-doped CdO [58], Samarium-, Cerium-, Europium-, Fe-, and Li-doped CdO nanocrystalline materials [59-63], In-doped CdO films [64], Fluorine- doped CdO [65], Gallium-doped CdO thin films [66], Gd-doped CdO thin films with different method, dopant amount and structural morphology [67], Li-Ni co-doped CdO thin films [68],

Aluminum-doped CdO thin films [69], Mn doped CdO nanoparticles [70], Ni-doped CdO nanoparticles [71] have been reported.

1.5 Nanoparticles in natural porous silica

Diatoms are algae whose shell is made up of porous silica which was synthesized by Diatoms themselves. Synthesis of porous silica by chemical route is a very tedious and hard job. So using this porous silica from the nature and harnessing it in the use of practical applications would be an interesting work. Porous silica has its own significant luminescence properties. After insertion of bifunctional nanoparticles like manganese doped CdSe and CdO nanoparticles can bring changes into its properties. Combined system of nanoparticles inserted into silica has many practical applications for example, synthesis of low cost light emitting materials.

1.5.1 Diatom: Natural blue luminescent nanoporous silica

Diatoms are unicellular, eukaryotic, photosynthetic algae that are found in various environments including both fresh and marine water. These are 1–500 μm in length with characteristic rigid cell walls (frustules) composed of silica. These organisms are found in a wide variety of habitats and are thought to be responsible for up to 25 % of the world's net primary production of organic carbon [72]. Diatoms may be divided into two major groups based on valve symmetry; those that are circular with essentially radial symmetry, the centric diatoms (Figure 1.5 (A)), and those that are more elongate, with primarily bilateral symmetry, the pennate diatoms (Figure 1.5 (B)) [73,74]. Or simply it can be said that centric diatoms are radially symmetrical, while pennate diatoms are elongated.

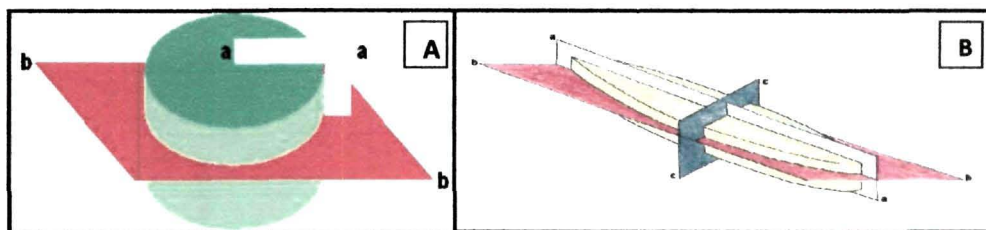


Figure 1.5: Schematic diagram of (A) Centric and (B) Pennate diatoms (Ref 73,74)

Chapter I

There are currently estimated to be over 1, 00,000 different species, classified by their unique frustule morphologies [75]. Diatoms have enormous ecological importance on this planet and each of the species has different patterns and structures. Diatom nanotechnology, an upcoming interdisciplinary area, has deep relation with biology, biochemistry, biotechnology, physics, chemistry, material science and engineering. The photonic crystal properties of diatoms' girdle band structures were already discovered which states that diatoms are living photonic crystals [76-78]. This discovery leads to a new area of research in Diatoms and their practical applications. Diatom frustule offers mechanical protection which has been tested by measuring the force necessary to break single cells [79]. Differences in the force at the frustule-crashing time were observed among different species. It was found that small cells require higher mechanical strength to break the frustule. Such high strength of the frustule is thought to result from its architecture, and specifically from the presence of ribs or pores that can dissipate the mechanical forces. A computational method called finite-element analysis, confirmed the importance of the ribs [80]. New methods of designing materials combining micro- (from zeolite), meso- and macroporosity (from the frustule) are under research. For example, diatom frustules were recently used as a substrate for the deposition of a zeolite layer by a vapor phase transport method. Shape-preserving conservation routes were also successfully used to change, by means of a two-step process, diatom ceramic into anatase TiO_2 or BaTiO_3 [81]. Diatom frustule has light focusing ability [82]. The discovery of the *C. Walesii* focusing features really opened new opportunities in the field of microlenses and of diatom nanotechnology. Diatom based microlenses could be more flexible than those fabricated with usual technologies. This is because of the intrinsic properties of their frustules. Silicon atoms of Diatom frustule can be substituted with other species without losing the structure [83]. These low cost, biological nanophotonic structures display versatile morphologies and may have potential applications in solar cells [84], photoluminescence based biosensors [85], drug delivery systems [86], selective membranes [87]. Diatom frustules have been used as templates for fabricating metallic nano-structures including the deposition of gold (Au) and silver (Ag) coatings onto diatom frustules via self-supported gold microstructures with complex three-dimensional (3-D) morphologies using electrodeless deposition [88,89]. These nanoporous silica frustules show very good luminescence properties when irradiated with ultra violet light [90]. From the application point of view, this makes these

Chapter I

natural nanoporous silica structures very favorable candidate for opto-electronic applications [91].

1.5.2 Insertion of Nanoparticles inside Diatom frustule

Diatom frustules have nano pores of silica. Suitably inserting nanoparticles inside Diatom frustule and investigating the optical and magnetic properties of the combined structure would be an interesting piece of work. Researchers are trying hard to make nanoporous silica structures till date by various methods. But such structures are abundant in nature itself and are easily available in sea and fresh water. Porous silica containing nanoparticles are especially important because of their numerous practical applications. The combined structure shows modified optical properties. Magnetic properties of such structures have not investigated so far.

1.6 Objective of the thesis

Combining basic materials, such as diatom porous silica (DPS) with semiconductor nanoparticles, one can change optical properties of DPS and it enables producing low-cost light emitting materials, which is economically useful and important nowadays [92]. DPS can be harnessed as a propitious natural material for application in luminescent devices and is also abundant in nature. So, low cost luminescent device can be fabricated by using nanoparticles inserted in DPS. Inserting the best suitable nanoparticle (pristine/doped) into DPS to see the photoluminescence and magnetic behavior is the main objective of our thesis. CdSe is a good luminescent material but does not show magnetic properties in its pristine form and when non-magnetic element manganese is doped into it, changes in the optical and magnetic properties of CdSe are expected. Mn²⁺ doping in CdSe is a challenge for the researchers, yet it has been selected as dopant since Mn²⁺ has got many interesting properties in comparison to others. It is remarkable as a luminescent activator. It expands the range of luminescence of the host material. Studying the magnetic properties of the combined system will also be interesting. Again, CdO which is known as a good, in fact, first

Chapter I

discovered transparent conducting oxide does not show good luminescence properties. When manganese is doped into CdO, both good magnetic and optical properties are expected to be incurred in the same host material. In short, finding one nanoparticle which works both as luminescent as well as magnetic material is one aim of our thesis. And to incorporate that nanoparticle into DPS to get better luminescent and magnetic property of the combined structure is the main objective as mentioned earlier.

References:

1. Schiller, J. *Nanotechnology Development: Using Research from the Internet*, Create Space, USA, 2010.
2. [HTTP://WWW.NOBELPRIZE.ORG/NOBEL_PRIZES/PHYSICS/LAUREATES/1986/](http://www.nobelprize.org/nobel_prizes/physics/laureates/1986/)
3. Kroto, H.W. C₆₀: Buckminsterfullerene, *Nature*, **318**, 162--163, 1985.
4. Royal society of chemistry, *Nanoscience and nanotechnologies: opportunities and uncertainties*, Latimer Trend Ltd, London, 2004.
5. Sparks, S. *Nanotechnology: Business Applications and Commercialization*, Taylor and Francis group, Boca Raton, 2012.
6. Rogers, B., Adams, J. & Pennathu, S. *Nanotechnology: The Whole Story*, Taylor and Francis, Boca Raton, 2013.
7. Tiwari, J. et al. Zero-dimensional, one-dimensional, two-dimensional and three-dimensional nanostructured materials for advanced electrochemical energy devices, *Prog. Mat. Sci.* **57** (4), 724--803, 2012.
8. Schmid, G. *Nanoparticles: From Theory to Application*, Wiley, Weinheim, 2005.
9. Thanh, N. *Magnetic Nanoparticles: From Fabrication to Clinical Applications*, Taylor and Francis, Boca Raton, 2013.
10. Stevens, S.Y. & Krajcik J.S. *The big Ideas of Nanoscale Science and Engineering*, NSTA, USA, 2009.
11. Shum, K. Density of states in semiconductor nanostructures, *Appl. Phys.* **69** (9), 6484--6487, 1991.
12. Binns, C. *Introduction to Nanoscience and Nanotechnology*, John Wiley & Sons, New Jersey, 2010.

13. Adachi, S. *Properties of Group-IV, III – V and II – VI Semiconductors*, John Wiley and Sons, England, 2005.
14. Wiederrecht, G. *Handbook of Nanoscale Optics and Electronics*, Elsevier, Amsterdam, Netherlands, 2010.
15. Srivani, A. Investigation of Physical Properties in IIVI Ternary Semiconductors of Sulphides, Selenides And Tellurides, *Research Inventy: International Journal Of Engineering And Science* 2 (11), 26--35, 2013.
16. Erwin, S. Doping semiconductor nanocrystals, *Nature* 436, 91--94, 2005.
17. Norris, D. et al. Doped Nanocrystals, *Science* 319 (5871), 1776--1779, 2008.
18. Bryan J. & Gamelin, R. Doped Semiconductor Nanocrystals: Synthesis, Characterization, Physical Properties, and Applications, *Prog. Inorg. Chem.* 54, 47--126, 2005.
19. Schmidt, G. Concepts for spin injection into semiconductors—a review, *J. Phys. D: Appl. Phys.* 38 (7), 107--122, 2005.
20. Chen, D. & Wang, Y. Impurity doping: a novel strategy for controllable synthesis of functional lanthanide nanomaterials, *Nanoscale* 5 (11), 4621--4637, 2013
21. Lee, Y. & Ramdas, A. Origin of the Mn^{2+} optical transition in Mn-based II-VI diluted magnetic semiconductors, *Phys. Rev. B* 33 (10), 7383--7385, 1986.
22. Timm, C. Disorder effects in diluted magnetic semiconductors, *J. Phys.: Condens. Matter.* 15 (50), 1865--1896, 2003.
23. Smith, A. & Nie, S. Semiconductor Nanocrystals: Structure, Properties, and Band Gap Engineering, *Acc. Chem. Res.* 43 (2), 190--200, 2010.
24. Alivisatos, A. Semiconductor Clusters, nanocrystals and Quantum dots, *Science* 271 (5251), 933--937, 1996.
25. http://en.wikipedia.org/wiki/File:Wurtzite_polyhedra.png
26. Ung, T.D.T. et al. CdTe and CdSe quantum dots: synthesis, characterizations and applications in agriculture, *Adv. Nat. Sci.: Nanosci. Nanotechnol.* 3 (4), 1-11, 2012.
27. Li, Y. et al. White-light-emitting diodes using semiconductor nanocrystals, *Mikrochim. Acta.* 159 (3-4), 207--215, 2007.
28. Kim, J. et al. Color-converting bilayered composite plate of quantum-dot-polymer for high-color rendering white light-emitting diode, *Opt. Lett.* 38 (15), 2885--2888, 2013.

29. Klimov, V. *Semiconductor and Metal Nanocrystals: Synthesis and Electronic and Optical properties*, CRC Press, New York, 2003.
30. Jin, S. et al. Application of Quantum Dots in Biological Imaging, *J. Nanomater.* **2011**, 1--13, 2011
31. Resch-Genger, U. et al. Quantum dots versus organic dyes as fluorescent labels, *Nat. Methods* **5**, 763--775, 2008
32. Dickerson, B. *Organometallic Synthesis Kinetics of CdSe Quantum Dots*; Ph.D. dissertation, Virginia Polytechnic Institute and State University, Blacksburg, VA, ,2005
33. Chen, L., Chou H.L., Chenc C.H., Tseng, C.H. Surface Modification of CdSe and CdS Quantum Dots-Experimental and Density Function Theory Investigation, *Advances in Nanofibres*, Maguire, R. ,eds., InTech, DOI: 10.5772/48675, 2013, 149--168.
34. Zhu, H. et al. Synthesis and Optical Properties of Thiol Functionalized CdSe/ZnS (Core/Shell) Quantum Dots by Ligand Exchange, *J. Nanomater.* **2014**, 1--14, 2014.
35. Rogach, A. et al. Synthesis and Characterization of a Size Series of Extremely Small Thiol-Stabilized CdSe Nanocrystals, *J. Phys. Chem. B* **103** (16), 3065--3069, 1999.
36. Zhang, Y. & Clapp, A. Overview of Stabilizing Ligands for Biocompatible Quantum Dot Nanocrystals, *Sensors* **11** (12), 11036--11055, 2011.
37. Efros, A. et al. Paramagnetic Ion-Doped Nanocrystal as a Voltage-Controlled Spin Filter, *Phys. Rev. Lett.* **87** (20), 206601--206604, 2001.
38. Dalpian, G. & Chelikowsky, J. Self-Purification in Semiconductor Nanocrystals, *Phys. Rev. Lett.* **96** (22), 226802--226806, 2006.
39. Beaulac, R. et al. Mn²⁺-Doped CdSe Quantum Dots: New Inorganic Materials for Spin-Electronics and Spin-Photonics, *Adv. Funct. Mater.* **18** (24), 3873--3891, 2008.
40. Lee, Y. & Ramdas, A. Energy gap, excitonic, and "internal" Mn²⁺ optical transition in Mn-based II-VI diluted magnetic semiconductors, *Phys. Rev. B Condens Matter.* **38** (15), 10600--10611, 1988.
41. Jamiesona, T. et al. Biological applications of quantum dots, *Biomaterials* **28** (31), 4717--4732, 2007.

42. Dou, Y. et al. N-type doping in CdO ceramics: a study by EELS and photoemission spectroscopy, *Surf. Sci.* **398** (1-2), 241--258, 1998.
43. Jaffe, J. et al. Electronic structure of the rocksalt-structure semiconductors ZnO and CdO, *Phys. Rev. B* **43** (17), 14030--14034, 1991.
44. http://en.wikipedia.org/wiki/Cadmium_oxide
45. Manickathai, K. et al. Synthesis and characterization of CdS and CdO nanoparticles, *Indian J. Pure Appl. Phys.* **46**, 561--564, 2008.
46. King, P.D.C. & Veal, T.D. Conductivity in transparent oxide semiconductors, *J. Phys.: Condens. Matter*, **23** (33), 334214--334231, 2011.
47. Haul, R. & Just, D. Disorder and Oxygen Transport in Cadmium Oxide, *J. Appl. Phys.* **33** (1), 487--493, 1962.
48. Liu, H. et al. Transparent conducting oxides for electrode applications in light emitting and absorbing devices, *Superlattices Microstruct.* **48** (5), 458--484, 2010.
49. Lanje A. et al. Luminescence and electrical resistivity properties of Cadmium Oxide Nanoparticles, *Indian J. Pure Appl. Phys.* **49** (4), 234-238, 2011.
50. Kusigerski, V. et al. Synthesis and some physical properties of the diluted magnetic semiconductor $Cd_{1-x}Mn_xO$, *J. Phys.: Condens. Matter*, **8** (49), 10581--10584, 1996.
51. Z. Nabi, Z. et al. Ferromagnetism in CdOX (X = Mn and N) with and without intrinsic point defects: A density functional theory, *Results in Physics* **3**, 205--208, 2013.
52. Zheng, B. et al. Optical and electrical properties of Sn doped CdO thin films obtained by pulse laser deposition, *Vacuum* **85** (9), 861--865, 2011.
53. Dagdelen, F. et al. Preparation of nanostructured Bi-doped CdO thin films by sol – gel spin coating method, *Mater. Lett.* **80**, 127--130, 2012.
54. Benhaliliba, M. et al. Luminescence and physical properties of copper-doped CdO derived nanostructures, *J. Lumin.* **132** (10), 2653--2658, 2012.
55. Kavasoglu, N. et al. Observation of negative photoconductivity in $(ZnO)_x(CdO)_{1-x}$, films, *J. Phys. Chem. Solids* **70** (3-4), 521--526, 2009.
56. Gupta, R. et al. Effect of oxygen partial pressure on structural, optical and electrical properties of titanium-doped CdO thin films, *Appl. Surf. Sci.* **255** (5), 2414--2418, 2008.

57. Ruvalcaba-Cornejo, C. et al. Photoluminescence properties of the ZnO– CdO– TeO₂ system doped with the Tb³⁺ and Yb³⁺ ions, *J. Lumin.* **128** (2), 213--216, 2008.
58. Neenu, V. et al. Solvothermal synthesis of nanorods of ZnO, N-doped ZnO and CdO, *Mater. Res. Bull.* **42** (12), 2117--2124, 2007.
59. Dakhel, A. A. Electrical and optical properties of iron-doped CdO, *Thin Solid Films*, **518** (6), 1712--1715, 2010.
60. Dakhel, A. A. Effect of thermal annealing in different gas atmospheres on the structural, optical, and electrical properties of Li-doped CdO nanocrystalline films, *Solid State Sci.* **13** (5), 1000--1005, 2011.
61. Dakhel, A. A. Influence of annealing in nitrogen on the structural, electrical, and optical properties of CdO films doped with samarium, *Mater. Chem. Phys.* **117** (1), 284--287, 2009.
62. Dakhel, A. A. Effect of cerium doping on the structural and optoelectrical properties of CdO nanocrystallite thin films, *Mater Chem Phys.* **130** (1-2), 398--402, 2011.
63. Dakhel, A. A. Bandgap narrowing in CdO doped with europium, *Opt. Mater.* **31** (4), 691--695, 2009.
64. Salih, K. et al. In doped CdO films: electrical, optical, structural and surface properties, *Int. J. Hydrogen Energ.* **34** (12), 5260--5266, 2009.
65. Metin, K. et al. Electrical and optical properties of fluorine-doped CdO films deposited by ultrasonic spray pyrolysis, *Solar Energ. Mat. Sol. C.* **91** (10), 882--887, 2000.
66. Deokate, R. et al. Structural, optical and electrical properties of chemically sprayed nano sized gallium doped CdO thin films, *J. Alloys Compd.* **496** (1-2), 357--368, 2010.
67. Gupta, R. et al. Low temperature processed highly conducting, transparent, and wide bandgap Gd doped CdO thin films for transparent electronics, *J. Alloys Compd.* **509** (10), 4146--4149, 2011.
68. Gupta, R. et al. Band gap variation in size controlled nanostructured Li– Ni co-doped CdO thin films, *J. Alloys Compd.* **515**, 96--100, 2012.
69. Maity, R. & Chattopadhyay, K., Synthesis and characterization of aluminum doped CdO thin films by sol – gel process, *Sol. Energ. Mat. Sol. C.* **90** (5), 597--606, 2006.

Chapter I

70. Rajkumar, N. et al. On the possibility of ferromagnetism in CdO: Mn at room temperature, *J. Exp. Nanosci.* **6** (4), 389--398, 2011.
71. Ahmad, T. et al. Structural characterization, optical and magnetic properties of Ni-doped CdO dilute magnetic semiconductor nanoparticles, *J. Mater. Res.* **28** (9), 1245--1253, 2013.
72. Werner D. *The Biology of Diatoms*, University of California Press, Berkeley, 1977.
73. Wehr, J. D. & Sheath, R. G. (ed.) *Freshwater Algae of North America, Ecology and Classification, A volume in Aquatic Ecology*, Academic press, USA, 2002.
74. <http://craticula.ncl.ac.uk/EADiatomKey/html/introduction.html>
75. Round, F. E., Crawford, R.M & Mann, D.G. *The Diatoms: Biology and Morphology of the Genera*, Cambridge University Press, Cambridge, 1990.
76. Parker, A. & Townley, H. Biomimetics of photonic nanostructures. *Nat. Nanotechnol.* **2** (6), 347--353, 2007.
77. Townley, H. Modification of the physical and optical properties of the frustule of the diatom *Coscinodiscus wailesii* by nickel sulfate, *Nanotechnology* **18** (29), 295101--295106, 2007.
78. Fuhrmann, T. et al. Diatoms as living photonic crystals, *Applied Physics B: Lasers and Optics* **78** (3-4), 257--260, 2004.
79. Hamm, C. E. et al. Architecture and material properties of diatom shells provide effective mechanical protection, *Nature* **421**, 841-843, 2003.
80. Unocic, R.R. et al. Anatase assemblies from algae: coupling biological self-assembly of 3-D nanoparticle structures with synthetic reaction chemistry, *Chem. Commun.* (7), 796--797, 2004.
81. Weatherspoon, M. et al. Sol gel synthesis on self-replicating single-cell scaffolds: applying complex chemistries to nature's 3-D nanostructured templates, *Chem. Commun.* (5), 651--653, 2005.
82. Stefano, L.D. et al. Lensless light focusing with the centric marine diatom *Coscinodiscus wailesii*, *Opt. Express* **15** (26), 18082--18088, 2007.
83. Jaccard, T. et al. Incorporation of zinc into the frustule of the freshwater diatom *Stephanodiscus hantzschii*, *Chem. Geol.* **265** (3-4), 381--386, 2009.

Chapter I

84. Jeffreyes, C. et al. The potential of diatom nanobiotechnology for applications in solar cells, batteries, and electroluminescent devices, *Energy Environ. Sci.* **4** (10), 3930--3941, 2011.
85. Gale, D et al. Photoluminescence detection of biomolecules by antibody-functionalized diatom biosilica, *Adv. Funct. Mater.* **19** (6), 926--933, 2009.
86. Zhang, Y. et al. Development of a micro-swimming robot using optimized giant magnetostrictive thin films, *Appl. Bionics Biomech.* **3** (3), 161--170, 2006.
87. Jeffreyes, C. et al. Electroluminescence and photoluminescence from nanostructured diatom frustules containing metabolically inserted Germanium, *Adv. Mater.* **20** (13), 2633--2637, 2008.
88. Losic, D et al. Rapid fabrication of micro-and nanoscale patterns by replica molding from diatom biosilica, *Adv. Funct. Mater.* **17** (14), 2439--2446, 2007.
89. Losic, D. et al. Pore architecture of diatom frustules: potential nanostructured membranes for molecular and particle separations, *J. Nanosci. Nanotechnol.* **6** (4), 982--989, 2006.
90. Goswami, B. et al. Luminescence properties of a nanoporous freshwater diatom, *Luminescence*, **27** (1), 16--19, 2012.
91. Gordon, R et al. The Glass Menagerie: diatoms for novel applications in nanotechnology, *Trends Biotechnol.* **27** (2), 116--128, 2008.
92. Jarimavičiūtė-Žvalionienė, R. et al. Photoluminescence Properties of Porous Silicon with CdSe/ZnS Quantum Dots, *Mater. Sci.* **17** (3), 232--235, 2011.

Chapter II: Material Synthesis and Characterization Methods

This chapter deals with the synthesis and characterization methods adopted to prepare pristine and manganese doped nanoparticles of cadmium selenide (CdSe) and cadmium oxide (CdO). Chemical method was chosen to prepare the nanoparticles. Transmission electron microscopy (TEM) was used to take images of the samples. Energy dispersive X-ray spectroscopy was used for elemental analysis. Morphological study was done by X-ray diffraction (XRD). Oxidation states of elements were tested by electron paramagnetic resonance (EPR) spectroscopy and X-ray photoelectron spectroscopy (XPS). Fourier transform infrared (FTIR) spectroscopy was also done to observe the bonds formed.

2.1 Synthesis of pristine and manganese doped CdSe nanoparticles

2.1.1 Preparation of pristine CdSe nanoparticles by one pot synthesis method using water as solvent

CdSe nanoparticles were synthesized using a novel one pot synthesis method [1]. In all other methods a neutral environment is required, but in this case, as SeO_2 is used, neutral environment is not required. The precursor consisted of 2 mmol $\text{CdCl}_2 \cdot 5\text{H}_2\text{O}$ and 1 mmol SeO_2 . First 2 mmol $\text{CdCl}_2 \cdot \text{H}_2\text{O}$ was added in double distilled water. After stirring the solution for a few minutes, 0.5 ml TGA was added and pH was adjusted to 11 by adding 0.1 mol L^{-1} of NaOH. After several minutes 1 mmol SeO_2 and 0.1 g NaBH_4 was added. SeO_2 was reduced using NaBH_4 . Thioglycolic acid ($\text{C}_2\text{H}_4\text{O}_2\text{S}$, TGA) was used as capping agent. TGA contains a thiol and a carboxylic acid. It forms complex with metal ions. Synthesis method is slightly modified by incorporating size selective precipitation using Acetone to obtain powder samples with uniform size distribution. pH of the solution was kept at 11. The solution was refluxed at 100°C for 3 hrs to control the size of the CdSe nanoparticles. As the nuclei grow, Van der Waals interactions can cause rapid coalescence of the nuclei and thus forming larger nanoparticles. Ligands such as TGA which are chemically bonded to both the solvent and nanoparticle resist Van der Waals forces. To determine the influence of pH on the properties, nanoparticles were synthesized with different pH levels.

2.1.2 Preparation of manganese doped CdSe nanoparticles

For doping in 1 %, 2.5 % and 5 % molar ratios, (2-X) mmol of $\text{CdCl}_2 \cdot \text{H}_2\text{O}$ was taken in water and the solution was stirred for a few minutes. Then 0.5 ml TGA was added and pH was adjusted to 11 by adding 0.1 molL^{-1} of NaOH. After stirring for several minutes 1 mmol SeO_2 and 0.1 g NaBH_4 was added. SeO_2 was reduced using NaBH_4 . Thioglycolic acid ($\text{C}_2\text{H}_4\text{O}_2\text{S}$, TGA) was used as capping agent. X mmol of manganese acetate after dissolving in 10 ml of water was then added into the precursor solution drop wise. Powder samples were obtained by using size selective precipitation. The solution was refluxed at 100°C for 3 hrs to control the size of the CdSe nanoparticles.

2.2 Synthesis of pristine and manganese doped CdO nanoparticles

2.2.1 Preparation of pristine CdO nanoparticles:

CdO nanoparticles were prepared by a simple and cost effective sol-gel method [2]. cadmium acetate 6.6 gm (0.5 M) was dissolved in 100 ml of distilled water. Ammonia solution was added to the above solution with constant stirring until pH became 8. White precipitate was obtained which was allowed to settle for 12 hours and then centrifuged and washed 3 times by distilled water. Washed precipitate was dried at 80°C and ground. Resulting white powder was calcined at 400°C , 600°C and 800°C . To see the differences in the properties of the nanoparticles when annealed in air and vacuum, two parts of the as prepared samples were taken and again dried them in both air and vacuum conditions at 150°C in 760 mm Hg vacuum pressure.

2.2.2 Preparation of manganese doped CdO nanoparticles

Manganese doped CdO nanoparticle samples were prepared in 1 %, 2.5 % and 5 % molar ratios. First, cadmium acetate 6.6 gm (0.5 M) was dissolved in 100ml of distilled water. Then aqueous Mn acetate was added to the solution drop wise. Ammonia solution was then added to the above solution with constant stirring until pH became 8. White precipitate was obtained which was allowed to settle for 12 hours and then centrifuged

Chapter II

and washed 3 times by distilled water. Washed precipitate was dried at 80 °C and ground. Resulting white powder was calcined at 400 °C.

2.3 Transmission electron microscopy (TEM), Selected area electron diffraction (SAED/SAD) and Energy dispersive X-Ray (EDX) studies

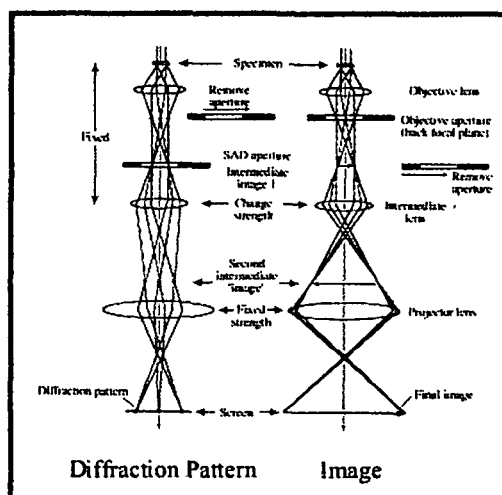


Figure 2.1: Ray diagram of TEM (Ref 4)

To get the image, particle size and/or grain size of the synthesized nanoparticles, Transmission electron microscopy was used. TEM images the transmission of a focused beam of electrons through a sample, forming an image in a way analogous to a light microscope [3]. The image formation is shown by the ray diagram in Figure 2.1 [4]. However, because electrons are used rather than light to illuminate the sample, TEM imaging has significantly higher resolution (by a factor of about 1000) than light-based imaging techniques. At smaller magnifications, TEM image contrast is due to absorption of electrons in the material, due to thickness and composition of the material. At higher magnifications complex wave interactions modulate the intensity of the image. TEM consist of an emission source (electron gun) which may be tungsten filament or a lanthanum hexaboride (LaB_6) source. By connecting this gun to a higher voltage source, the gun will begin to emit electrons. Coupling of magnetic field and electrostatic field in opposite directions allows for the shift in the beam path. Magnetic field allows for the

Chapter II

formation of magnetic lens of variable focusing power and electrostatic field can cause the electrons to be deflected through a constant angle. The lenses of the TEM allow for the beam convergence as a variable parameter, giving the ability to modify the amount of current passing through the lenses. Typically, a TEM consists of three stages of lenses; the condenser lens forming the primary beam, the objective lens focusing the electron beam that comes through the sample and the projector lens expanding the beam onto the phosphor screen or other imaging device. Here, TEM images were taken by High resolution transmission electron microscope (HR-TEM/JEM-2100, 200 KV, JEOL).

The selected area diaphragm is used to select only one part of the imaged sample. This mode of TEM, called selected area electron diffraction (SAED) mode, permits to obtain the symmetry of the lattice and calculate its interplanar spacing.

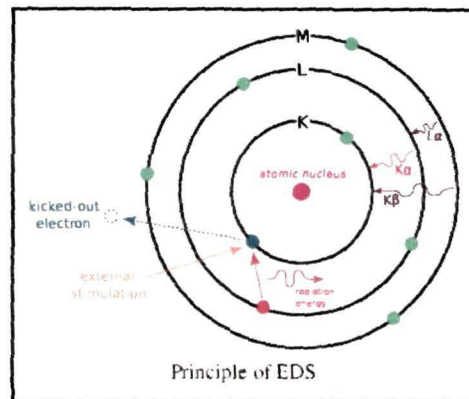


Figure 2.2: Principle of EDX (Ref 6)

Energy-dispersive X-ray spectroscopy (EDX) is an analytical technique to investigate the elemental characterization of a sample [5]. It relies on the investigation of an interaction of some source of X-ray excitation and a sample. The fundamental principle of EDX is that each element has a unique atomic structure allowing unique set of peaks on its X-ray spectrum. The emission of characteristic X-rays from a specimen is triggered when a high-energy beam of charged particles such as electrons or protons (PIXE), or a beam of X-rays, is focused onto the sample. The incident beam may excite an electron in an inner

shell, ejecting it from the shell while creating an electron hole where the electron was previously. An electron from an outer, higher-energy shell then fills the hole. The difference in energy between the higher-energy shell and the lower energy shell may be released in the form of an X-ray which is depicted in Figure 2.2 [6]. The number and energy of the X-rays emitted from a specimen can be measured by an energy-dispersive spectrometer. As the energy of an X-ray is characteristic of the difference in energy between the two shells, and of the atomic structure of the element from which they were emitted, this allows the elemental composition of the sample to be measured.

2.3.1 TEM, SAED and EDX study of pristine and manganese doped CdSe nanoparticles

TEM images of pristine CdSe nanoparticles are shown in Figure 2.3 (A). The statistical analysis (Figure 2.3 (B)) of the images depicts that the average particle size is 5 nm. EDX and SAED pattern of the pristine nanoparticles are also shown in Figure 2.4 (A and B). EDX (JEOL, JSM-6390LV, INCAx-sight) detector confirms that the sample contains cadmium and selenium without any oxygen and weight percentage of cadmium and selenium are 63.71 % and 31.61 % respectively. SAED confirms the polycrystalline nature of the sample and crystallite planes are also marked in the same. The interplanar spacing for one 5 nm particle is calculated to be 0.35 nm.

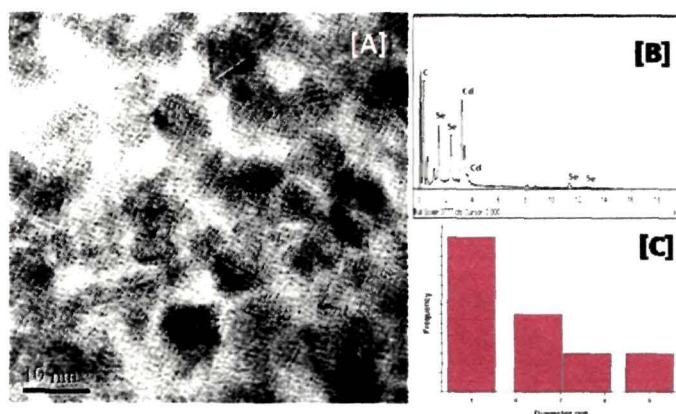


Figure 2.3: (A) HR-TEM, (B) EDX and (C) particle size calculation of CdSe nanoparticles

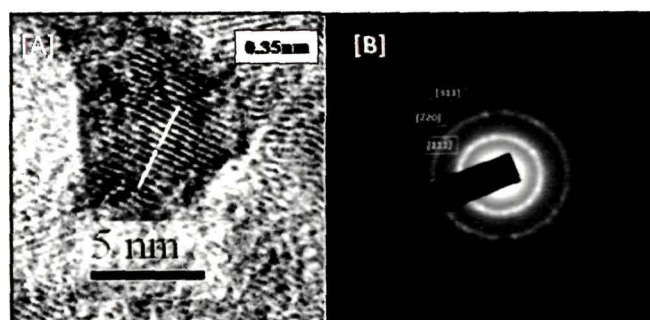


Figure 2.4: (A) Interplanar spacing and (B) SAED of CdSe nanoparticles

Figure 2.5 (A) shows HR-TEM images of the 1 % manganese doped samples. Statistical analysis shows that the average particle size is 5 nm and there is a small size variation of 5-13 nm in the sample. SAED pattern of the crystalline areas of Figure 2.5 (A) shows bright circular rings indicating high crystallinity in the sample. EDX shown in Figure 2.5 (C) confirms presence of manganese in the sample.

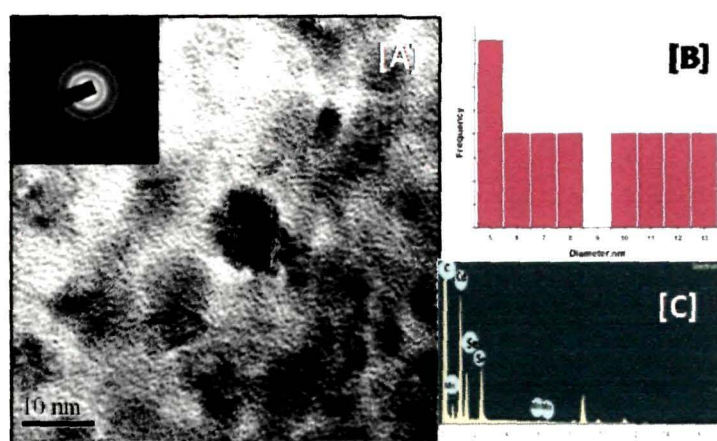


Figure 2.5: (A) HR-TEM, (B) particle size calculation, (C) EDX of Mn doped CdSe nanoparticles

2.3.2 TEM, SAED and EDX study of pristine and manganese doped CdO nanoparticles

Size of a single CdO nanoparticle synthesized at 400 °C is around 25 nm as depicted in high-resolution image shown in Figure 2.6 (a). Crystal planes can be seen in HR-TEM. Selected area electron diffraction (SAED, Figure 2.6 (c)), was also taken to confirm crystalline nature. Presence of cadmium and oxygen are confirmed by EDX taken by

Chapter II

JEOL, JSM-6390LV, INCAx-sight EDX detector as shown in Figure 2.6 (b). Weight percentage of Oxygen present is 63.37 and cadmium is 31.63.

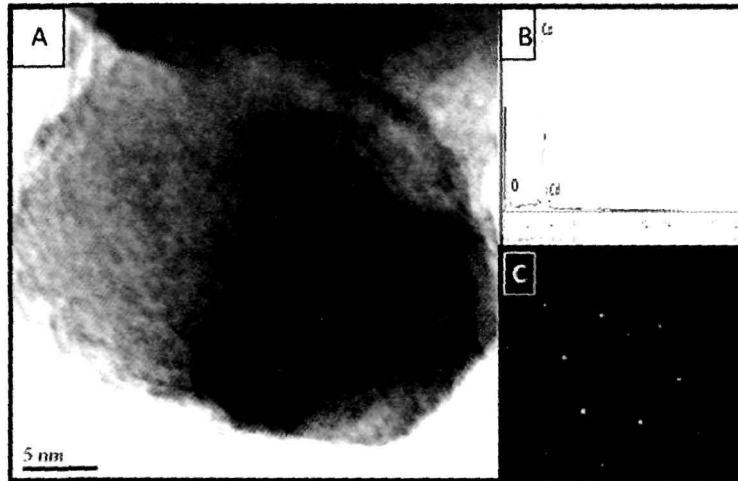


Figure 2.6: (A) HR-TEM image, (B) EDX and (C) SAED of CdO nanoparticles

The unproportional ratio between cadmium and oxygen found from EDX may be due to the defects present in the system. Also since EDX is a surface sensitive tool and can determine dopant concentration upto a few layers from surface, so obtained weight ratio indicates presence of cadmium and oxygen only a few nanometer depth from the surface of CdO.

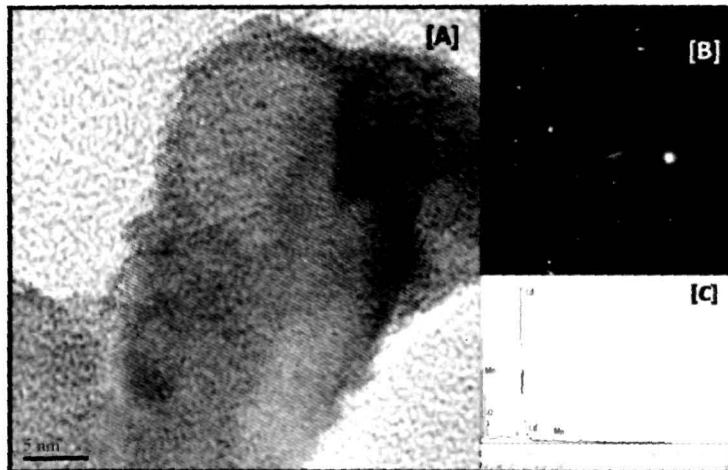


Figure 2.7: (A) HR-TEM, (B) SAED and (C) EDX of Mn doped CdO nanoparticles

HR-TEM images of manganese doped CdO nanoparticles are shown in Figure 2.7 where particle agglomeration was seen. This is because surfactants are not used for preparation of the CdO nanoparticles. EDX (Figure 2.7 (C)) confirms the presence of manganese.

2.4 X-Ray diffraction studies

XRD is very useful to study morphological properties of the nanoparticles. In an XRD measurement, a crystal is mounted on a goniometer and is gradually rotated while being bombarded with X-rays. This produces a diffraction pattern of regularly spaced spots known as reflections. The two dimensional images taken at different rotations are converted into a three-dimensional model of the density of electrons within the crystal using the mathematical method of Fourier transforms, combined with chemical data known for the sample. Poor resolution or even errors may result if the crystals are too small, or not uniform enough in their internal structure [7]. Earlier Scherrer formula was used to determine crystalline size from the XRD plot which is given by, $D=0.9\lambda/\beta\cos\theta$, where β =FWHM, $\lambda=1.54 \text{ \AA}$, 2θ =peak position, D = Crystallite size [8]. From Scherrer formula it is always difficult to separate size and strain broadening present in XRD peaks. Williamson-Hall (W-H) method is used to separate these two effects by equation, $\beta\cos\theta=(k\lambda/D) + \eta\sin\theta$, where η is the strain, the value of D represents the size of the crystallites, constant k typically close to 1 [9]. From $\beta\cos\theta$ versus $\sin\theta$ graph as shown in Figure 2.8 (B), a straight line with slope η was obtained. Slope η gives strain generated in the nanoparticles. Crystallite size (D) can also be determined from this method.

Morphological properties were studied by XRD. XRD pattern was collected by using Bruker D8 focus AXS X-ray diffractometer with $\text{CuK}\alpha$ radiation ($\lambda=1.5405 \text{ \AA}$). The XRD pattern and W-H plot for CdSe nanoparticles are shown in the Figure 2.8. Grain size for the CdSe nanoparticles having zinc blende crystalline was found to be 5 nm. D-spacing for the same was found to be 0.35 nm which was also found from HR-TEM of CdSe nanoparticles (Figure 2.5 (A)).

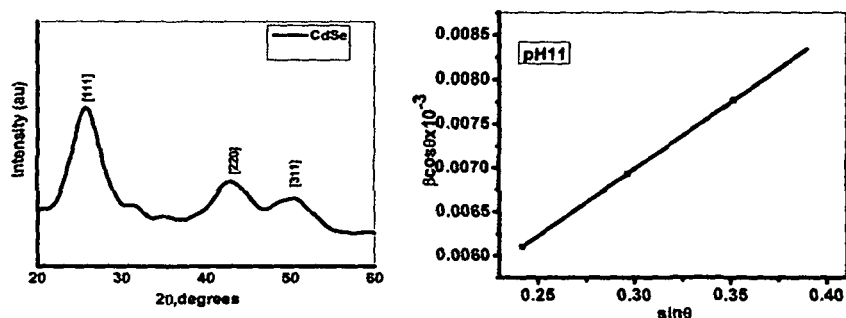


Figure 2.8: XRD and W-H plot of CdSe nanoparticles

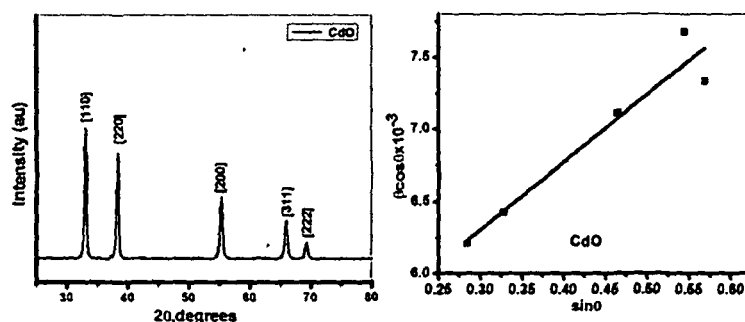


Figure 2.9: XRD and W-H plot for CdO nanoparticles

Figure 2.9 is the XRD and W-H plot for Montepionite CdO with a cubic structure which was matched with the XRD data of our samples (JCPDS#050640). Often crystallite size matches with grain size but it may be different from particle size in the nano range. From HR-TEM, particle size of CdO nanoparticle is found to be 25 nm but crystallite size from W-H plot is found to be 24 nm.

2.5 Fourier Transform Infrared (FTIR) Spectroscopy

Infrared spectroscopy is the spectroscopy that deals with the infrared region of the electromagnetic spectrum. It covers a range of techniques, mostly based on absorption

Chapter II

spectroscopy. IR spectroscopy can be used to identify and study chemicals and chemical bonds. Fourier transform infrared (FTIR) spectrometer uses IR spectroscopy technique to analyze samples. The term Fourier transform infrared spectroscopy originates from the fact that a Fourier transform is required to convert the raw data into the actual spectrum. The theory is based on the fact that molecules absorb specific frequencies that are characteristic of their structure. These absorptions are resonant frequencies i.e. the frequency of the absorbed radiation matches the transition energy of the bond or group that vibrates. In this technique, a beam containing many frequencies of light are allowed to fall on the sample at once, and measures how much of that beam is absorbed by the sample [10].

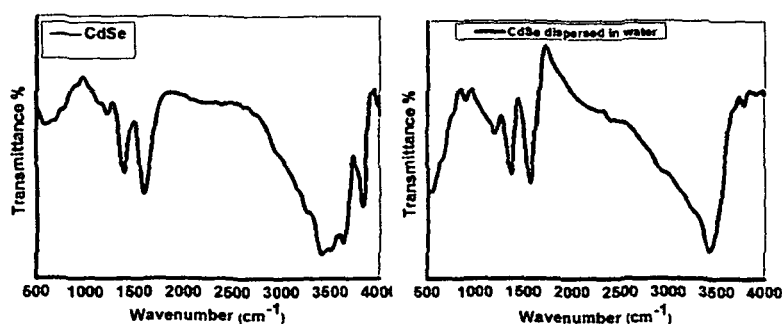


Figure 2.10: FTIR spectra of CdSe nanoparticles before and after dispersion in water

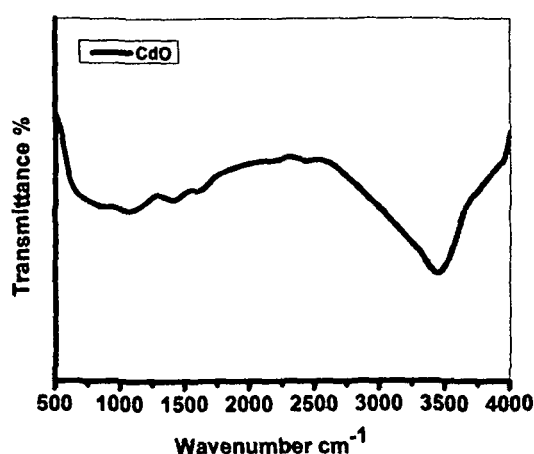


Figure 2.11: FTIR spectroscopy of CdO nanoparticles

Fourier transform infrared spectroscopy is performed by Nicolet Impact I-140. FTIR of the samples before and after dispersion in water are shown in the Figure 2.10. At 1388 cm^{-1} , CH_3 bending vibration can be seen. At 1591 cm^{-1} , there is a CO vibration peak. At 3426 cm^{-1} , an OH vibration peak was found. FTIR spectra confirm absence of -SH group in CdSe sample by the lack of vibration peak at around 2576 cm^{-1} . This is due to the formation of covalent bonds between thiols and Cd^{2+} ions on the surface of CdSe nanoparticles [11,12]. FTIR spectroscopy of CdO nanoparticles is shown in Figure 2.11 where OH vibrations at around 3439 cm^{-1} are seen.

2.6 X-ray photoelectron spectroscopy study

XPS is one of the most powerful techniques which can give accurate qualitative elemental analysis (except Hydrogen and Helium) and quantitative composition and at the same time chemical state (binding and oxidation). XPS can get information from the top 10 nm surface [13]. XPS is based on the photoelectric effect discovered by Hertz in 1887 in which interaction of an X-ray photon with sufficient energy with a solid eject an electron from the surface. Since the energy levels are quantized, the photoelectrons have a kinetic energy distribution consisting of discrete peaks associated to the electron levels of the photoionized atom. The emitted electrons have a kinetic energy given by: $E_K = h\nu - E_B - \phi$, where E_K is the kinetic energy of the photoelectrons; $h\nu$, the incident photon energy; E_B , the electron binding energy; and ϕ , the work function. E_B can be obtained by measuring E_K . The identification of the elements present on the surface is done directly by the binding energies of the core photoelectrons [14]. A typical XPS spectrum is a plot of the number of electrons detected (sometimes per unit time) versus the binding energy of the electrons detected.

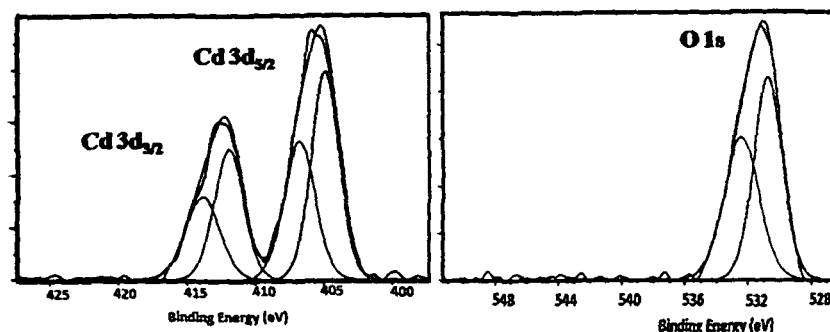


Figure 2.12: XPS of CdO nanoparticles

XPS of CdO nanoparticles are shown in the Figure 2.12. Cd 3d and O 1s binding energies are shown in the Figure. Cd 3d features consists of two main 3d_{5/2} and 3d_{3/2} spin-orbit components at 406 eV and 413 eV which agree well with the 6.74 eV spin-orbit energy splitting between Cd 3d_{5/2} and Cd 3d_{3/2} states [15,16]. Deconvolution of Cd 3d_{5/2} peak renders two peaks with binding energies of 405 eV and 407 eV which can be related to Cd(OH)₂ and CdO respectively. Similarly, Deconvolution of Cd 3d_{3/2} peak gives two peaks at 412 eV and 414 eV at an energy difference of around (\approx) 7 eV corresponding to their Cd 3d_{5/2} peaks. Moreover two peaks are found for O1s at 531 eV and 533 eV which are due to related CdO systems and are due to presence of hydroxyl species on the surface.

2.7 Electron paramagnetic resonance spectroscopy

EPR spectroscopy is used at the microscopic level to get information about the oxidation state, lattice defects, color centres, site occupancy and magnetic phases in the host semiconductor lattice. EPR can reveal the subtle changes occurring in the crystal environment surrounding the paramagnetic impurity such as Mn²⁺. In presence of an external magnetic field, unpaired electron spins absorb microwave radiation. EPR measures the transition frequency between different electron spin states. The energy difference between an electron spin state $m_s = \frac{1}{2}$ and $m_s = -\frac{1}{2}$ in a reasonably strong

Chapter II

magnetic field of 1 Tesla is $\Delta E = 1.86 \times 10^{-23}$ J. In the presence of an external magnetic field, the electron's magnetic moment aligns itself either parallel ($1/2$) or antiparallel ($-1/2$) to the field, each alignment having a specific energy due to the Zeeman effect, $E = m_s g_e \mu_B B_0$ where g_e is the electron's so-called g -factor, μ_B is the Bohr magneton. Therefore, the separation between the lower and the upper state is $\Delta E = g_e \mu_B B_0$ for unpaired free electrons. This equation implies that the splitting of the energy levels is directly proportional to the magnetic field's strength. An unpaired electron can move between the two energy levels by either absorbing or emitting a photon of energy $h\nu$ such that the resonance condition, $\Delta E = h\nu$, is obeyed. This leads to the fundamental equation of EPR spectroscopy, $h\nu = g_e \mu_B B_0$ [17]. When incident external magnetic field was varied, the gap between $+1/2$ and $-1/2$ widens and at one point it matches with the ΔE of the microwave. At this point the unpaired electrons can move between their two spin states. Since, there typically are more electrons in the lower state due to MB distributions, there is a net absorption that is monitored and converted into a spectrum [18].

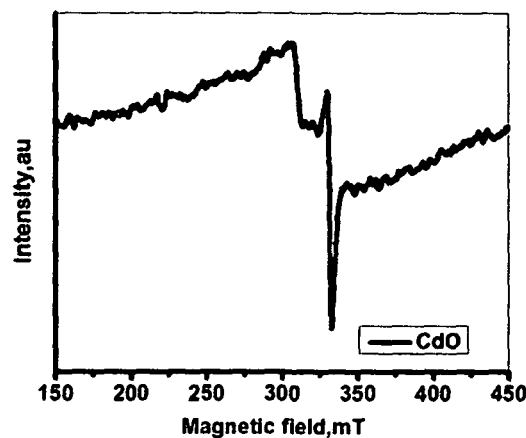


Figure 2.13: EPR spectroscopy of CdO nanoparticles

EPR spectroscopy [EPR, ESR-JEOL, Japan, model: ES - FA200 ESR Spectrometer with X and Q band, Standard Frequency (X band) - 8.75-9.65 GHz, Sensitivity - 7×10^9 spins/0.1mT, Resolution - 2.35(micro) T or better] is used at the microscopic level to get information about the oxidation state, lattice defects, color centres, site occupancy and magnetic phases in CdO nanoparticles as shown in Figure 2.13. Bulk CdO is a general non-stoichiometric n-type semiconductor. When it is in nano size range its

properties change from the bulk. Non-stoichiometric CdO nanoparticles show asymmetric EPR signal. Both bulk and nano CdO crystallizes in the NaCl-type structure. The distance between cadmium and oxygen (Cd-O) is 2.34 Å. The CdO contains Cd nuclei with natural abundance. Apart from the isotopes with even masses, there are the two odd isotopes ^{111}Cd (12.75%; $I=1/2$; $\mu=0.592\mu_N$) and ^{113}Cd (12.26 %; $I=1/2$; $\mu=0.619\mu_N$). It is assumed that the paramagnetic center is a Cd^+ ion ($2S_{1/2}$ ground state) on the site of a Cd^{2+} ion. The unpaired electron is localized not only at the central Cd^+ ion, but reaches far into the crystal [19]. Therefore, on the basis of other already reported results, signals with $g=2.046686$ and $g=2.202907$ were assigned to conduction band electrons, and to Cd^+ ions on the site of Cd^{2+} . Cd^+ ions arise from polaronic self-trapping of electrons introduced by oxygen deficiency at Cd sites to generate localized $5s^1$ states [20]. Already reported results show that Cd^+ states were not involved in the conduction band. Same kind of behavior has been previously elucidated for other systems i.e. SnO_2 , TiO_2 . In these systems self-trapped electronic states are observed close to the conduction band edge rather than in the middle of the band gap. At liquid Helium temperature, EPR spectrum gives rise to hyperfine and superhyperfine lines for the peak of localized electrons [21-23]. The presence of nuclear moments in cadmium isotopes can contribute local magnetic fields at the electron in addition to the main applied field. Since the possible orientations of a nuclear moment are $2I + 1$, where I is the nuclear spin quantum number, the absorption spectrum for the electron will consist of $2I + 1$ lines. So, ^{111}Cd and ^{113}Cd should give rise to hyperfine lines. But the other peak due to conduction electrons disappears at liquid Helium temperature. Single electrons can produce localized lattice distortions in ionic solids because of their electrostatic interaction with neighboring ions. As the electron moves through the lattice, this lattice distortion moves with the electron. This results in what is known as polaron. When the distortion is sufficiently strong, the electron may be trapped at a particular lattice site. EPR peaks observed in present experiments are due to localized Cd $5s^1$ states.

Chapter II

References:

1. Beaulac, R. et al. Spin-Polarizable Excitonic Luminescence in Colloidal Mn²⁺-Doped CdSe Quantum Dots, *Nano lett.* **8** (4), 1197--1201, 2008.
2. Lanje, A. S. et al. Luminescence and electrical resistivity properties of Cadmium Oxide nanoparticles, *Indian J Pure Ap Phy* **49**, 234--238, 2011.
3. Egerton, R. *Physical principles of electron microscopy*, 1st ed., Springer, New York, 2005.
4. <http://hrdg.matse.illinois.edu/images/pdf/TEMbasics.pdf>
5. Hanke, L. *Handbook of analytical methods for materials*, Materials Evaluation and Engineering, Inc. Plymouth, MN, 2001.
6. http://en.wikipedia.org/wiki/Energy-dispersive_X-ray_spectroscopy
7. Pecharsky, V. *Fundamentals of Powder Diffraction and Structural Characterization of Materials*, 2nd ed., Springer, 2009.
8. Nogi, K. *Nanoparticle Technology Handbook*, 2nd ed, Elsevier, UK, 2012.
9. Nelson, J.B. & Riley, D.P. An experimental investigation of extrapolation methods in the derivation of accurate unit-cell dimensions of crystals, *Proc. Phys. Soc.* **57** (3), 160--177, 1945.
10. Mote, V et al. Williamson-Hall analysis in estimation of lattice strain in nanometer-sized ZnO particles, *J. Theor. and Appl. Phys.* **6** (6),1--8, 2012.
11. Stuart, B.H. *Infrared Spectroscopy: Fundamentals and Applications*, John Wiley & Sons Ltd, England, 2004.
12. Zeng, J. et al. Fine tuning photoluminescence properties of CdSe nanoparticles by surface states modulation, *J Colloid Interface Sci.* **298** (2), 685--688, 2006.
13. Mohai, M. *Development and applications of quantitative photo electron spectroscopy*, Ph. D. thesis, Institute of Materials and Environmental Chemistry, Chemical Research Centre, Hungarian Academy of Sciences, 2006.
14. Nascente, P. Materials characterization by X-ray photoelectron spectroscopy, *J. Mol. Catal. A: Chem.* **228** (1-2), 145--150, 2005.

15. Khallaf, H. et al. Investigation of chemical bath deposition of CdO thin films using three different complexing agents, *Appl. Surf. Sci.* **257** (22), 9237--9242, 2011.
16. Gulino, A. & Tabbi, G. CdO thin films: a study of their electronic structure by electron spins resonance spectroscopy, *Appl. Surf. Sci.* **245** (1-4), 322--327, 2005.
17. Rajkumar, N. et al. On the possibility of ferromagnetism in CdO:Mn at room temperature, *J. Exp. Nanosci.* **6** (4), 389--398, 2011.
18. Weil, J. & Bolton, J. *Electron Paramagnetic Resonance: Elementary Theory and Practical Applications*, 2nd ed. John Willey & Sons, Inc, New Jersey, 2007.
19. Shinde, R., Date, S. X-band EPR studies of hyperfine and superhyperfine structure of Mn²⁺ ions in polycrystalline CdO, *Mater. Chem. Phys.* **24** (1-2), 71--81, 1989.
20. B. Santara, B. et al. Evidence of oxygen vacancy induced room temperature ferromagnetism in solvothermally synthesized undoped TiO₂ nanoribbons, *Nanoscale* **5** (12), 5476--5488, 2013.
21. Wolff, P et al. Polaron-polaron interactions in diluted magnetic semiconductors, *J. Appl. Phys.* **79** (12), 5196--5198, 1996.
22. Kaminski, A. & Sarma, S.D. Polaron percolation in diluted magnetic semiconductors, *Phys. Rev. Lett.* **88** (24), 247202--247206, 2002.

**Chapter III: Effect of pH and Dopant on Cadmium
Selenide Nanoparticles**

3.1 Effect of pH on structural and optical properties of CdSe nanoparticles

Optical properties of cadmium selenide (CdSe) nanoparticles prepared by a novel one pot synthesis method described in page section 2.2.1 of chapter II were investigated by varying pH of the precursor. Four different pH were taken for the solution. It is found that luminescence intensity of CdSe nanoparticles change with pH and it is highest for pH 11. Also it is found that for pH 11, band gap is maximum. High-resolution transmission electron microscope (HR-TEM) image of the CdSe nanoparticles is shown in Figure 2.3 and 2.4 of chapter II. These particles crystallize in zinc blende crystalline structure. Only first [111] peak was prominent. It has been observed that [111] peak is broadened. Comparison of the XRD pattern is shown in Figure 3.1.

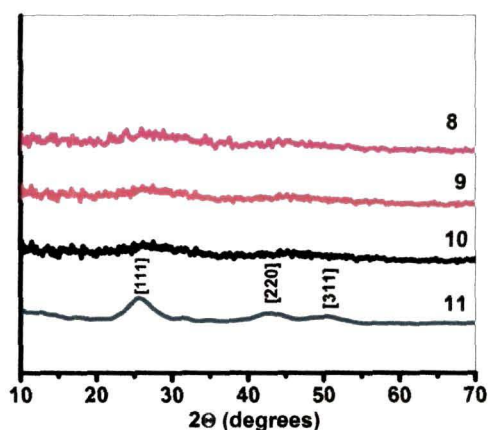


Figure 3.1: XRD of the synthesized nanoparticles

Crystallite size of the nanoparticles prepared in pH 11 is calculated by Williamson-Hall method as shown in Figure 3.2 which is found to be 4 nm. W-H plot could not be plotted for all other particles as XRD pattern is not clear. Later, it is explained that CdSe nanoparticles were in crystalline form when they are prepared in a certain pH. Otherwise, it may also possible that at pH 8, 9 and 10, these nanoparticles are so small that XRD pattern is not well defined for them.

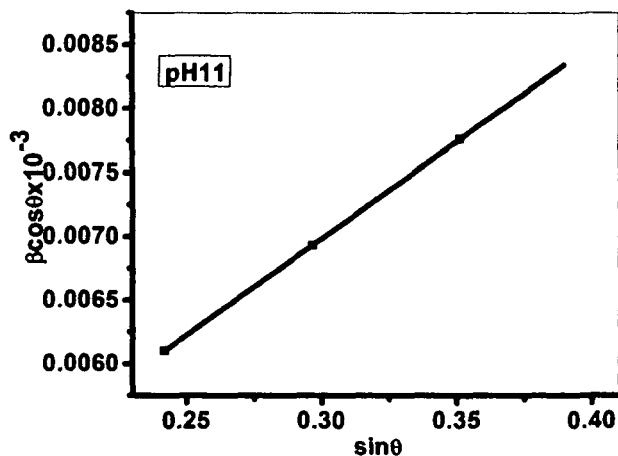


Figure 3.2: Williamson-Hall plot of CdSe nanoparticles

UV-Vis absorption spectra of the CdSe nanoparticles prepared in pH 8, 9, 10, 11 were taken as shown in Figure 3.3. From absorbance spectra band gap of the nanoparticles can be derived by using Tauc's plot [1-3]. For direct band gap semiconductors, band gap is determined from the plot of square of the product of absorption co-efficient and photon energy along y-axis and photon energy along x-axis. This plot is a curve which should have a section of straight line. If this straight line portion is extended to the x-axis, the x-intercept of this line gives the optical band gap.

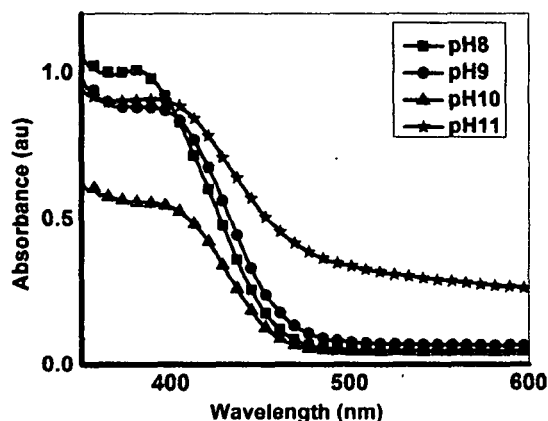


Figure 3.3: UV-Visible absorption spectra

Chapter III

Tauc's plots for calculating band gap of the nanoparticles are shown in the Figure 3.4 bellow. Band gaps are 1.71 eV, 1.73 eV, 1.76 eV and 1.77 eV for pH 8, 9, 10 and 11 respectively.

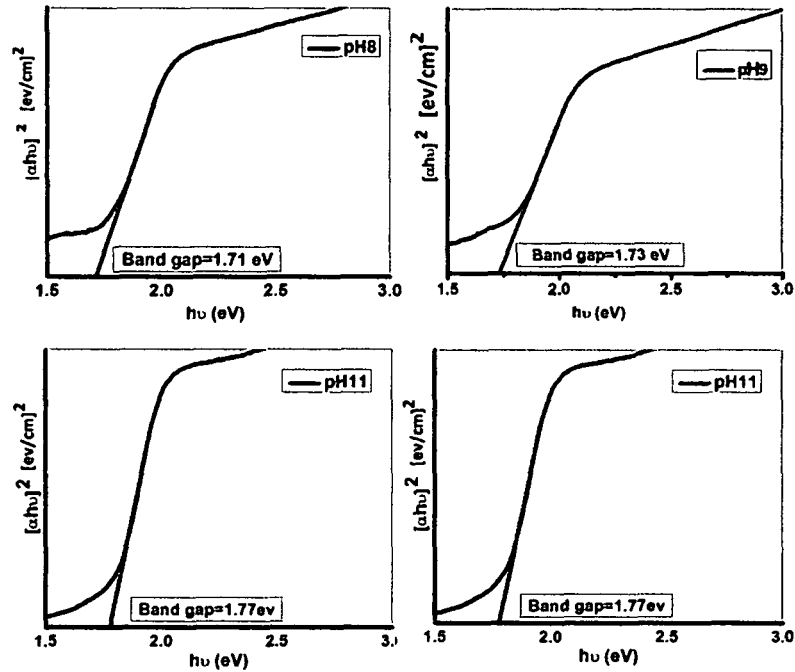


Figure 3.4: Tauc's plot of the CdSe samples at different pH

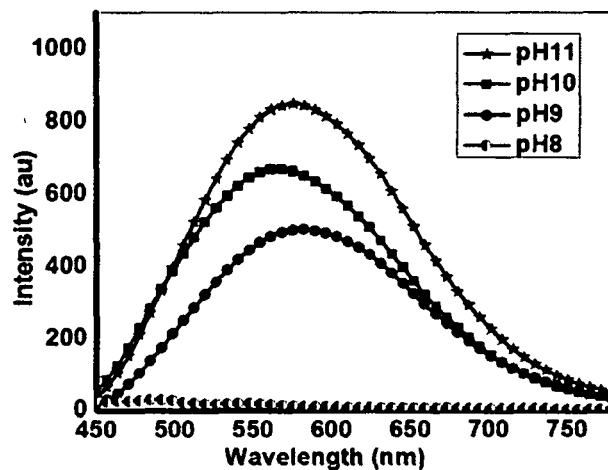


Figure 3.5: PL spectra of CdSe nanoparticles prepared in different pH

Chapter III

PL spectra of the nanoparticles are shown in the above Figure 3.5. When a system of molecules absorbs energy it goes to an excited state. One way of relaxation is to emit photons. Here this case, it was found that emission of the nanoparticles prepared in pH 11 is at around 550 nm. At pH 11, CdSe nanostructures showed maximum luminescence. For other pH luminescence intensity decreases. For pH 8, it is lowest. So, it may be possible that luminescence intensity highly depends upon pH. CdSe nanoparticles are coated with organic capping agent Thioglycolic acid (TGA). Thioglycolic acid (TGA) is an organic compound with the formula $\text{HSCH}_2\text{CO}_2\text{H}$. TGA is often called Mercaptoacetic acid (MAA). It contains both a thiol (mercaptan) and a carboxylic acid. It is a clear liquid with a strong unpleasant odor. Its IUPAC name is 2-Sulfanylacetic acid. In our case, some of the TGA molecules may depart from the CdSe nanoparticles into the solvent until a dynamic equilibrium is established between the adsorbing and desorbing of TGA from the NPs surfaces. At pH 11, a dynamic equilibrium is finally established and so the luminescence intensity is highest and also from XRD it is confirmed that at pH 11 CdSe nanoparticles took crystalline nature [5]. This argument is further confirmed from the Fourier transform infra-red spectra results shown in Figure 3.6.

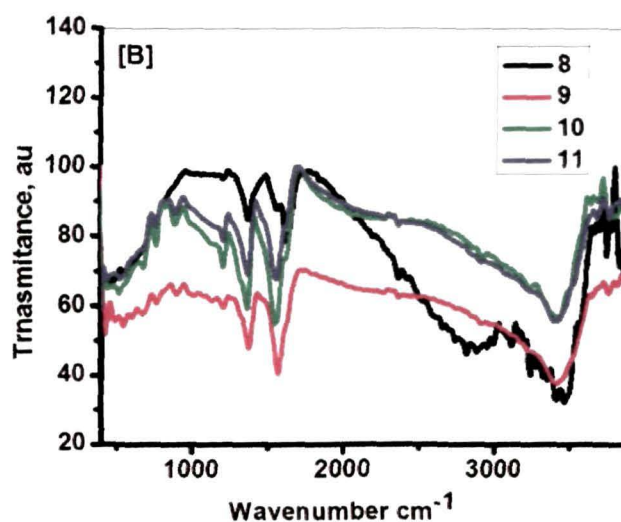


Figure 3.6: FTIR spectra of the CdSe nanoparticles prepared in pH 8, 9, 10 & 11

FTIR spectra confirm presence of -SH group in CdSe nanoparticles which were prepared in pH 8. For pH 9, 10 and 11, -SH vibrational peak which should be at around 2576 cm^{-1} , was absent [4]. This is due to the formation of covalent bonds between thiols and Cd^{2+} ions of the surface of CdSe nanoparticles.

Optical and structural properties of the nanoparticles were investigated by varying pH of the solution. Crystallite size of the nanoparticles prepared in pH 11 was found to be 4 nm. XRD pattern for all other pH were not clear. It may be possible that due to small size of the particles XRD for pH 8, 9, 10 were not clear. Band gap of the nanoparticles were calculated and it was found that band gap increase with increase in pH which may be due to increase in particle size of the nanoparticles with pH. In intermediate pH levels (pH=11), chemical interaction between thiolate group of TGA and the surface of Cd^{2+} is same as that between thiolate groups and H^+ ions in water [5]. Lowering pH enhances the number of H^+ concentration which promotes increase in the number of free thiols and uncoated nanoparticles and aggregated nanoparticles. And so photoluminescence intensity for lower pH (8, 9, 10) is low. At pH 11, a dynamic equilibrium is established and so the luminescence intensity is highest.

3.2 Effect of dopant on structural and optical properties of CdSe nanoparticles

Synthesis of manganese doped CdSe nanoparticles are described in section 2.2.2 of chapter II. High resolution transmission electron microscopy pictures are shown in Figure 2.5 of chapter II. Synthesized particles are precipitated as power and diffuse reflectance spectra were taken which is shown in Figure 3.7. From diffuse reflectance spectra band gap was calculated by using Kubelka-Munk function, $F(R)=(1-R)^2/2R$ and is shown in Figure 3.8. Where R is the reflectance in percentage, h is the Planck's constant, ν is the frequency of incident light. For a semiconductor sample $[F(R).h\nu]^2$ vs Energy (h ν) in electron volt plot gives Tauc's plot.

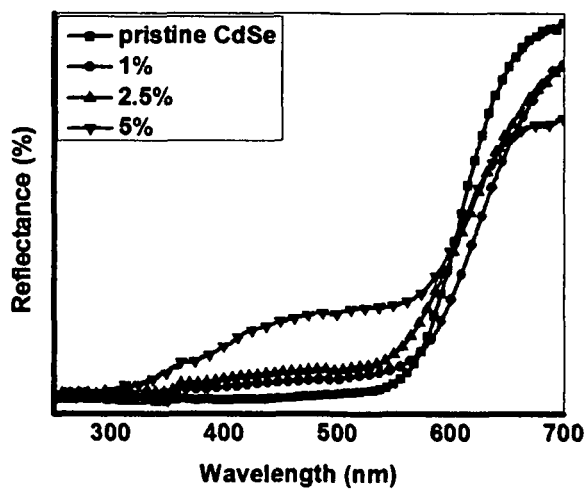


Figure 3.7: Diffuse reflectance spectra of pristine and doped CdSe nanoparticles

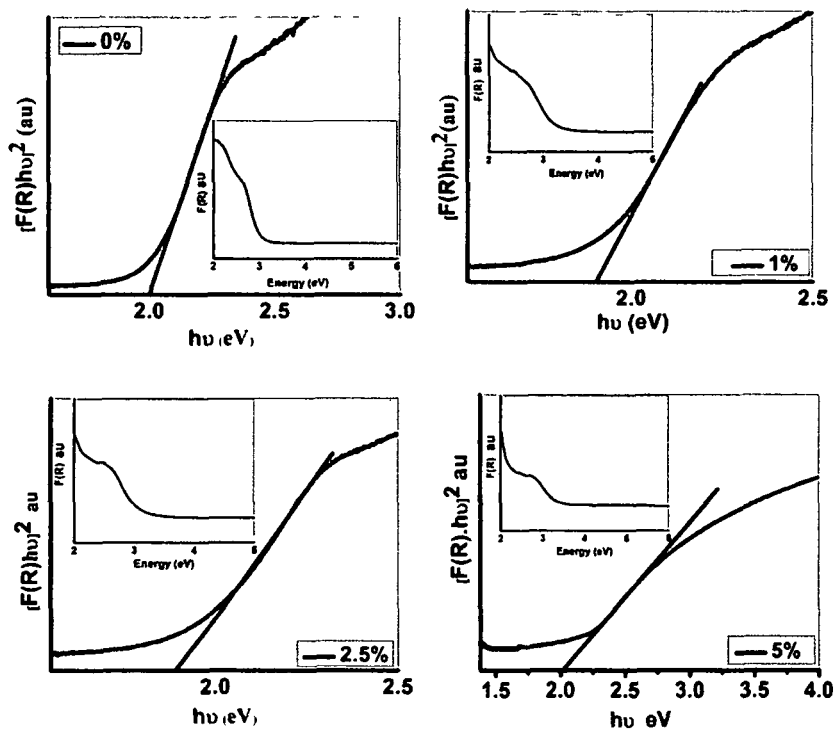


Figure 3.8: Band gap calculation of pristine and doped CdSe nanoparticles

Chapter III

Since Mn^{2+} has no spin allowed ligand field transitions, only the transitions for CdSe were observed in the F(R) versus energy curves for all the doping concentrations. Band gap of the nanoparticles decrease for 1 % and 2.5 % doping concentrations. But for doping concentration 5 %, band gap of the nanoparticles again increased than that for pristine ones. The table for band gaps is shown below :

Table 3.1: Band gap of pristine and Mn doped CdSe nanoparticles

Sample name	Band gap (eV)
CdSe	2
1 % Mn CdSe	1.90
2.5 % Mn CdSe	1.89
5 % Mn CdSe	2.02

XRD pattern is shown in Figure 3.9. First peak is shown in inset. Displacement of the peaks can be clearly seen towards higher angle. This shift in the position of first peak of XRD pattern confirmed that manganese ions replaced cadmium ions from their positions and occupied the corresponding positions in the lattice. First peak of XRD shifts towards higher angle indicating lattice contraction. However, peaks are broadened due to small crystal dimensions [6]. And lattice contraction is maximum for 1 % doping concentration. Crystallite size and strain in the nanoparticles are calculated by Williamson-Hall plot shown in Figure 3.10. With increase in the doping concentration to 1 %, 2.5 % and 5 %, negative strain started to decrease and lattice constants gradually increased. Here lattice constant is calculated for all the peaks in XRD and then an average is taken. Ionic radius of manganese (Mn^{2+}) is 70 pm and that of cadmium (Cd^{2+}) is 99 pm. When a manganese ion replaces a cadmium ion lattice strain is generated in the crystal and lattice contracts. For 1 % and 2.5 % manganese doping it can be seen that crystallite size decreased and lattice constant also decreased. Lattice contraction is highest for 1 % doping. The reason for increase in crystallite size for 5 % doping may be is that for this amount of Mn^{2+} a

Chapter III

phenomenon called self purification occurs in CdSe nanocrystals [7]. For this reason Mn^{2+} ions were not properly incorporated inside the crystal and so lattice contraction is least. Table for crystallite size, strain and lattice constant is shown in table 3.2.

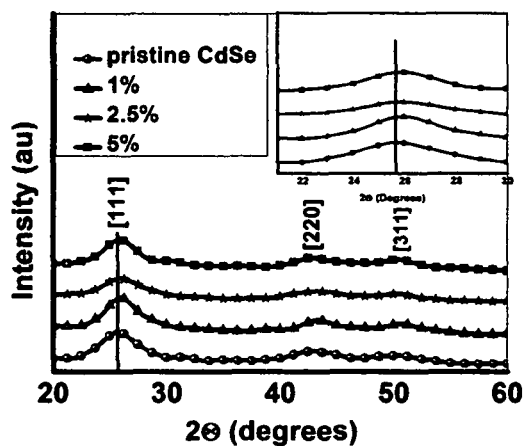


Figure 3.9: XRD pattern of pristine and doped CdSe nanoparticles

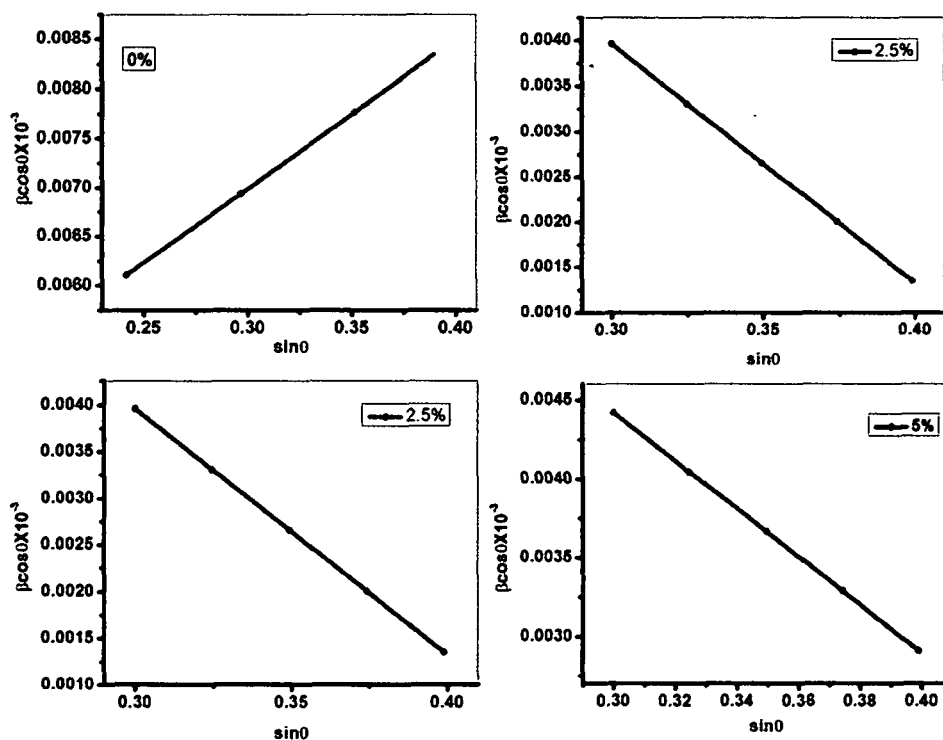


Figure 3.10: Williamson-Hall plot for pristine and doped CdSe nanoparticles

Chapter III

PL spectra of the pristine and Mn doped CdSe nanoparticles are shown in Figure 3.11. Luminescence of manganese doped CdSe at 620 nm is not due to band to band transition that is not due to the electron transition from conduction band also called lowest unoccupied molecular orbital composed of selenium (Se) 4P to the valence band i.e. highest occupied molecular orbital composed of cadmium (Cd) 5S. This luminescence is attributed to the defects present in the system that is selenium vacancies. In case of CdSe nanoparticles if the size of the nanoparticles is higher than 3.3 nm then Mn^{2+} transition is absent in the luminescence spectra because in that case Mn^{2+} states are present above the excitonic levels. It can be seen from the luminescence spectra that luminescence peak for dopant concentration 5 % is not quenched and shows more intense peak than the other two concentrations. It has already found that only when the dopants are not properly incorporated inside the host material, the luminescence shows intense peak [8].

TABLE 3.2: Comparison table of crystallite size and strain for doped and undoped samples

Sample name	Crystallite size nm	Strain $\times 10^{-3}$	Lattice constant, Å	
			a	c
CdSe	4	0.151	8.66	11.51
1% Mn CdSe	2.6	-5.5549	4.5	7.01
2.5% Mn CdSe	3	-0.1985	5.54	8.10
5% Mn CdSe	6	-0.05173	8.87	11.96

The local electronic structures of Mn ions in such II-VI semiconductor crystals are generally described well by ligand field theory. Mn^{2+} has five 3d electrons. The ground state is split into six Zeeman components ($\pm 1/2, \pm 3/2, \pm 5/2$) as shown in Figure 3.12

[9,10]. The ${}^4T_1 \rightarrow {}^6A_1$ ligand field transition is responsible for the characteristic luminescence of Mn^{2+} ions in doped II-VI crystals. But in our case of CdSe nanoparticles, Mn^{2+} PL emission is not seen. Mn-doped II-VI semiconductor nanocrystals are organized into three distinct categories according to the nature of their lowest energy excited state, which determines their resulting photophysical properties [11-17].

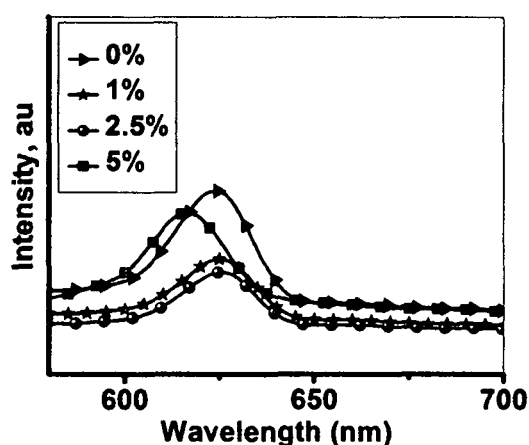


Figure 3.11: Photoluminescence spectra of pristine and doped CdSe nanoparticle

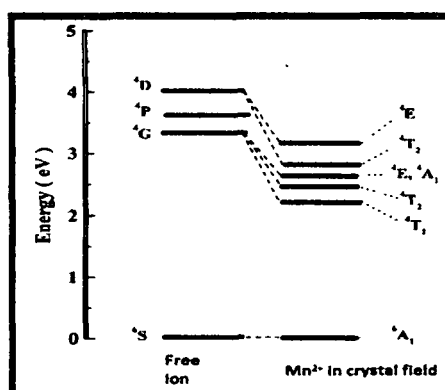


Figure 3.12: Schematic diagram of the splitting excited states of $3d^5$ level for a Mn^{2+} ion in presence of a tetrahedral crystal field (Ref 7)

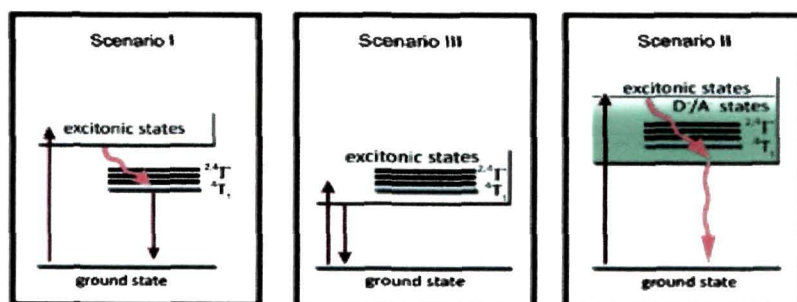


Figure 3.13: Scenarios of PL emission in different nanoparticles (Ref 8)

In scenario I, Mn^{2+} ligand-field excited states are lowest in energy and within the band gap (e.g., Mn^{2+} doped ZnS, CdS, and ZnSe etc). In scenario II, Mn^{2+} photoionization excited states are lowest in energy and within the gap (e.g., Mn^{2+} doped ZnO). In scenario III: semiconductor excitonic excited states are lowest in energy (Mn^{2+} excited states are outside the gap, e.g., Mn doped CdSe) as shown in Figure 3.13. Mn doped CdSe QDs differ from all other doped semiconductor nanocrystals in that they are the first that have allowed tuning of the semiconductor band gap energy across the dopant excited state levels. In PL spectra of Mn doped CdSe QDs, the characteristic $Mn^{2+} \ ^4T_1$ emission is observed when the bandgap energy is greater than the $Mn^{2+} \ ^4T_1$ excited state energy as shown in Figure 3.14. With decrease in nanocrystal diameter dopants are excluded from the nanocrystal below critical nuclei and hence for smaller sized undoped nanocrystals are found. Energy of the excitonic transition depends strongly on particle size, but the energy of the localized Mn^{2+} transition does not. The nature of the emissive state changes at $d \approx 3.3$ nm, marking the cross-over between scenarios I and III. Although scenarios I and III both also exist among bulk DMSs, these Mn doped CdSe QDs are unique in that they allow tuning from one scenario to the other quite readily, simply by changing the nanocrystal diameter. Although only vacancy related emission is observed in Mn doped CdSe QDs in the present case, the properties of this luminescence are still fundamentally altered by the presence of the Mn^{2+} ions.

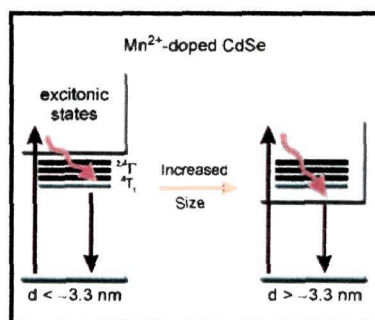


Figure 3.14: PL emission in Mn doped CdSe dependent upon size of the nanocrystal (Ref 8)

So, it was seen that Mn doped CdSe nanoparticles with diameter higher than 3.3 nm do not show pseudo-tetrahedral Mn²⁺ (${}^4T_1 \rightarrow {}^6A_1$) transitions. But it is observed that presence of Mn dopant leads to decrease in luminescence intensity. The reason behind partial quenching of photoluminescence intensity is may be due to the shrinking distance between the dopant-dopant or presence of deep Mn³⁺ neutral state that facilitates nonradiative recombination of band-edge electrons and holes [18-20]. Since, any Mn³⁺ related phase was not found in XRD pattern, so shrinkage in Mn-Mn distance should be the reason for partial quenching of PL intensity.

Raman spectra of pristine and doped CdSe nanoparticles were also studied by Renishaw Invia Raman spectrometer. Figure 3.15 shows the Raman spectra of pristine and Mn doped CdSe samples. Raman spectroscopy is a non-destructive method for studying vibrational and electronic states of a confined system. The Raman effect arises when an intense monochromatic radiation undergo inelastic scattering on passing through a sample containing molecules and result in the change in molecular polarizability on vibration. When a sample is irradiated with incident light of frequency ν_0 , the scattered light is shifted by frequency $\nu(\nu_0+\nu)$. Raman scattering light undergoing a frequency shift $(\nu_0-\nu)$ (longer wavelength) are known as Stoke's light and scattered light with frequency shift $(\nu_0+\nu)$ (shorter wavelength) are called Anti-Stoke's light. The frequency shift is attributed to transfer of energy due to lattice vibrations, molecular vibrations and rotations of molecules and electronic transitions. Raman studies on nanoparticles revealed that whenever a system goes from bulk to nano a wavenumber shift and

Chapter III

broadening of Raman peaks is observed. Since CdSe nanoparticles are spherical in shape so on the basis of Heisenberg uncertainty principal, $\Delta x \Delta p \geq \hbar^2/4$ it can be said that with decrease in grain size, the phonon position is confined in the particle size Δx and the phonon momentum distribution Δp will increase. Here, $\hbar = h/2\pi$, h is the Planck's constant. The broadening of the phonon momentum leads to a broadening of scattered phonon momentum according to the law of conservation of momentum. And this may lead to shift of the Raman lines [21]. In the present case, longitudinal optical phonon (LO) is observed near 280 cm^{-1} . That is Raman spectra of CdSe nanoparticles are blue shifted than their bulk counterpart due to phonon confinement as explained above. For bulk CdSe LO phonon mode is observed at 210 cm^{-1} . Position of the peaks slightly changed due to doping. Deviation in the spectra due to doping is also seen in the intensity of the spectra. This is because now the manganese ions have replaced some of the cadmium ions and lattice contraction occurred.

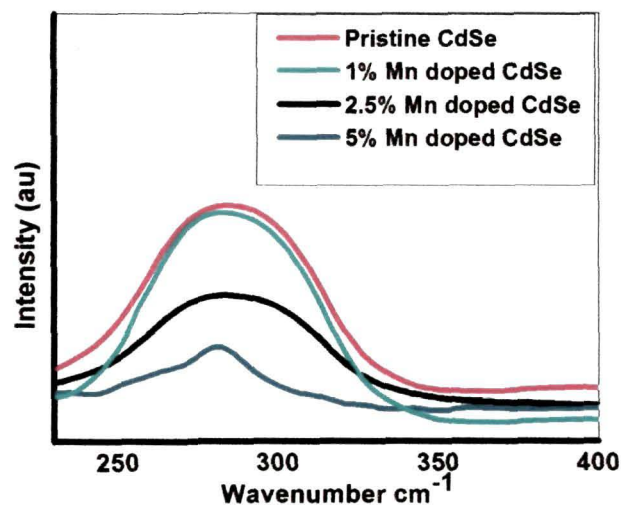


Figure 3.15: Raman spectra of Mn doped CdSe nanoparticles

3.3 Origin of ferromagnetism in Doped CdSe nanoparticles

To investigate oxidation state of the dopant and to know whether dopant ions are incorporated inside the nanocrystal or not EPR spectroscopy was done. EPR spectroscopy gives local electronic structure of dopant ion in the host crystal. Traces of Mn^{2+} doped in II-VI bulk semiconductors result in numbers of isolated tetrahedrally co-ordinated Mn^{2+} ions. From Figure 3.16, it was seen that EPR spectra of 2.5 % and 5 % doping is well defined. EPR spectroscopy of 1 % doping is actually composed of two spectra with a hyperfine structure with six lines and a broad spectrum.

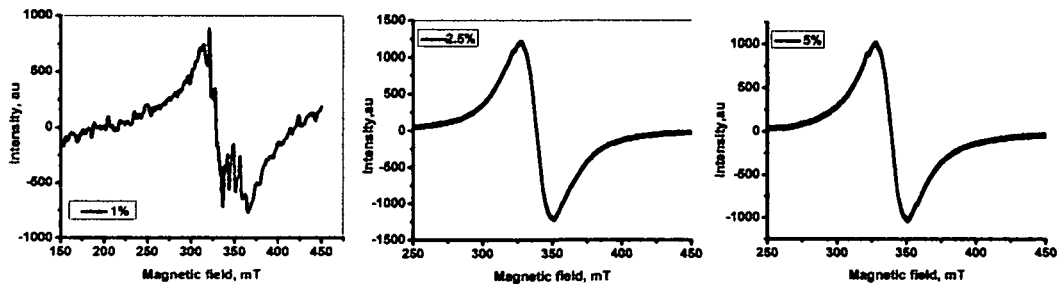


Figure 3.16: EPR spectra of Mn doped CdSe nanoparticles

The smaller Mn^{2+} ion is expected to distort the CdSe lattice by replacing Cd^{2+} . The EPR data suggest that the Mn site is trigonally or tetragonally distorted which leads to the observation of forbidden EPR transitions. These transitions are attributed to a stronger spin-orbit term arising from symmetry breaking and are assigned to $-\frac{1}{2} \rightarrow \frac{1}{2}$ / spin-spin interactions [23, 24]. Six line pattern is from the Mn nucleus ($J=5/2$) and corresponds to the transition of $M_s=\pm 1$ and $M_I=0$ where M_s and M_I are electron spin and nuclear spin quantum numbers, respectively. The Mn-Mn interaction which inversely related to the hyperfine interactions becomes stronger as more and more Mn ions are introduced into CdSe nanoparticles. A broadening effect is seen with increase in Mn concentration. This broadening effect with increase in Mn concentration is due to Mn-Mn interaction.

Magnetic hysteresis (M-H) loops at room temperature for all the three doping concentrations of manganese in CdSe nanoparticles are shown in Figure 3.17 and zoomed

image is shown in Figure 3.18. Magnetic properties are analyzed in a superconducting quantum interference device (SQUID) (Quantum Design MPMS SQUID VSM Evercool system, USA). SQUID is based on Josephson effect to measure small variations in magnetic flux. SQUID is a ring of superconductor cut short by one or more Josephson junctions [25]. The superconducting magnetic coil produces the magnetic field. The sample is moved through the pick-up coils by means of a hydraulic system. Magnetic moment of sample induces a magnetic flux change in the pick-up coils into the SQUID [26].

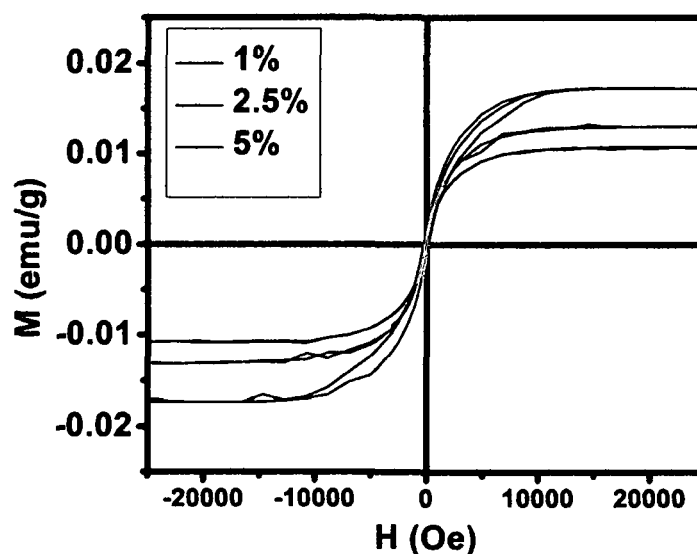


Figure 3.17: M-H curves for Mn doped CdSe nanoparticles

The origin of ferromagnetism in II-VI (CdSe, CdTe etc) doped semiconductors comes from the spin exchange interaction between the Mn-ions mediated by the carriers (conduction-band electrons or valence-band holes), in particular through the sp-d exchange interaction [27]. In spite of the fact that Mn differs from the group-II cations by the $3d^5$ shell which is only half-filled, Mn can contribute its $4s^2$ electrons to the $s-p^3$ bonding. Therefore, Mn can substitute the group-II elements in wurtzite or zinc blende structures. Following Hund's rule, these five d-electrons have parallel spins that adding another electron with opposite spin to the manganese (Mn) atom needs a considerably

Chapter III

large energy. As a result, the $3d^5$ orbit is stable and the Mn-atom resembles a group-II element. In the II-VI doped semiconductors, the Mn-ion is isoelectronic which means that no additional electric field is created and the number of carriers is conserved. Besides, the polarity of the elements in II-VI group is strong. This makes them attractive for interesting optical properties. The magnetic interaction in II-VI doped semiconductors is dominated by antiferromagnetic exchange between the Mn spins, which results in paramagnetic, spin glass, and ultimately long-range antiferromagnetic behavior. Incorporated Mn doped CdSe [28] nanoparticles are expected to be good candidates to achieve suitable nanoscaled ferromagnetism [29,30].

Coercivity and saturation magnetization were found to be 196, 69, 67 Oe and 0.010, 0.013, 0.017 emu/g were for 1 %, 2.5 % and 5 % doping concentration respectively. The coercivity decreases with increase in doping concentration. The saturation magnetization (M_s) values of the three samples were found to increase with increasing doping but M_s per dopant decreases with increase in doping concentration.

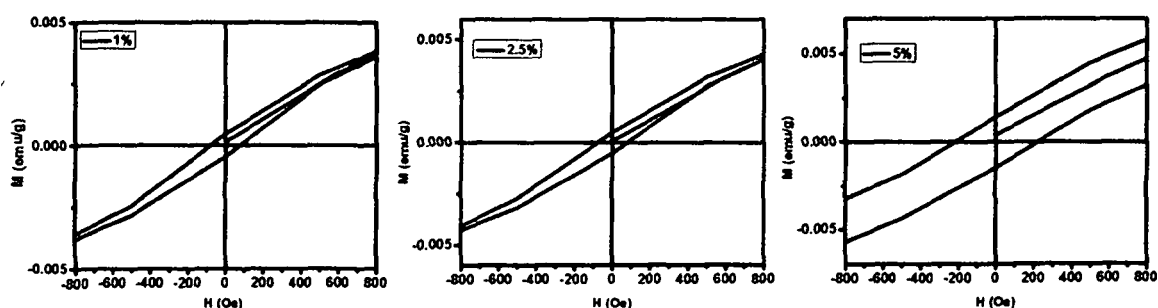


Figure 3.18: Zoomed image of M-H curves of Mn doped CdSe nanoparticles

Ferromagnetism ordering may arise due to many possible reasons. One origin is small secondary phases of manganese such as ferromagnetic Mn_3O_4 . But in XRD confirms absence of any secondary oxide phases as shown in Figure 3.9 and EDX also confirms absence of oxygen and other magnetic impurities as described in chapter II Figure 2.5. Another origin may be carrier mediated ferromagnetic Ruderman-Kittel-Kasuya-Yosida

(RKKY) mechanism of spin-spin exchange interaction. But with such low doping RKKY interaction is not possible. Low carrier densities of II-VI doped semiconductor nanoparticles are usually paramagnetic but neighbor Mn-Mn pairs are antiferromagnetically coupled or even blocked owing to short range superexchange interactions but RTFM is found in the present case. In addition to superexchange coupling, strong spin dependent coupling (sp-d) exchange interaction between the band of host semiconductor (sp-state) and magnetic moments (d-state) exists in Mn doped CdSe nanoparticles [31]. The antiferromagnetic coupling in these nanoparticles can be overcompensated by ferromagnetic interactions mediated by holes. In the presence of band carriers, the RKKY mechanism of spin-spin exchange interaction operates. But RKKY interaction is possible only if there are sufficient carriers in the system. But CdSe do not have sufficient carriers with such low doping. So, there may be an alternative F-centre mediated exchange mechanism responsible for this system. An F-centre is a selenium vacancy with a trapped electron. Presence of selenium vacancy is also confirmed from PL spectra. This trapped electron occupies an extensive orbital state that overlaps with the d shells of some nearby transition metal atoms. The radius of this trapped electron orbital is predictable to be of the order of a_0 , where a_0 is the Bohr radius [32]. This pair is called bound magnetic polaron (BMP). The BMP will align in a parallel arrangement with the surrounding individual dopant ion spins by sp-d exchange interaction. This implies that the electronic states of the carriers are delocalized and extended, and when the concentration exceeds a certain value, ferromagnetism may be expected.

3.4 Conclusion

Novel findings of the chapter III is summarized in the following points:

1. pH dependent properties are seen in CdSe nanoparticles. At pH 11, CdSe nanoparticles show highest luminescence. In TGA capped CdSe nanoparticles, some of the TGA molecules may depart from the CdSe nanoparticles into the solvent until a dynamic equilibrium is established between desorption and

Chapter III

absorption. At pH 11, this equilibrium is established between the adsorbing and desorbing of TGA from the NPs surfaces.

2. XRD confirms successful substitutional doping and absence of any oxide phases of manganese. Shifting of the first XRD peak towards higher angle indicating lattice contraction due to replacement of larger Cd^{2+} ions by manganese.
3. Mn^{2+} doping in CdSe nanoparticles leads to partial quenching of PL intensity for 1 % and 2.5 % dopant concentration due to shrinking distance between Mn-Mn. But for 5 % luminescence intensity increases due to improper incorporation of dopants inside host.
4. In EPR spectroscopy, hyperfine splitting was seen in 1 % Mn doped CdSe nanoparticles. EPR spectra confirm presence Mn^{2+} in CdSe nanoparticles.
5. Room temperature ferromagnetism is found in Mn doped CdSe which is ascribed to bound magnetic polaron mediated sp-d exchange interactions.

References:

1. Murphy, A.B. Band-gap determination from diffuse reflectance measurements of semiconductor films, and application to photoelectrochemical water-splitting, *Sol Energ. Mat. Sol. C*, **91** (14), 1326--1337, 2007.
2. Kasap, S. & Capper, P. *Springer Handbook of Electronic and Photonic Materials*, Springer, UK, 2006.
3. Vaseashta, A.K., Mihailescu, I.N. (Ed.) *Functionalized Nanoscale Materials, Devices and Systems*, proceedings of NATO Advanced Study Institute (ASI) titled "Functionalized Nanoscale Materials, Devices, and Systems for chem.-bio Sensors, Photonics, and Energy Generation and Storage", Springer, Netherlands, 2008.
4. Zeng, J. et al. Fine tuning photoluminescence properties of CdSe nanoparticles by surface states modulation, *J. Colloid. Interface. Sci.* **298** (2), 685--688, 2006.

Chapter III

5. Mandal, A., Tamai, N. Influence of Acid on Luminescence Properties of Thioglycolic Acid-Capped CdTe Quantum Dots, *J. Phys. Chem. C* **112** (22), 8244--8250, 2008.
6. Raola, O.E. & Strouse, G.F. Synthesis and Characterization of Eu-Doped Cadmium Selenide Nanocrystals, *Nano Lett.* **2** (12), 1443--1447, 2002.
7. Gustavo, M. et al. Self-Purification in Semiconductor Nanocrystals, *Phys. Rev. Lett.* **96** (22), 226802--226896, 2006.
8. Leung, K. & Whaley, B. Surface relaxation in CdSe nanocrystals, *Journal of Chem. Phys.* **110** (22), 11012--11022, 1999.
9. Furdyna, J.K. Diluted magnetic Semiconductors, *J. Appl. Phys.* **64** (4), 29--64, 1988.
10. Tanaka, M. Photoluminescence properties of Mn²⁺-doped II--VI semiconductor nanocrystals, *J. Lumin.* **100** (1-4), 163--173, 2002.
11. Beaulac, R. et al. Luminescence in colloidal Mn²⁺-doped semiconductor nanocrystals, *J. Solid State Chem.* **181** (7), 1582--1589, 2008.
12. Beaulac, R. et al. Mn²⁺-Doped CdSe Quantum Dots: New Inorganic Materials for Spin-Electronics and Spin-Photonics, *Adv. Funct. Mater.* **18** (24), 3873--389, 2008.
13. Nag, A. et al. Size-Dependent Tuning of Mn²⁺ d Emission in Mn²⁺-Doped CdS Nanocrystals: Bulk vs Surface, *J. Phys. Chem. C* **114** (43), 18323--18329, 2010.
14. Beaulac, R. et al. Spin-Polarizable Excitonic Luminescence in Colloidal Mn²⁺ Doped CdSe Quantum Dots, *Nano Lett.* **8** (4), 1198--1201, 2008.
15. Leung, K., Whaley, K. Surface relaxation in CdSe nanocrystals, *J. Chem. Phys.* **110** (22), 11012--11022, 1999.
16. Levy, L. et al. Isolated Mn²⁺ ions in CdS, *Langmuir* **15** (10), 3386--3389, 1999.
17. Yang, H et al. Synthesis and application of Mn doped II-VI semiconductor nanocrystal, *J. Nanosci. Nanotech.* **5** (9), 1364--1375, 2005.
18. Bang, H et al. Concentration quenching of Eu-related luminescence in Eu-doped GaN, *Appl. Phys. Lett.* **85** (2), 227, 2004.
19. Lee, D.S. et al. Optimum Er concentration for in situ doped GaN visible and infrared luminescence, *Appl. Phys. Lett.* **79** (6), 719--721, 2001.

Chapter III

20. Radovanovic, P. et al. General synthesis of Manganese-doped II-VI and III-V semiconductor nanowires, *Nano. Lett.* **5** (7), 1407--1411, 2005.
21. Xu, C. et al. Blue shift of Raman peak from coated TiO₂ nanoparticles, *J. Raman Spectrosc.* **32** (10), 862--865, 2001.
22. Dzhagan, V. et al. Size effects on Raman spectra of small CdSe nanoparticles in polymer films, *Nanotechnology* **19** (30), 305707--305712, 2008.
23. Iragashi, T. et al. Characterization of Mn²⁺ coordination of Mn²⁺ coordination states in ZnS nanocrystal by EPR spectroscopy and related photoluminescence properties, *J. Nanopart. Res.* **3** (1), 51--56, 2001.
24. Magana, D. Synthesis and characterization of dilute magnetic semiconductors nanoparticles, Ph. D. Thesis, Florida State University, USA, 2007.
25. Fagaly, R.L. Superconducting quantum interference device instruments and applications, *Rev. Sci. Instrum.* **77** (10), 101101, 2006.
26. Gramm, K. et al. SQUID magnetometer for magnetization measurements, *Phys. Scr.* **13** (2), 93--95, 1976.
27. Nguyen, NTT. Quantum dots doped with few magnetic impurities, Ph. D. Thesis, University of Antwerp, Belgium, 2010.
28. Haury, A. et al. Observation of a Ferromagnetic Transition Induced by Two-Dimensional Hole Gas in Modulation-Doped CdMnTe Quantum Wells, *Phys. Rev. Lett.* **79** (3), 511--514, 1997.
29. Boukari, H. et al. Light and Electric Field Control of Ferromagnetism in Magnetic Quantum Structures, *Phys. Rev. Lett.* **88** (20), 207204--4, 2002.
30. D. Ferrand, D. et al. Carrier-induced ferromagnetism in p-Zn_{1-x}Mn_xTe, *Phys. Rev. B* **63**, 085201--13, 2001.
31. Shinjo, T. et al. *Nanomagnetism and spintronics*, Elsevier, Netherlands, 2009.
32. Kumar, S. et al. Magnetic and structural characterization of transition metal co-doped CdS nanoparticles, *Appl. Nanosci.* **2** (2), 127--131, 2012.

**Chapter IV: Changes in structural, optical &
magnetic properties of Cadmium Oxide nanoparticles
induced by annealing and doping**

4.1 Enhanced visible luminescence and modification in morphological properties of cadmium oxide nanoparticles induced by annealing

Cadmium oxide (CdO) nanoparticles are synthesized by a simple sol-gel synthesis method as described in section 2.2.1 of chapter II. They showed luminescence properties in visible region of electromagnetic spectrum. Both blue and green emissions were observed in PL spectra. Structural, optical and electrical properties were investigated by changing annealing temperature of the samples. Changes in luminescence intensity due to cadmium interstitial and oxygen vacancy defects of nanoparticles were realized when these particles were annealed at three different temperatures. XRD confirmed annealing induced changes in morphological properties. A good correlation between all the experimental results was obtained.

4.1.1 Diffuse reflectance spectroscopy

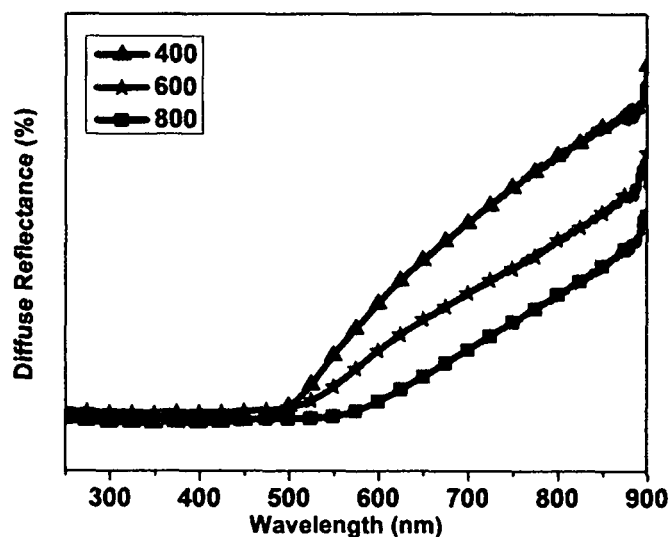


Figure 4.1: Diffuse reflectance spectra of CdO nanoparticles annealed at three different temperatures

Chapter IV

CdO nanoparticles are synthesized by sol-gel method as explained in section 2.2.1 of chapter II. These nanoparticles are annealed at three different temperatures 400 °C, 600 °C and 800 °C. Comparison of diffuse reflectance spectra of these powder nanoparticles are shown in the above Figure 4.1. Figure 4.2 (a) and (b) are Tauc's plots of all three samples derived from using Kubelka-Munk function $F(R)$ where $F(R)=(1-R)^2/2R$, R is the reflectance in percentage [1-3]. Figure 4.2 (a) is the Tauc's for calculation of direct band gap CdO nanoparticles and Figure 4.2 (b) is for indirect band gap.

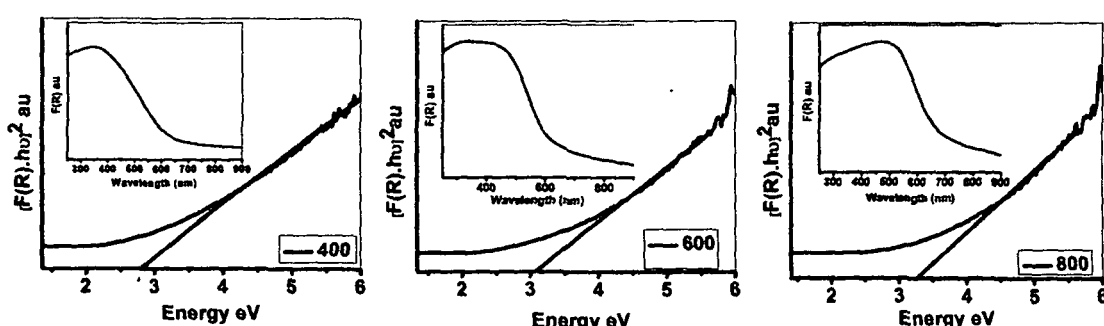


Figure 4.2 (a): Tauc's plot for determination of direct band gap of CdO nanoparticles

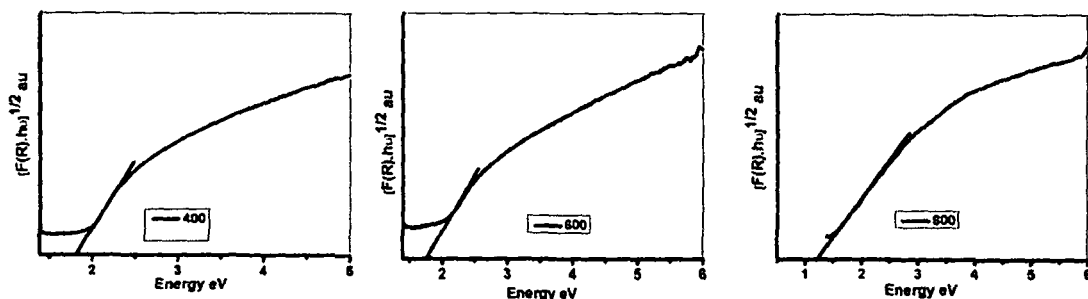


Figure 4.2 (b): Tauc's plot for determination of indirect band gap of CdO nanoparticles

Urbach Energy is calculated from $F(R)$ vs $h\nu$ plot using the relation,

$$\alpha(E) = \alpha_0 \exp(E - E_g) / E_0$$

where E_0 is the characteristic width of the absorption edge called Urbach parameter, E_g is the optical band gap [4]. Figure 4.3 is the Urbach energy plot for all the three samples.

Chapter IV

Calculated values of Urbach energies and band gaps are summarized in table 4.1. It is seen that direct band gap (DBG) increases with increase in annealing temperature while indirect band gap (IBG) decreases. Urbach energy also decreases with increase in annealing temperature. Increase in direct band gap and decrease in indirect band gap signifies that total defect states in the system decreased with increase in annealing temperature. Since Urbach energy is a measure of defects in the system and so decrease in Urbach energy implies that number of defects in the system decrease with increase in annealing temperature.

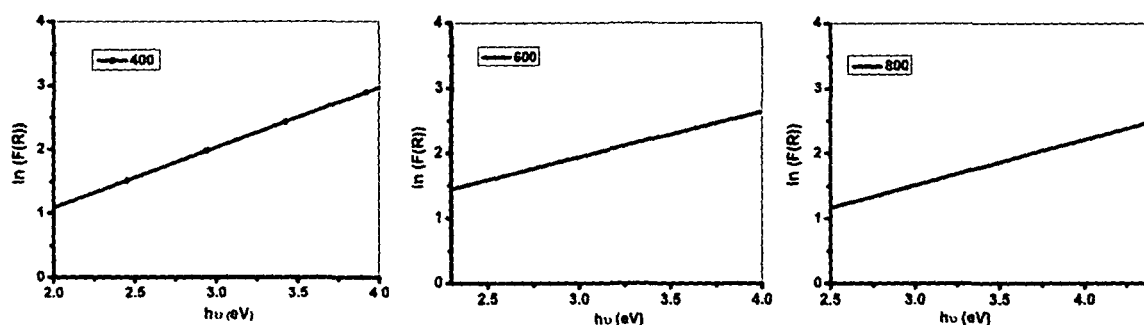


Figure 4.3: $\ln [F(R)]$ versus incident photon energy $h\nu$ for CdO nanoparticles annealed at three different temperatures

TABLE 4.1: Comparison of direct band gap, indirect band gap and Urbach energy

Sample name	Direct Band gap (DBG), E_{DBG} eV	Indirect Band gap (IBG), E_{IBG} eV	Urbach Energy, eV
400	2.8	1.81	0.94
600	3.08	1.74	0.70
800	3.24	1.19	0.69

4.1.2 Photoluminescence spectroscopy

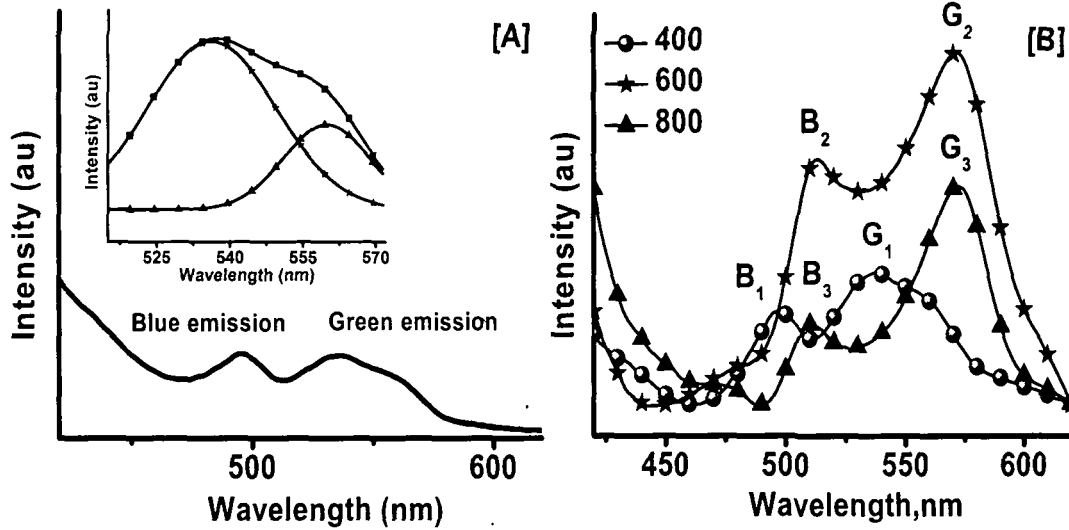


Figure 4.4: (a) PL spectroscopy of CdO nanoparticle and (b) Comparison of PL spectra of CdO nanoparticles annealed at three different temperatures

From PL spectra (Figure 4.4 (A)) of CdO nanoparticles annealed at 400 °C, it was found that the green emitting peak is actually composed of two peaks. The deconvoluted green peak is shown in inset. PL spectra of CdO nanoparticles have both green and blue emissions which are the results of emissions from oxygen vacancy and interstitial vacancies [5]. In a crystal, a certain number of defects always present, because entropy is increased by the presence of disorder in the structure [6]. Oxygen vacancies create deep levels and Cd-interstitials are shallow donors in CdO nanoparticles. Cd-interstitials are Frenkel type defects. These defects can move outward. Let us consider blue and green peaks of samples annealed at 400, 600 and 800 °C as B₁, B₂, B₃ and G₁, G₂, G₃ respectively. Then the ratio of the intensity of the peaks are B₁/ B₂=0.54, B₁/ B₃=1.15, G₁/ G₂=0.44, G₁/ G₃=0.30. In Figure 4.4 (A), green peak as stated above consists of two peaks. This may be ascribed to emission from two different levels of oxygen vacancy defect states. From Figure 4.4 (B), it was found that annealing slightly red-shifted the emission peak positions for samples annealed at 600 and 800 °C samples. Red shifting can be ascribed to increase in particle size. Intensity of blue emitting peak of 600 °C sample was increased to a greater extent. But it was decreased for 800 °C sample than that for 400 °C sample. Intensity

of Green peak of both 600 ° and 800 °C samples increased than that of 400 °C. This is because annealing at 600 °C increases the number of Cd- interstitial vacancies by providing enough ionization energy. At this temperature Cd-interstitial vacancies, which are Frenkel defects get enough thermal energy to diffuse through the crystal and go to the surface which in turn increases blue peak intensity. But these defects are unstable in comparison to oxygen vacancy defects. At high temperature i.e. at 800 °C oxygen vacancies predominate. It may be possible that at 800 °C, Cd-interstitials get oxidized. Hence intensity of green peak of the samples increased while blue peak decreased. Because at this temperature possibility of electrons to jump down to the oxygen vacancy levels increases as now there are lesser number of Cd-interstitial defects within band gap.

4.1.3 X-ray diffraction studies

Morphological properties were studied by XRD. XRD studies have been done to find the crystal structure as shown in Figure 4.5. From Williamson-Hall plot as shown in Figure 4.6, crystallite size and strain were calculated [7]. Lattice parameter of CdO samples are calculated by using the Nelson–Riley Parameter [8] given by,

$$NRF=1/2[\text{Cos}^2\theta/\sin\theta+\text{cos}^2\theta/\theta]$$

where θ = Bragg angle. By extrapolating the lines to $NRF=0$, the true lattice parameter is obtained as shown in Figure 4.7.

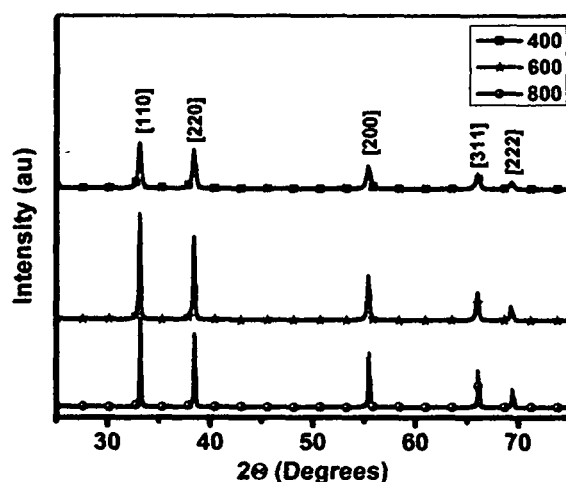


Figure 4.5: XRD pattern of CdO nanoparticles annealed at different temperatures

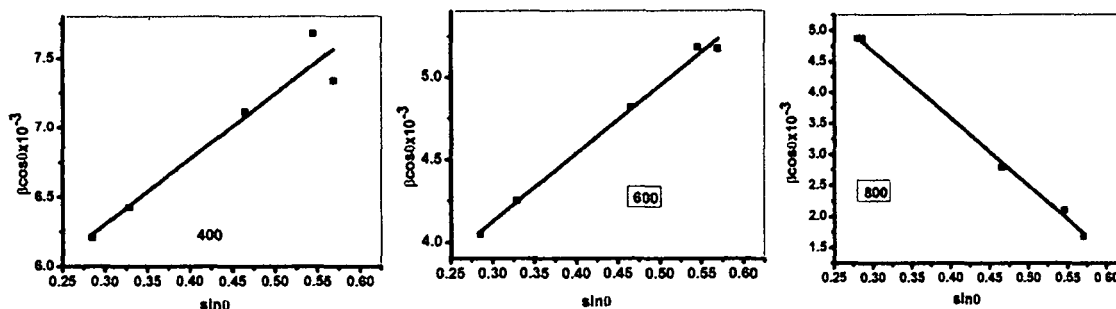


Figure 4.6: Williamson-Hall plot of all three CdO nanoparticle samples annealed at different temperatures

Comparison between lattice constant, crystallite size, interplanar distance and strain of the nanoparticles are shown in TABLE 4.2. Lattice constant and interplanar distance of the nanoparticles continues to decrease with increase in annealing temperature. Although crystallite size first increases then slightly decrease with temperature. Change in lattice constant may be due to change in particle size with annealing. Annealing leads to change in number of oxygen vacancies or defects in the system which in turn changes the lattice constant, interplanar distance and strain in the nanoparticles.

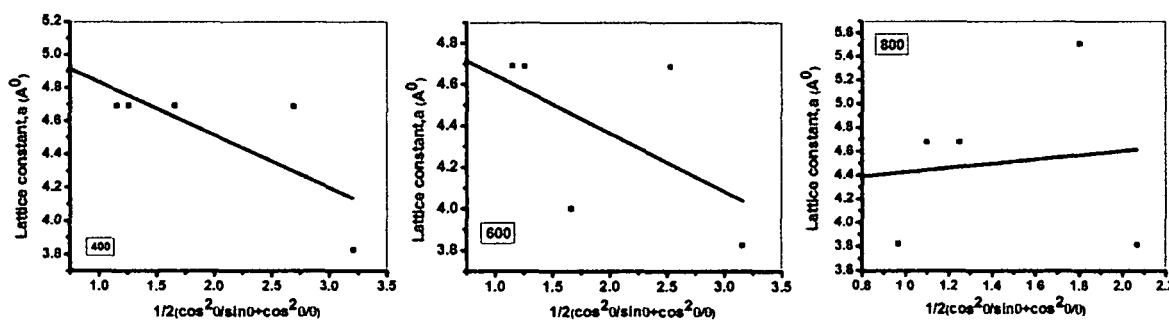


Figure 4.7: Lattice constant vs NRF of CdO nanoparticles

TABLE 4.2: Comparison between lattice constant, Interplanar spacing, Crystallite size & Strain

Sample name	Lattice constant, Å	Interplanar spacing, d nm	Crystallite Size, nm	Strain×10 ⁻³
400	4.8	0.34	24	4.68
600	4.71	0.33	37	4.11
800	4.38	0.31	31	-10.87

4.1.4 I-V measurements

I-V measurements of the samples were done by using a Keithley electrometer automatic system. Pellets were made from all the three samples and conductivity measurements were taken after making contact with silver paste. I-V curve shows linear relationship showing the contact to be Ohmic. The electrical conductivity of the samples are measured by using the following relation, $\Omega = l/A (dI/dV)$ where l is the thickness of the sample and A is the area of the sample. Slope of the graph (Figure 4.8) gives (dI/dV) [9]. Conductivities of all the samples are given in table 4.3. Conductivities of the CdO nanoparticles for the samples gradually increase with increase in annealing temperature as shown in Figure 4.8. This type of behavior is expected for n-type intrinsic semiconductors.

TABLE 4.3: Conductivity of CdO nanoparticle

Sample name	Conductivity $\Omega^{-1} \text{ cm}^{-1}$
400	0.0075
600	0.0015
800	0.02

It was seen that a certain amount of defects were present in the system. Here, annealing leads to increase in oxygen vacancies in the CdO nanoparticles. These oxygen vacancies capture electrons forming V^+ centres. In electrical conductivity, electrons trapped in oxygen vacancies also contribute. As the temperature of the samples was increased trapped electrons get sufficient thermal energy and go to the conduction band and become free electrons. So oxygen vacancies greatly contribute to electrical conductivity. With increase in annealing temperature amorphous phase in the nanoparticles decreases and crystallite size increases. Also, scattering in grain boundary is reduced with increase in annealing temperature. Hence conductivity increases.

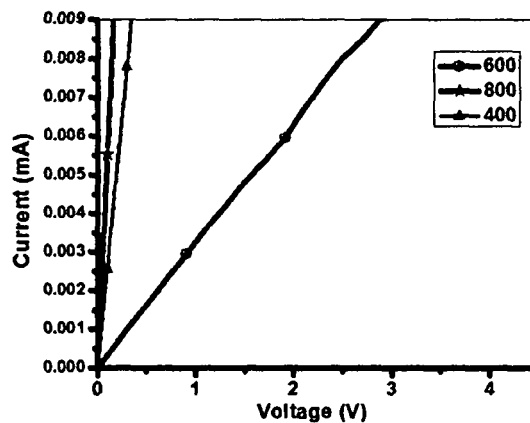


Figure 4.8: Current vs Voltage plot of CdO nanoparticles

Chapter IV

4.1.5 Hall-effect

The Lorentz force law is given by, $F=q(E+v \times B)$. This equation states that a force (F) will be exerted when a magnetic field (B) intersects a moving charge (q) with velocity v as shown in Figure 4.9 below. Therefore, if a current (I) is run through the sample (palette) and a magnetic field is generated perpendicular to the current, then a force will occur on electrons moving through the material [10]. This will generate a potential perpendicular to both the current and the field, known as the Hall Voltage (V_H , Hall, E. H.1879), defined by $V_H = -IB/dne$ where d is the thickness of the strip, n is the density of charge carriers, and e is the charge of an electron. Given this, n is calculated by $n = -IB/deV_H$. Hall co-efficient, $R_H = 1/nq$.

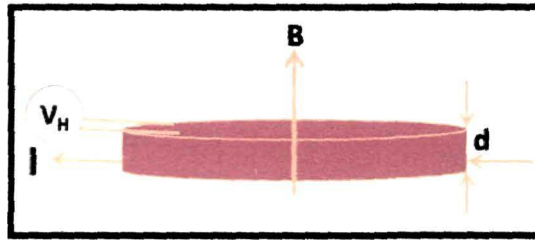


Figure 4.9: Schematic diagram of Hall-effect

Measurements were taken by a standard laboratory set up where contacts are provided by silver paint. From the slope of the graph between Hall voltage and magnetic field gives Hall co-efficient from which charge concentration can be calculated. Hall voltage versus magnetic fields graphs are shown in Figure 4.10. Hall co-efficient and charge concentration of the samples are given in table 4.4.

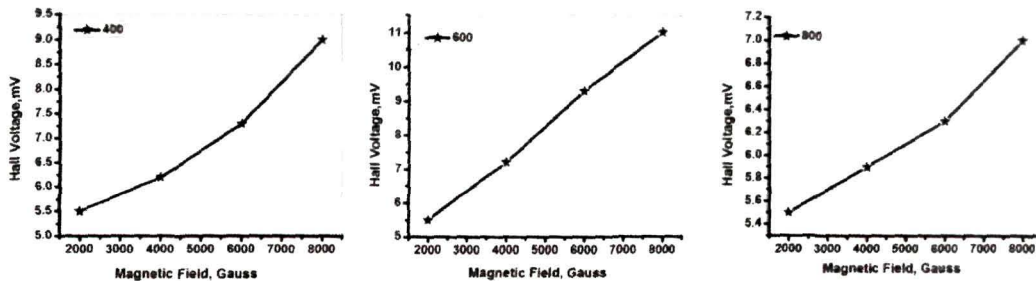


Figure 4.10: Hall Voltage vs Magnetic field of all three CdO nanoparticle samples

TABLE 4.4: Hall co-efficient and charge density of the samples

Sample name	Hall co-efficient	Charge density /m³
400	9.3×10^{-4}	107×10^{20}
600	5.8×10^{-4}	67×10^{20}
800	2.45×10^{-4}	255×10^{20}

N-type electrical conductivity in CdO is due to Cd-interstitials and oxygen vacancies. With gradual increase in temperature conductivity increases due to increase in number of available free electrons in conduction band. With increase in annealing temperature potential barrier also decreases. Hence charge density also increases as it was found in Hall Effect measurements.

4.2 Optical and magnetic properties of Mn doped CdO nanoparticles

Transition metal Mn doping into CdO nanoparticles is especially interesting as doping of CdO gives rise to the variation in the energy band gap, carrier concentration and defects which in turn gives rise to changes in optical and magnetic properties. Main motivation of this work is to study optical and magnetic properties of Mn doped CdO nanostructures. Pristine and Mn doped CdO nanoparticles are synthesized by sol-gel method as explained in section 2.2.2 of chapter II. HR-TEM images of Mn doped CdO nanoparticles are shown in Figure 2.7 (A) of Chapter II where particle agglomeration was seen. This is

because surfactants are not used for preparing CdO nanoparticles. EDX (Figure 2.7 (C)) confirms the presence of Mn, cadmium and oxygen. Selected area electron diffraction (SAED, Figure 2.7 (B)), was also taken to confirm crystalline nature.

4.2.1 X-Ray diffraction Studies

XRD pattern for pristine and doped CdO nanoparticles are shown in the Figure 4.11. Williamson-Hall for calculation of crystallite size and strain generated in the nanoparticles is shown in Figure 4.12 (A, B, C and D). Lattice parameter of CdO samples are calculated by using the Nelson–Riley Parameter given in section 4.1.3. By extrapolating the lines to $NRF=0$, the true lattice parameter is obtained as shown in Figure 4.13 (A, B, C, D). Comparison between crystallite size, strain, interplanar distance and lattice constant of the nanoparticles are shown in TABLE 4.5.

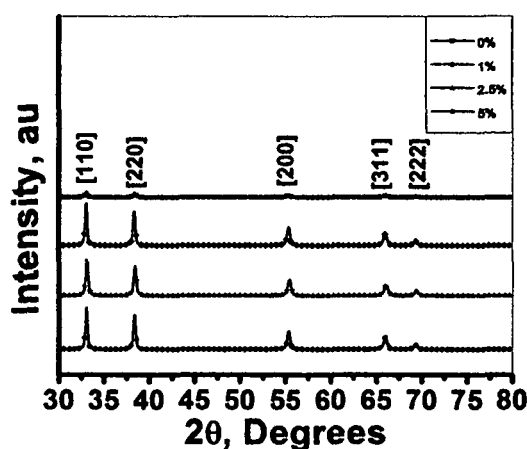


Figure 4.11: Comparison of XRD studies

Chapter IV

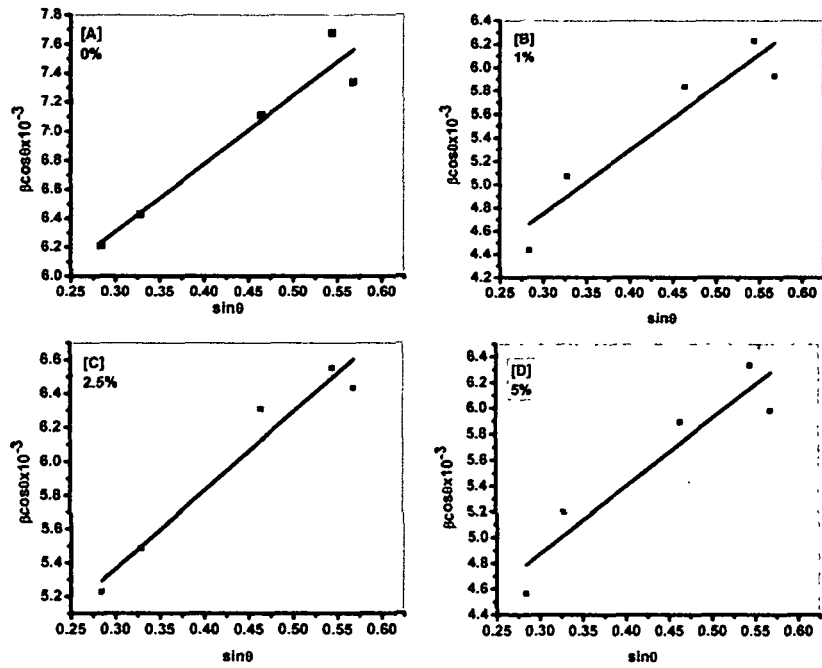


Figure 4.12: Williamson-Hall plot of pristine and Mn doped CdO nanoparticles

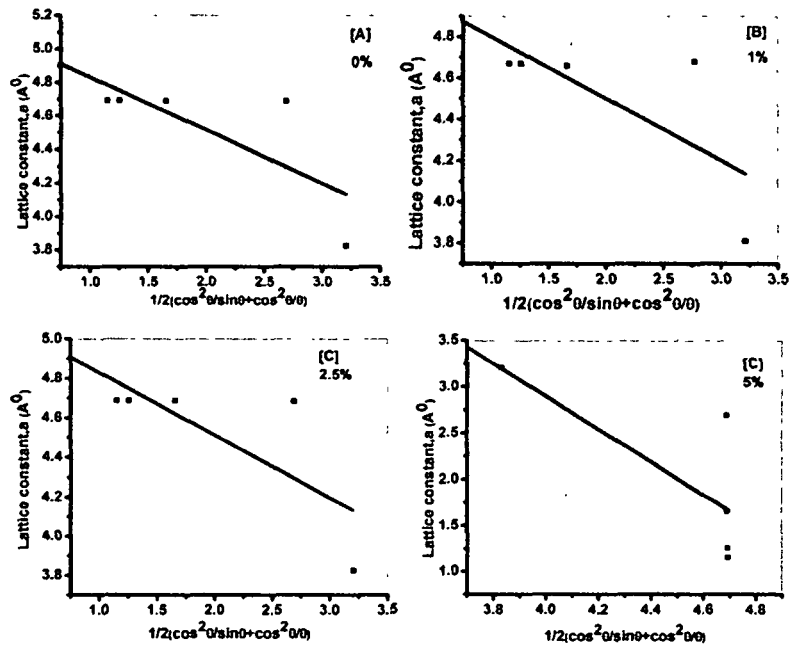


Figure 4.13: Nelson-Riley plot of pristine and Mn doped CdO nanoparticles

TABLE 4.5: Comparison of crystallite size, strain, interplanar distance and lattice constant

Sample Name	Crystallite size, nm	Strain $\times 10^{-3}$	Interplanar distance, nm	Lattice constant Å
0 %	5	4.68	0.34	4.8
1 %	5	5.44	0.19	4.8
2.5 %	4	4.61	0.18	4.9
5 %	4	5.23	0.19	3.4

Crystallite size of the nanoparticles does not change much with doping. Strain in the nanoparticles is highest for 1 % doping. Interplanar distance decreases than that for pristine nanoparticles. Crystallite size is almost constant for all the doping concentrations and so also lattice constants as calculated from Nelson-Riley plot.

4.2.2 Diffuse reflectance and photoluminescence spectroscopy of pristine and Mn doped CdO nanoparticles

Tauc's plots are drawn in a similar fashion as explained in section 4.1. Figure 4.14 shows comparison of diffuse reflectance spectra of the samples. Figure 4.15 (A, B, C and D) are Tauc's plots for direct band gap of pristine and doped CdO nanoparticles. Since Mn^{2+} has no spin allowed ligand field transitions, only the transitions for CdO were observed in the F(R) versus energy curves for all the doping concentrations.

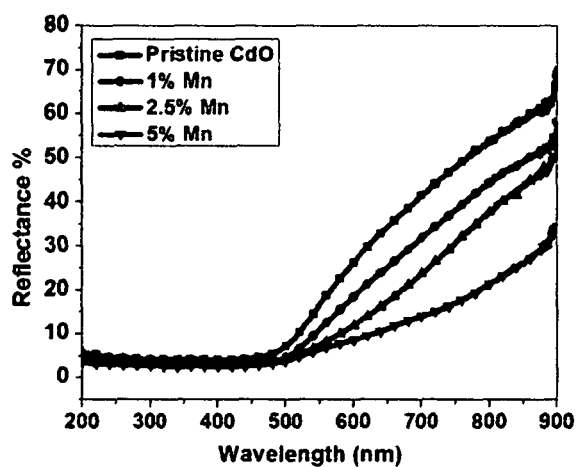


Figure 4.14: Diffuse reflectance spectra of pristine and Mn doped CdO nanoparticles

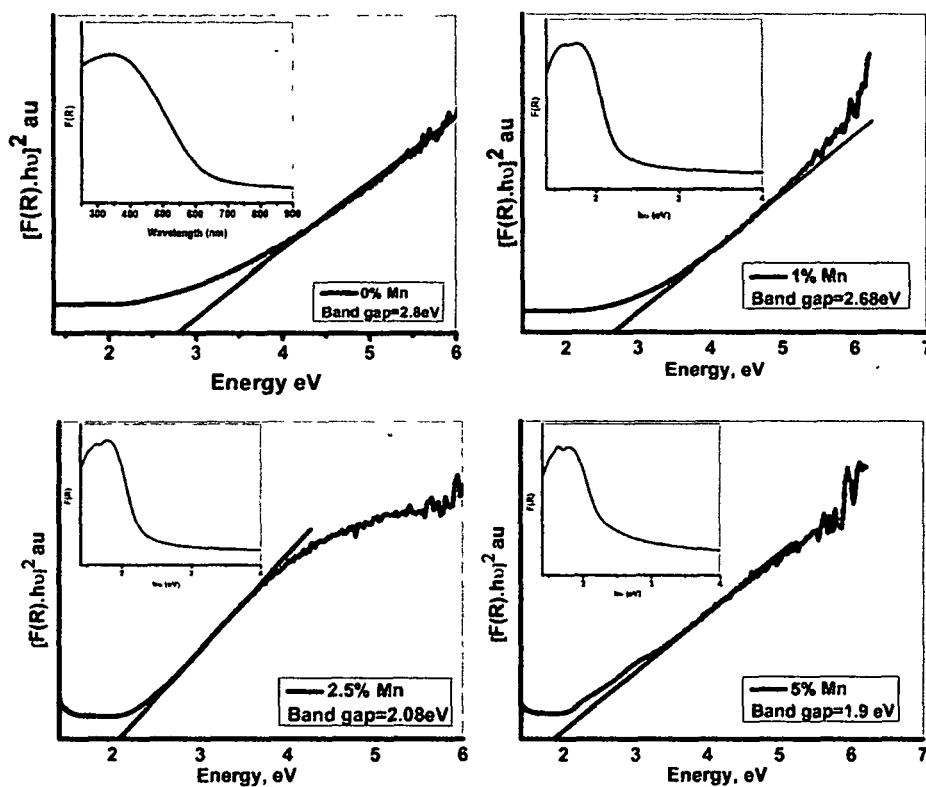


Figure 4.15: Tauc's plot for pristine and Mn doped CdO nanoparticles

Band gaps of the pristine and doped CdO nanoparticles calculated by Tauc's plot show that it decreases with increase in doping concentration. Instead of ideal direct band-edge

Chapter IV

absorption, an exponential tail in the absorption spectra was found which is called Urbach tail as explained in section 4.1. Defect states are formed as an intermediate state in the band gap of CdO. These defect states create a tail extending from the lower of conduction band to band gap. These states are very near to the valence band and spread the valence band edge deep inside the gap. Therefore, on both sides of the valence band maximum and conduction band minimum, an energy tail is formed. This defect tail is known as the Urbach tail [11]. The energy associated with this defect tail is referred to as Urbach energy. Dopant impurities as well as other structural imperfections for example defects such as oxygen vacancy, interstitial vacancy etc introduce lattice disorder. So, Urbach energy is used to characterize the degree of disorder in the nanoparticles. Urbach energy was calculated using the relation given in section 4.1.1. Figure 4.16 (A, B, C and D) is the Urbach energy plot for the samples. Calculated values of Urbach energy and band gaps are summarized in table 4.16.

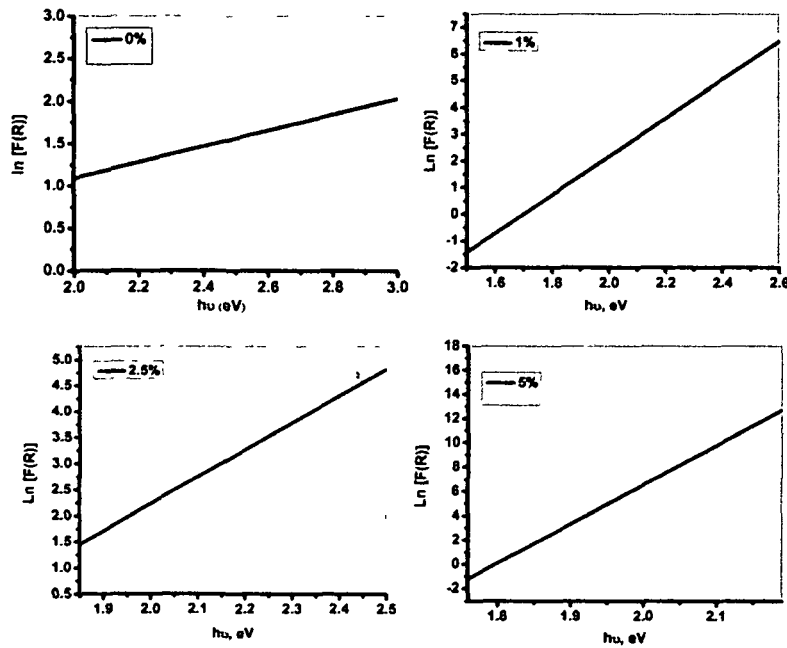


Figure 4.16: Urbach energy plot for pristine and Mn doped CdO nanoparticles

TABLE 4.6: Table for Bandgap and Urbach energy of pristine and Mn doped CdO nanoparticles

Sample Name	Band gap eV	Urbach Energy eV
0 %	2.8	0.10
1 %	2.68	0.13
2.5 %	2.08	0.19
5 %	1.9	0.03

Band gap of the nanoparticles decreases with increase in doping concentration. Decrease in band gap is may be due to trapping of Mn atoms at the grain boundary which leads to the introduction of Mn defect states within the forbidden gap. With increase in Mn concentration density of these Mn induced defect states increases, leading to the observed decrease of band gap. Urbach energy which is a measure of disorderness in the nanoparticles is higher for 1 % and 2.5 % Mn doped CdO nanoparticles than 0 %. But for 5 % Mn doped samples Urbach energy decreases than 0 % doping.

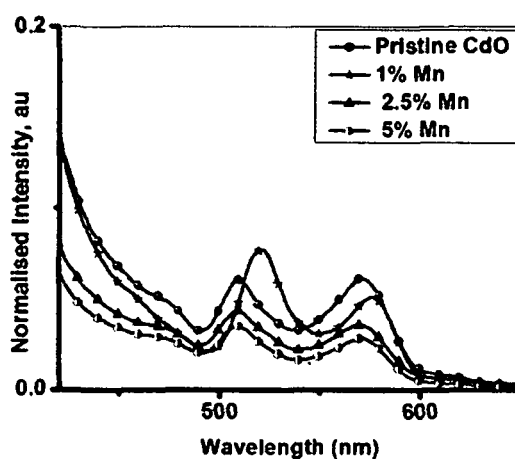


Figure 4.17: Normalized PL spectra of pristine and Mn doped CdO nanoparticles

Normalized PL spectra of pristine and Mn doped CdO nanoparticles are shown in Figure 4.17. It is seen that PL intensity decreases with increase in doping concentration. This

partial quenching in PL intensity may be due to various nonradiative processes like Auger recombination. Strong carrier to carrier interactions lead to Auger nonradiative process. Rather than releasing the energy of recombination as a photon or phonon, the excess energy is transferred to another electron known as Auger electron. The Auger electron loses its surplus energy by creation of phonon. The Auger recombination process involves two electrons and a hole in the conduction band and valence band, respectively. For 1 % doping intensity is higher than that for pristine CdO. This can happen only if the dopants are properly incorporated in the host lattice. PL spectra have both blue and green emissions which are results of emissions from interstitial vacancies and oxygen vacancies. And green emitting peak is actually composed of two peaks due to two different types of oxygen vacancies [12].

4.2.3 Electron paramagnetic resonance spectroscopy (EPR)

EPR is used at the microscopic level to get information about the oxidation state, lattice defects, color centres, site occupancy and magnetic phases in the host semiconductor lattice. This technique is based on the microwave absorption of unpaired electron spins in presence of an external magnetic field. EPR studies of powder of CdO nanoparticles formed at high temperature provide information about the conduction electrons, together with Cd^+ ions. Bulk CdO is a general non-stoichiometric n-type semiconductor. When it is in nano size range its properties change from Bulk. Non-stoichiometric CdO nanoparticles show asymmetric EPR signal. On the basis of other already reported results, signals with $g = 2.046686$ and $g = 2.202907$ were assigned to conduction band electrons, and to Cd^+ ions on the site of Cd^{2+} in pristine CdO nanoparticles [13-15]. Cd^+ ions arise from polaronic self-trapping of electrons introduced by oxygen deficiency at Cd sites to generate localized $5s^1$ states. In ionic solids, single electrons can produce localized lattice distortions, resulting from their electrostatic interaction with neighboring ions. This type of distortion accompanies the electron as it moves through the lattice, and the result is known as polaron.

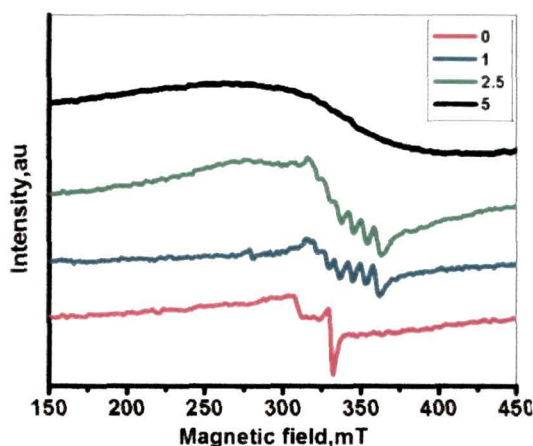


Figure 4.18: EPR spectra of pristine and Mn doped CdO nanoparticles

EPR spectra of pristine and Mn doped CdO nanoparticles are shown in Figure 4.18. The electronic configuration of Mn^{2+} is $3d^5$ and electronic ground state is ${}^6S_{5/2}$ as the spin of Mn^{2+} is $S=5/2$. The energy level of electrons under an external field is again split into six lines by magnetic field produced by the nuclear spin states giving sextet of hyperfine line [16]. As the concentration of Mn^{2+} increases from 1 % to 5 %, sextet of hyperfine lines disappears and the peak broadens. Dipolar interaction between Mn^{2+} - Mn^{2+} is responsible for this EPR broadening effect [17]. No Cd^+ related EPR signal is seen here as sextet of hyperfine lines overlaps the EPR signal due to Cd^+ ions.

4.2.4 Origin of room temperature ferromagnetism

Magnetic hysteresis loops for the samples with three levels of Mn doping from SQUID measurements are shown in Figure 4.19. The magnetization versus magnetic field loops at room temperature exhibit coercive field and saturation magnetization of approximately 255, 252, 230 Oe and 0.22, 0.13, 0.12 emu/gm respectively. It is seen that coercivity decreases with increase in doping but saturation magnetization increases with doping.

Nevertheless, saturation magnetization per impurity ion decreases with increase in doping concentration.

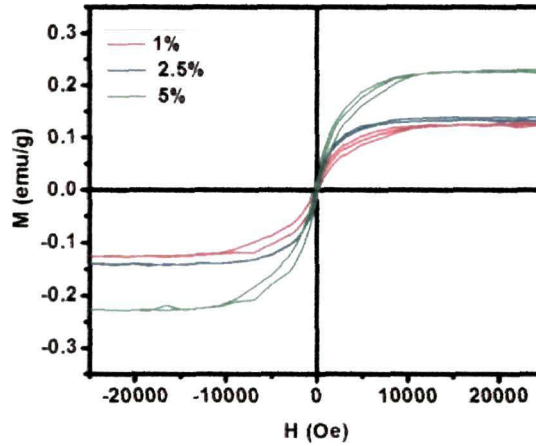


Figure 4.19: Magnetization curve of pristine and Mn doped CdO nanoparticles

The exact mechanism of intrinsic ferromagnetism in transition metal (TM) -doped oxides is still under debate. A diversity of theories has been proposed, such as super-exchange, double-exchange between the d states of TMs, free-carrier-mediated exchange and sp-d exchange mechanism, Rudermann- Kittel-Kasuya-Yosida (RKKY) etc. RKKY interaction is based on free electrons but CdO do not have free electrons like metals at such low doping. This is only suggestive; other possible mechanisms are also there that can explain the magnetic origin. Since any Cd^+ centre related peaks are not seen in EPR spectra, so formation of bound magnetic polaron (BMP) by Cd^+ ions with singly charged oxygen vacancy is not perfectly justified. So, here indirect interaction among Mn^{2+} (Mn-O-Mn) centres may lead to ferromagnetism, whereas direct interaction among them leads to antiferromagnetism. But with such diluted amount of Mn direct or indirect interaction is not possible. With increase in Mn doping, the average distance between Mn^{2+} ions decreases, resulting in enhancement of antiferromagnetic contribution [18-20]. It is well known that Mn ions belonging to antiferromagnetic clusters do not contribute to the increase in magnetic signal rather they reduce the net magnetization. Among all oxides of Mn, only MnO is anti-ferromagnetic with a Neel temperature of 96 K and Mn_3O_4 is ferromagnetic with a curie temperature of 43 K. But T_c is very low, so entire

ferromagnetism cannot be due to Mn_3O_4 . Also in our case, nano-clustering or MnO formation is ruled out as any impurity phase regarding Mn clustering was not observed in our XRD spectra. The formation of another type of BMP, in which an electron trapped in an oxygen vacancy (F center) couple with the magnetic spins of the nearest Mn^{2+} ions within the radius of the hydrogen like orbit of the F center and forms a BMP, may lead to ferromagnetism. Electron locally trapped by oxygen vacancy, with the trapped electron occupying an orbital overlapping with the d shells of TM (Mn^{2+}) neighbors, has been proposed to explain the origin of ferromagnetism [21-24] in Mn doped CdO nanoparticles. The radius of the hydrogenic orbit of the F^+ -center is given by $r_H = \epsilon_r(m/m^*)a_0$ where ϵ_r is the dielectric constant, m is the electron mass, a_0 is the Bohr radius. Those Mn^{2+} ions that fall within this F-center radius interacts with the spin of F center, forms BMP and imparts ferromagnetism. These oxygen vacancies with single electron are called F^+ centre. PL spectra also confirm presence of two types of oxygen vacancies. Since electrons in doubly occupied oxygen vacancy (F centre) for $1S^2$ state generate only weak antiferromagnetic interaction, so BMP with singly charged oxygen vacancies are responsible for room temperature ferromagnetism (RTFM).

4.3 Conclusion

Following are the novel findings of our work in brief:

1. Cadmium interstitials which are Frenkel defects after getting higher energy go to the surface. At the surface after getting further higher energy these interstitial defects become oxidized and for this reason blue PL intensity which is due to Cd-interstitials first increases and then decreases.
2. Number of oxygen vacancies continuously increase with rise in temperature, so green PL intensity which is due to oxygen vacancies increases with rise in temperature.
3. Also, since F^+ centres are present in the samples so with rise in temperature, electrons trapped in oxygen vacancies get sufficient energy and become free

Chapter IV

electrons. Hence conductivity and charge density increases with increase in temperature.

4. It was found that the incorporation of Mn in the host CdO nanoparticles leads to decrease in band gap. Also there is a partial quenching of luminescence intensity because of doping. Absence of any secondary oxide phases of Mn is confirmed. The origin of room temperature ferromagnetism can be assigned to formation of bound magnetic polaron.
-

References:

1. Kubelka, P. New Contributions to the Optics of Intensely Light-Scattering Materials. Part I, *J. Opt. Soc. Am.* **38** (5), 448--448, 1948.
2. Yang, L. & Kruse, B. Revised Kubelka–Munk theory. I. Theory and application, *J. Opt. Soc. Am. A* **21** (10), 1933--1041, 2004.
3. Yang, L. & Miklavcic, S. Revised Kubelka-Munk theory. III. A general theory of light propagation in scattering and absorptive media, *J. Opt. Soc. Am. A* **22** (9), 1866--1873, 2005.
4. Adachi, S. *Properties of Group-IV, III-V and II-VI Semiconductors*, John Wiley & Sons Ltd, West Sussex, England, 2005.
5. Zeng, H. et al. Blue Luminescence of ZnO Nanoparticles Based on Non-Equilibrium Processes: Defect Origins and Emission Controls, *Adv. Funct. Mater.* **20** (4), 561--572, 2010.
6. Charles, K. *Introduction to Solid state Physics* (7th ed.) Wiley India (P.) Limited, New Delhi, 2004.

Chapter IV

7. Nogi, K., Hosokawa, M., Naito, M. & Yokoyama, T. *Nanoparticle Technology Handbook* (2nd ed.) Kidlington, UK, 2012.
8. Nelson, J. B. & Riley, D.P. An experimental investigation of extrapolation methods in the derivation of accurate unit-cell dimensions of crystals, *Proc. Phys. Soc.* **57** (3), 160--177, 1945.
9. Jbaier D.S. Physical Properties of CdO Thin Films Prepared by Spray Pyrolysis Technique, *Eng. & Tech. Journal* **31** (2), 185--193, 2013.
10. Bhosale, C.H. et al. Structural, optical and electrical properties of chemically sprayed CdO thin films, *Mat. Sci. Eng. B* **122** (1), 67--71, 2005.
11. Boubaker, K. A physical explanation to the controversial Urbach tailing universality, *Eur. Phys. J. Plus* **126** (10), 10--14, 2011.
12. B. Goswami, A. Choudhury, Enhanced visible luminescence and modification in morphological properties of Cadmium Oxide nanoparticles induced by annealing, *Journal of Experimental Nanoscience*, accepted.
13. Rajkumar, N. et al. On the possibility of ferromagnetism in CdO: Mn at room temperature, *J. Exp. Nanosci.* **6** (4), 389--398, 2011.
14. Gulino, A. & Tabbi, G. CdO thin films: a study of their electronic structure by electron spins resonance spectroscopy, *Appl. Surf. Sci.* **245** (1-4), 322--327, 2005.
15. Shinde, R.F. & Date, S.K. X-band EPR studies of hyperfine and superhyperfine structure of Mn²⁺ ions in polycrystalline CdO, *Mater. Chem. Phys.* **24** (1-2), 71--81, 1989.
16. Iragashi, T. et al. Characterization of Mn²⁺ coordination of Mn²⁺ coordination states in ZnS nanocrystal by EPR spectroscopy and related photoluminescence properties, *J. Nanopart. Res.* **3** (1), 51--56, 2001.
17. Magana, D. *Synthesis and characterization of dilute magnetic semiconductors nanoparticles*, Ph. D. Thesis, Florida State University, USA, 2007.

Chapter IV

18. Hao, Y.M. et al. Structural, optical and magnetic studies of Mn-doped zinc oxide hierarchical microspheres by self-assembly of nanoparticles, *Nanoscale Res. Lett.* **7** (1), 101--109, 2012.
19. Choudhury, B. & Choudhury, A. Oxygen vacancy and dopant concentration dependent magnetic properties of Mn doped TiO₂ nanoparticle, *Curr. Appl. Phys.* **13** (6), 1025--1031, 2013.
20. Ilyas, U. et al. Enhanced indirect ferromagnetic p-d exchange coupling of Mn in oxygen rich ZnO: Mn nanoparticles synthesized by wet chemical method, *J. Appl. Phys.* **111** (3), 033503--, 2012.
21. Coey, J.M. et al. Donor impurity band exchange in dilute ferromagnetic oxides, *Nat. Mater.* **4**, 173--179, 2005.
22. Coey, J.M.D. et al. Ferromagnetism in Fe-doped SnO₂ films, *Appl. Phys. Lett.* **84** (8), 1332--1334, 2004.
23. Caldero'n, M.J. & Sarma, S.D. Theory of carrier mediated ferromagnetism in dilute magnetic oxides, *Ann. Phys.* **322** (11), 2618--2634, 2007.
24. Iqbal, J. et al. Oxygen-vacancy-induced green emission and room-temperature ferromagnetism in Ni-doped ZnO nanorods, *New J. Phys.* **11**, 063009-063023, 2009.

**Chapter V: Enhanced luminescence and realization of
ferromagnetism in Vacuum annealed CdO
nanoparticles**

Rocksalt CdO nanoparticles show remarkable magnetic properties when these particles are annealed in vacuum conditions. These nanoparticles show both blue and green luminescence. Vacuum annealed CdO nanoparticles show enhanced luminescence properties and room temperature ferromagnetism than air annealed nanoparticles. Here, Cd-interstitials and Oxygen vacancies play significant role. Increase in oxygen vacancies lead to increase in strain in nanoparticles. To relax and to decrease strain, crystallite size in CdO nanoparticles increase. The observed ferromagnetism is explained with bound magnetic polaron model.

5.1 Structural and Morphological Properties of CdO Nanoparticles

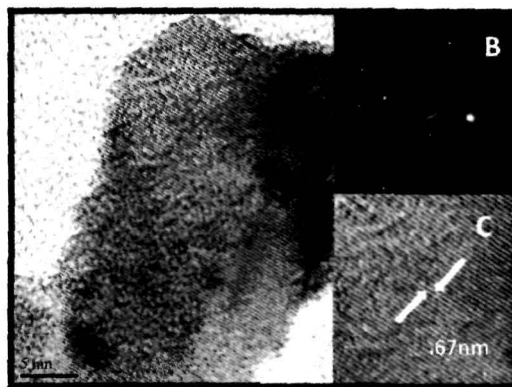


Figure 5.1: (A) HR-TEM of CdO nanoparticle, (B) SAED of CdO nanoparticle, (C) Lattice plane spacing of CdO nanoparticles

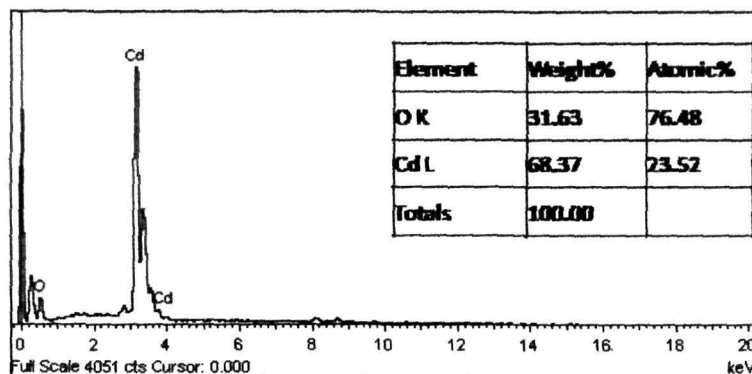


Figure 5.2: EDX spectrum of CdO nanoparticles

High-resolution transmission electron microscope (HR-TEM) images are shown in Figure 5.1. From a carefully calibrated high resolution image, an individual particle is selected with its zone axis parallel to the beam. Size of a single CdO nanoparticle annealed in air is around 25 nm as shown in high resolution image shown in Figure 5.1 (A). Crystal planes were clearly seen in HR-TEM (A & C). Selective area electron diffraction (SAED, Figure 5.1 (B)) was also taken to confirm polycrystalline nature. Interplanar spacing is 0.67 nm as shown in Figure 5.1 (C). Presence of cadmium and oxygen are confirmed by energy dispersive X-ray spectra (EDX) taken by JEOL, JSM-6390LV, INCAx-sight EDX detector as shown in Figure 5.2. Weight percentage of oxygen present is 31.63 and cadmium is 68.37.

Morphological properties of CdO nanoparticles were studied by XRD. XRD studies of both air and vacuum annealed CdO nanoparticles samples have been done to find the crystal structure as shown in Figure 5.3.

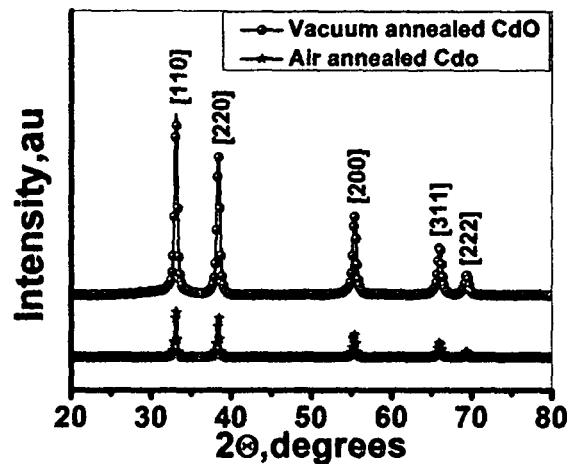


Figure 5.3: XRD spectra of CdO nanoparticles

From $\beta \cos\theta$ versus $\sin\theta$ graph as shown in Figure 5.4 (A & B), a straight line is obtained with slope η [1]. Slope gives strain generated in the nanoparticles. Crystallite size (D) can be calculated from this method. Lattice parameter of CdO samples are calculated by using the Nelson–Riley Parameter as described before in chapter IV [2]. By extrapolating the lines to $\text{NRF}=0$, the true lattice parameter is obtained as shown in Figure 5.4 (C & D).

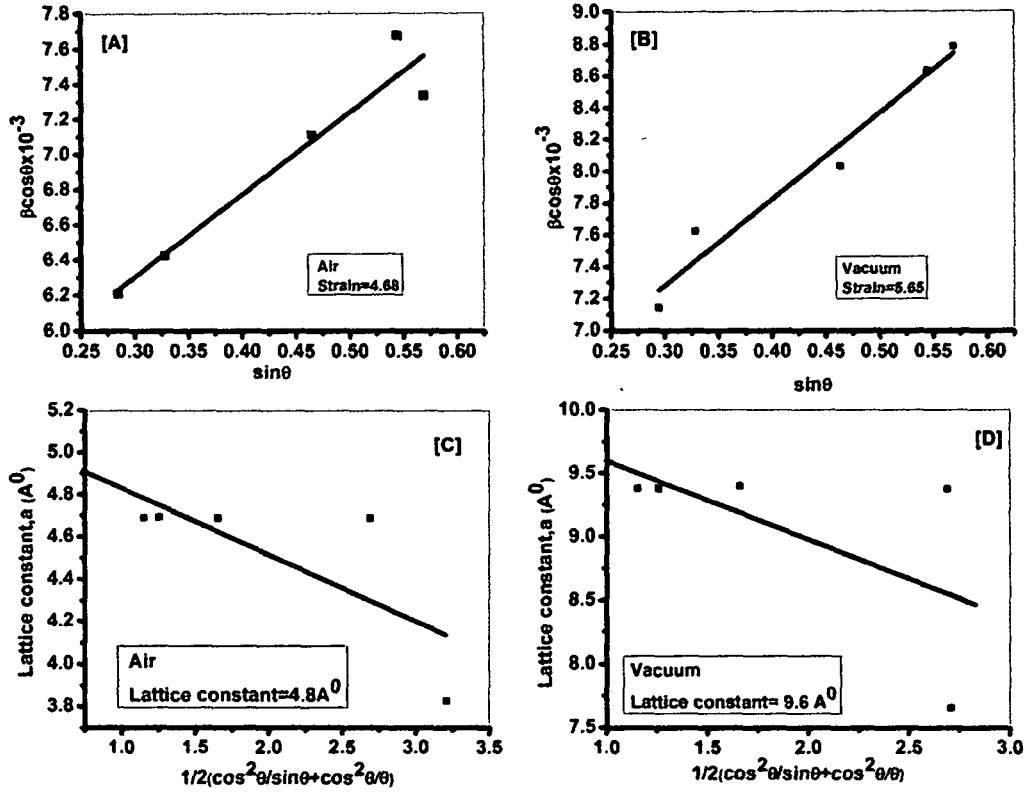


Figure 5.4: (A) & (B) W-H plot and (C) & (D) NRF plot of air and vacuum annealed samples

TABLE 5.1: Comparison of crystallite size, strain, interplanar spacing and lattice constant of the CdO nanoparticles

Sample name	Crystallite size nm	Strain $\times 10^{-3}$	Interplanar spacing nm	Lattice constant Å
Air annealed CdO	24	4.68	0.34	4.8
Vacuum annealed CdO	27	5.65	0.67	9.6

Comparison between crystallite size, strain, interplanar distance and lattice constant of the nanoparticles are shown in table 5.1. Crystallite size, strain, interplanar spacing and lattice constant increased when particles are annealed in vacuum as annealing in vacuum leads to increase in number of oxygen vacancies due to lack of oxygen in air. With increase in oxygen vacancies surrounding a cadmium atom, strain experienced by the cadmium atom will increase. To decrease the strain experienced, these cadmium atoms will try to push the defects away from their positions and thereby, increasing the crystallite size. Or, in other words, formation of oxygen vacancies leads to displacement of the nearest-neighbor atoms of oxygen vacancy from their ideal position. In CdO, cadmium atoms near the oxygen vacancy will relax by going away from the oxygen vacancy. Lattice parameter and interplanar spacing of the nanoparticles also increase with increase in crystallite size. The increase of lattice parameter can also be associated with the displacement of the nearest-neighbor atoms of oxygen vacancy. So the lattice constant will increase with the increase of the density of oxygen vacancies and so also interplanar distance.

5.2 Study of diffuse reflectance spectra and PL spectra

Diffuse reflectance spectra (DRS) of the nanoparticles were shown in Figure 5.5 [3-5]. And Figures 5.6 (A), (B) & (C), (D) are Tauc's plots for calculation of direct and indirect band gaps of air and vacuum annealed CdO nanoparticles.

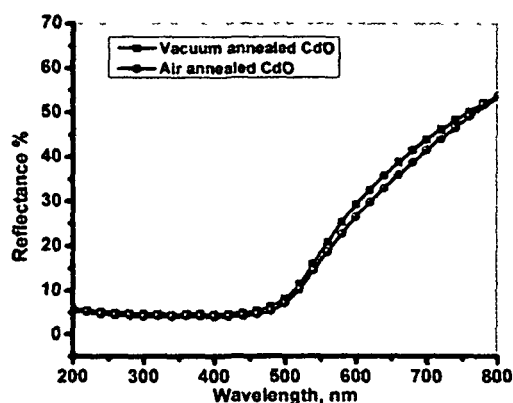


Figure 5.5: Comparison of DRS of CdO nanoparticles annealed in air and vacuum

Defect states introduced by dopant impurities as well as other structural imperfections for example defects such as oxygen vacancy, interstitials etc formed as an intermediate state in the band gap of CdO, creating a band tail. These defects reside inside the band gap. Therefore, on both sides of the valence band maximum and conduction band minimum, an energy tail is formed. This defect tail is known as the Urbach tail [6]. The energy associated with this defect tail is referred to as Urbach energy. It is used to characterize the degree of disorder in the crystal [7]. Figure 5.7 (A) and (B) is the Urbach energy plot for the samples. Calculated values of Urbach energy and band gaps are summarized in table 5.2.

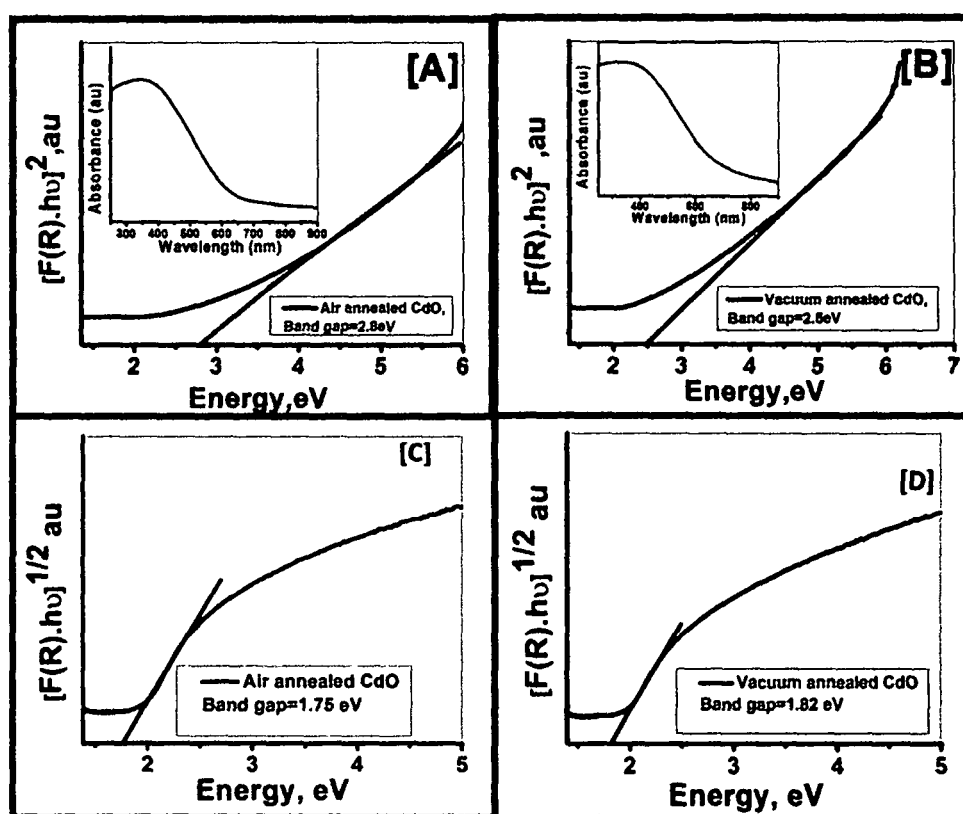


Figure 5.6: Tauc's plot for calculation of direct band gap of (A) air annealed and (B) vacuum annealed CdO nanoparticles, & indirect band gap of (C) air annealed, (D) vacuum annealed CdO nanoparticles

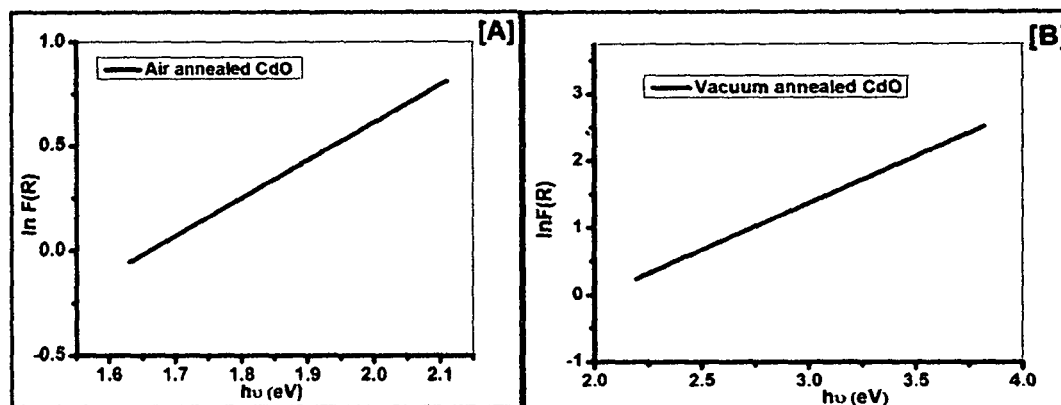


Figure 5.7: Urbach energy plot for (A) Air annealed CdO and (B) Vacuum annealed CdO nanoparticles

TABLE 5.2: Urbach energy and Band gap of CdO nanoparticles

Sample name	Urbach energy, eV	Direct band gap, eV	Indirect band gap
Air annealed CdO	0.5541	2.8	1.75
Vacuum annealed CdO	0.7153	2.5	1.82

Direct band gap is decreased from 2.8 eV to 2.5 eV and indirect band gap slightly increased from 1.75 eV to 1.82 eV when the particles are annealed in vacuum. Also Urbach energy increased from 0.5541 eV to 0.7153 eV. Increase in indirect band gap and Urbach energy are due to the increase in defects in the crystal. As CdO contains both Cd-interstitials and oxygen vacancies and with vacuum annealing samples will face lack of oxygen while growing. So number of oxygen vacancies increases and this must be the reason for band gap narrowing.

PL spectra of CdO nanoparticles annealed in air and vacuum are shown in Figure 8. Blue luminescence in CdO nanostructures is due to Cd-interstitial vacancies and green

luminescence is due to oxygen vacancies [8]. Oxygen vacancies play an important role in CdO nanostructures as explained earlier. These defects are responsible for band gap narrowing and increase in crystallite size. In case of vacuum annealed particles, number of oxygen vacancies will increase as these particles face lack of oxygen in environment. It has been found by theoretical calculations in Indium Oxide that formation energy of oxygen vacancy is very low. This leads to nonstoichiometry. And sufficient concentrations of oxygen vacancies can contribute to lattice expansion [9]. Here with increase in oxygen vacancies intensity of green peak increases. As shown in Figure 5.8, green peak actually consists of two peaks which may be due to different oxygen vacancy levels for example F^{2+} centre, F^+ centre etc. Luminescence intensity of blue peak decreased and green peak increased when the particles are annealed in vacuum. Increase in green peak intensity confirms that more oxygen vacancies are created now.

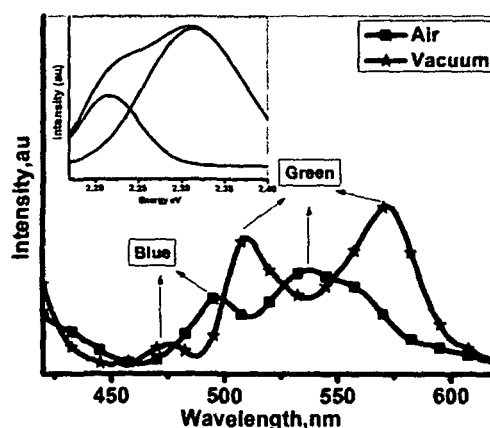


Figure 5.8: PL spectra of air and vacuum annealed CdO nanoparticles

Raman scattering is a multifaceted investigation technique for characterization of semiconductor materials and structures. Rocksalt compounds like CdO has O_h space group symmetry with only one optically active mode (IR-active Flu mode). However, Raman spectroscopy cannot detect this mode because of high amount of conducting electrons present in CdO. Moreover, the first-order Raman modes are forbidden [10,11]. Early reports suggest that the zone-center transverse-optical and longitudinal optical phonon modes of CdO are located at 262 cm^{-1} and 523 cm^{-1} , respectively [12]. Later,

Schaack and Uhle have done a Raman study of polycrystalline CdO samples with different free electron densities. As for CdO, no phonon dispersion curves were available, in that work second-order features were assigned by comparison to the Raman spectra of several alkaline-earth oxides [13]. Vibrational properties of CdO have not been investigated well.

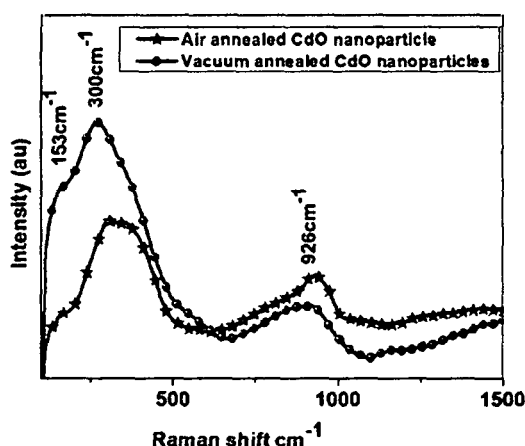


Figure 5.9: Raman spectra of CdO nanoparticles annealed in air and vacuum

Raman spectra of CdO nanoparticles are dominated by a relatively broad peak located at 300 cm^{-1} and a less intense peak at 926 cm^{-1} as shown in Figure 5.9. Peak at 300 cm^{-1} is actually composed of two peaks. There is another peak at 153 cm^{-1} . In principle, according to selection rules for the rocksalt structure both TO and LO modes are dipole forbidden, all features in the spectrum can be attributed to second-order Raman scattering processes in CdO. Second order Raman peaks observed are due to overtones and combination modes. Strong Raman signal of the second-order modes are due to low absorption coefficient of CdO for the visible excitation wavelengths. There is a shift of Raman peak for samples than the bulk samples. Also, CdO nanoparticles annealed in vacuum show red shifts. Although these particles do not show any oxygen vacancy related new peak but due to strain generated with increase in oxygen defects in the system the peak shifts to lower frequency (red shift). Oxygen vacancies produced in the particles might decrease the average atomic mass and cause mass fluctuations at the

oxygen positions. This results in red shift of Raman peak of vacuum annealed nanoparticles [11].

5.3 Electron Paramagnetic resonance study

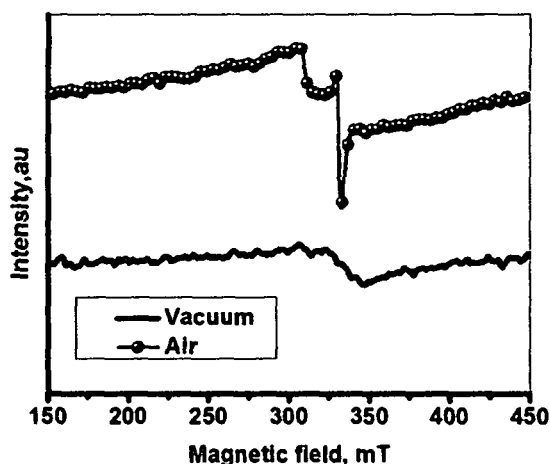


Figure 5.10: EPR spectra of Mn doped CdO nanoparticles

Electron paramagnetic resonance spectroscopy (shown in Figure 5.10) is used at the microscopic level to get information about the oxidation state, lattice defects, color centres, site occupancy and magnetic phases in the host semiconductor lattice as explained in section 2.5 of chapter II. In presence of an external magnetic field of unpaired electron spins absorb microwave radiation [12]. The paramagnetic center is a Cd^+ ion ($2S_{1/2}$ ground state) on the site of a Cd^{2+} ion. The unpaired electron is localized not only at the central Cd^+ ion, but reaches far into the crystal [13]. Therefore, on the basis of other already reported results, signals with $g = 2.046686$ and $g = 2.202907$ were assigned to conduction band electrons, and to Cd^+ ions on the site of Cd^{2+} . Cd^+ ions arise from polaronic self-trapping of electrons introduced by oxygen deficiency at Cd sites to generate localized $5s^1$ states [14-18]. Already reported results show that Cd^+ states were not involved in the conduction band. The presence of nuclear moments in cadmium isotopes can contribute local magnetic fields at the electron in addition to the main

applied field. Since the possible orientations of a nuclear moment are $2I + 1$, where I is the nuclear spin quantum number, the absorption spectrum for the electron will consist of $2I + 1$ lines. So, ^{111}Cd and ^{113}Cd should give rise to hyperfine lines. But the other peak due to conduction electrons disappears at liquid Helium temperature. Single electrons can produce localized lattice distortions in ionic solids because of their electrostatic interaction with neighboring ions. As the electron moves through the lattice, this lattice distortion moves with the electron. This results in what is known as polaron. When the distortion is sufficiently strong, the electron may be trapped at a particular lattice site. EPR peaks observed in present experiments are due to localized $\text{Cd } 5s^1$ states. EPR signal of vacuum annealed sample broadened significantly than the air annealed sample. This may be attributed to the increase in Cd^+ concentration which is again depends upon number of oxygen vacancies. Increase in oxygen vacancies due to vacuum annealing leads to more electron transfer from Cd^{2+} to oxygen vacancy site and hence more number of Cd^+ are generated.

5.4 Study of Magnetic properties

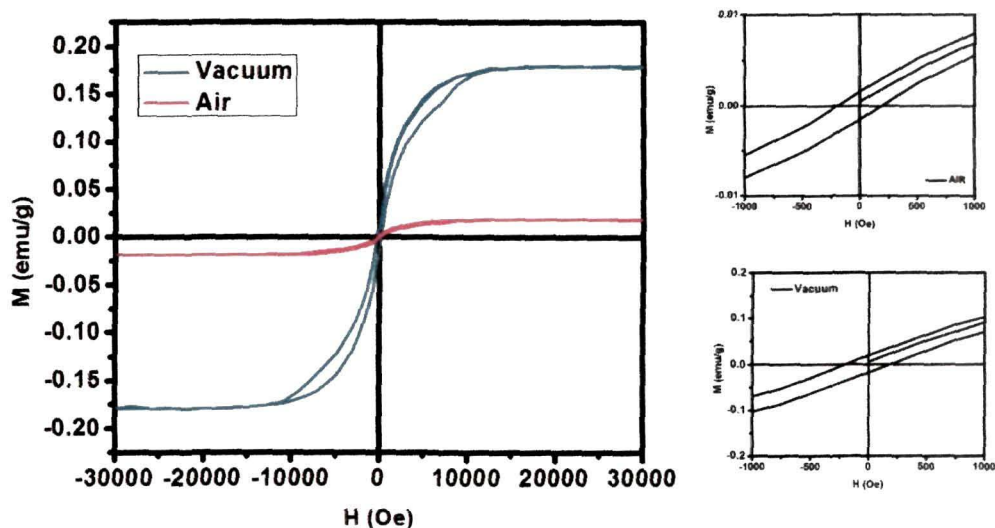
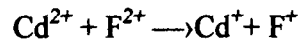


Figure 5.11: Comparison of M-H curves of CdO nanoparticle annealed in air and vacuum

The field dependent magnetic measurements are shown in Figure 5.11. The samples show hysteresis loop at room temperature. Magnetic moment is quite higher for vacuum annealed sample. Due to nonstoichiometric structure of CdO nanoparticles, defects such as oxygen defects, Cd⁺ and Cd interstitials are present. Among these defects oxygen vacancies play an important role in determination of magnetic properties of CdO nanoparticles. As explained earlier in EPR spectroscopy measurements, Cd²⁺ ions give rise to Cd⁺ ions by sharing one electron given by oxygen vacancy (F²⁺) present nearby the Cd²⁺ ion. Formation of Cd⁺ centres in CdO is shown below:



The interaction between F²⁺ center and Cd²⁺ gives rise to long range ferromagnetic ordering. From PL spectra, it can be observed that these F⁺/F²⁺ centres form defect levels within band gap giving green PL emission. Remnant field of vacuum and air annealed samples are found to be 0.0016 emu/g, 0.02 emu/g and coercivity of vacuum and air annealed samples are found to be 167 Oe, 175 Oe. If Cd interstitials would have been the reason for ferromagnetism then it would have been decreased after vacuum annealing. However, vacuum annealed sample showed good luminescence properties and enhanced ferromagnetism. So F⁺ centres must be the reason for ferromagnetism. Thus the formation of bound magnetic polaron (BMP) which includes electrons locally trapped by oxygen vacancies with the trapped electron in F⁺ centre occupying an orbital overlapping with the unpaired electron in Cd⁺ is proposed to explain the observed ferromagnetism in CdO nanoparticles. Electrons in doubly occupied oxygen vacancy (F²⁺ centre) for 1S² state generate only weak antiferromagnetic interaction. Oxygen vacancy constituted BMP is one of the most promising models to explain the room temperature ferromagnetism (RTFM). Within the BMP model, greater density of oxygen vacancies helps to produce more BMPs and enhancing RTFM behavior [19-22]. The hydrogenic orbit of the F⁺ centre is given by $a_{\beta} = \epsilon (m/m^*)$, with 'ε' is the static dielectric constant, 'm*' is the effective mass of the polaron, 'a_β' is the Bohr radius and m is the effective mass of electron. Those Cd⁺ ions which fall within this radius interact with the spin of F⁺ centre and forms BMP [23-25]. Other models like Rudermann-Kittel-Kasuya-Yoshida (RKKY) interaction is based on free electrons. But CdO nanoparticles do not have free electrons

like metals. Direct interactions like double exchange or superexchange mechanism are not valid as there are no magnetic cations in CdO nanoparticle samples [27-29].

5.5 Conclusion

Following novel findings are found in the work:

1. CdO nanoparticles show different optical and magnetic properties than air annealed nanoparticles. With vacuum annealing number of oxygen vacancies in the system increase which bring changes in crystallite size, strain, interplanar spacing and lattice constant.
2. Oxygen vacancies are also responsible for increase in green luminescence intensity in vacuum annealed nanoparticles.
3. Oxygen vacancies cause red shift of Raman peak of vacuum annealed nanoparticles. Oxygen vacancies generated in the particles might decrease the average atomic mass and cause mass fluctuations at the oxygen positions. This results in red shift.
4. From the broad EPR peak in vacuum annealed nanoparticles, one can conclude increase in number of oxygen vacancies in the system. Ferromagnetism in nanoparticles can be explained with BMP model. Increase in number of BMPs in the system lead to ferromagnetism.

References:

1. Nogi, K., Hosokawa, M., Naito, M. & Yokoyama, T. *Nanoparticle Technology Handbook* (2nd ed.), Kidlington, UK, 2012.
2. Nelson, J. B. & Riley, D.P. An experimental investigation of extrapolation methods in the derivation of accurate unit-cell dimensions of crystals, *Proc. Phys. Soc.* **57** (3), 160--177, 1945.
3. Kubelka, P. New Contributions to the Optics of Intensely Light-Scattering Materials. Part I, *J. Opt. Soc. Am.* **38** (5), 448--448, 1948.

4. Yang, L. & Kruse, B. Revised Kubelka–Munk theory. I. Theory and application, *J. Opt. Soc. Am. A* **21** (10), 1933--1041, 2004.
5. Yang, L. & Miklavcic, S. Revised Kubelka-Munk theory. III. A general theory of light propagation in scattering and absorptive media, *J. Opt. Soc. Am. A* **22** (9), 1866--1873, 2005.
6. Boubaker, K. A physical explanation to the controversial Urbach tailing universality, *Eur. Phys. J. Plus* **126** (10), 10--14, 2011.
7. S. Adachi, *Properties of Group-IV, III-V and II-VI Semiconductors*, West Sussex: England, 2005.
8. B. Goswami, A. Choudhury, Enhanced visible luminescence and modification in morphological properties of cadmium oxide nanoparticles induced by annealing, *Journal of Experimental Nanoscience*, accepted.
9. Walsh, A. et al. Strontium migration assisted by oxygen vacancies in SrTiO₃ from classical and quantum mechanical simulation, *Phys.Rev. B* **83** (22), 224105-9, 2011.
10. Lany, S. & Zunger, A. Dopability, intrinsic conductivity, and nonstoichiometry of transparent conducting oxides, *Phy. Rev. Lett.* **98** (4), 045501--4, 2007.
11. Migani, A. et al. Dramatic reduction of the oxygen vacancy formation energy in ceria particles: a possible key to their remarkable reactivity at the nanoscale, *J. Mater. Chem.* **20** (46), 10535--10546, 2010.
12. Cuscó, R. et al. Raman scattering of cadmium oxide epitaxial layers grown by metal-organic vapor phase epitaxy, *J. Appl. Phys.* **107** (6), 063519--4, 2010.
13. Finkenrath, H. et al. The influence of phonons and polarons on the infrared absorption of cadmium oxide, *Solid State Commun.* **7** (1), 11--14, 1969.
14. Schaack, G. & Uhle, N. Raman spectra in doped cadmium oxide, *Solid State Commun.* **19** (4), 315--318, 1976.
15. Ansari, S.A. et al. Oxygen vacancy induced band gap narrowing of ZnO nanostructures by an electrochemically active biofilm, *Nanoscale*, **5** (19), 9238--9246, 2013.
16. Lewis, I.R. & Edwards, H. *Handbook of Raman Spectroscopy: From the Research Laboratory to the Process Line*, CRC press, New York, 2001.

17. Meinhold, R.H. Studies of impure cadmium oxide semiconductors using NMR, EPR and conductivity measurements, *Phys. Chem. Solids* **48** (10), 927--934, 1987.
18. Rajkumar, N. et al. On the possibility of ferromagnetism in CdO: Mn at room temperature, *J. Exp. Nanosci.* **6** (4), 389--398, 2011.
19. Gulino, A. & Tabbi, G. CdO thin films: a study of their electronic structure by electron spins resonance spectroscopy, *Appl. Surf. Sci.* **245** (1-4), 322--327, 2005.
20. Shinde, R.F. & Date, S.K. X-band EPR studies of hyperfine and superhyperfine structure of Mn²⁺ ions in polycrystalline CdO, *Mater. Chem. Phys.* **24** (1-2), 71--81, 1989.
21. B. Santara, B. et al. Evidence of oxygen vacancy induced room temperature ferromagnetism in solvothermally synthesized undoped TiO₂ nanoribbons, *Nanoscale*, **5** (12), 5476--5488, 2013.
22. Wolff, P.A. et al. Durst, Polaron-polaron interactions in diluted magnetic semiconductors, *J. Appl. Phys.* **79** (8), 5196--5198, 1996.
23. Kaminski, A. & Sarma, S.D., Polaron percolation in diluted magnetic semiconductors, *Phys. Rev. Lett.* **88** (24), 247202--4, 2002.
24. Lu, Z.L. et al. The origins of ferromagnetism in Co-doped ZnO single crystalline films: From bound magnetic polaron to free carrier-mediated exchange interaction, *Appl. Phys. Lett.* **95** (10), 102501--3, 2009.
25. Shah, L.R. et al. Detailed study on the role of oxygen vacancies in structural, magnetic and transport behavior of magnetic insulator: Co-CeO₂, *J. Phys. Condens. Matter.* **21** (48), 486004--9, 2009.
26. Coey, J.M. et al. Donor impurity band exchange in dilute ferromagnetic oxides, *Nat. Mater.* **4**, 173--179, 2005.
27. Coey, J.M.D. et al. Ferromagnetism in Fe-doped SnO₂ films, *Appl. Phys. Lett.* **84** (8), 1332--1334, 2004.
28. Caldero'n, M.J. & Sarma, S.D. Theory of carrier mediated ferromagnetism in dilute magnetic oxides, *Ann. Phys.* **322** (11), 2618--2634, 2007.
29. Wang, C. et al. Effects of oxygen pressure on lattice parameter, orientation, surface morphology and deposition rate of (Ba_{0.02}Sr_{0.98})TiO₃ thin films grown on

Chapter V

MgO substrate by pulsed laser deposition, *Thin Solid Films* **485** (1-2),82--89, 2005.

**Chapter VI: Luminescence and Magnetic properties of
Pure Diatom Frustules and Diatom Frustules with
CdO Nanoparticles**

6.1 Luminescence properties of nanoporous fresh water Diatom

Diatoms are unicellular, eukaryotic, photosynthetic algae that are found in various environments including both fresh and marine water. These are 1–500 μm in length with characteristic rigid cell walls (frustules) composed of silica as described in section 1.5.1 of chapter I. These organisms are found in a wide variety of habitats and are thought to be responsible for up to 25 % of the world's net primary production of organic carbon. Fresh water Diatom frustules show special optical properties. Fresh water diatom *Cyclotella Meneghiniana* shows unique luminescence properties. To ensure the morphological properties scanning electron microscopy (SEM) was done. X-ray diffraction (XRD) studies were carried out to see the structural properties of the frustules which along with EDX confirm that silica is present in diatom frustules. This silica crystallizes in alpha quartz structure. Study of optical properties of the silica frustules of diatom using Ultraviolet-Visible (UV-Vis) absorption spectroscopy, PL spectroscopy confirmed that diatom *Cyclotella Meneghiniana* show luminescence in the blue region of the electromagnetic spectrum when irradiated with UV light. This property of Diatom can be exploited to get many applications in day to day life. Also from time resolved photoluminescence spectroscopy (TRPL), it is confirmed that these species of Diatom show bi-exponential decay.

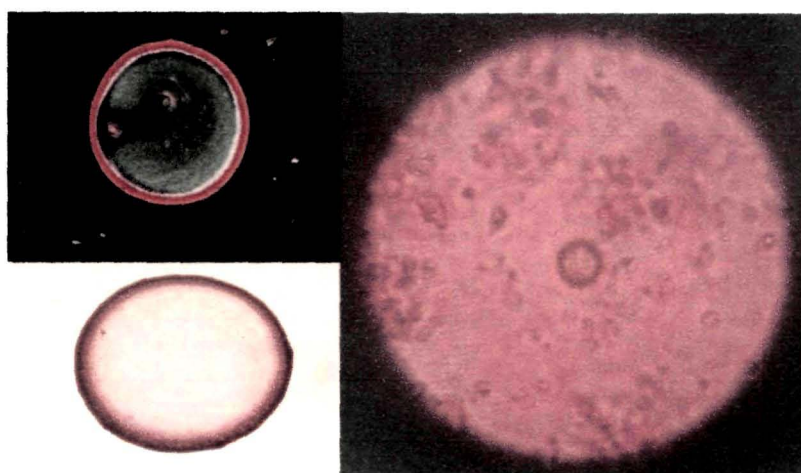


Figure 6.1: Images of fresh water Diatom taken by Optical microscope

6.1.1 Culture of Diatoms

Living diatom cells were collected from a pond in Tezpur. The samples revealing the presence of diatom like structure is taken by compound microscope as shown in Figure 6.1. The samples were centrifuged to 9000 rpm for 10 minutes. The heavy particles were allowed to sediment. The precipitate was suspended in 1 ml of PBS buffer to remove the artifacts to improve resolutions. The pellet was again dissolved in distilled water. The cells were cultured using W.C. medium of Guillard and Lorenzen [1]. The samples are kept in B.O.D. incubator under controlled condition of temperature (23 °C) and photoperiods of 16 hour dark and 8 hour bright. The protocol was slightly modified by doubling the composition of sodium metasilicate and lowering the pH from 7 to 6.23. To analyze the diatom frustules, a cleaning procedure is needed that removes the external organic matrix covering the frustules. In this work, this was done by using the acid procedure. Many methods have been developed to do this (Hassle 1978, Krammer and Lange-Bertlot 2000) some of these have some advantages and disadvantages. Acid treatment is a common method for removing all organic matrixes of the cell. Following steps were done in this procedure:

- Culture flask was shaken for 5 minutes to detach all diatoms;
- 10 ml of sample was centrifuged at 5000 rpm for another 10 min;
- The pellet was washed in double distilled water three times to remove the excess of fixative;
- 37 % aqueous HCl was added and centrifuged at 3000 rpm for 10 minutes and was put in water bath for 15 min at 60 °C;
- The acid was pipetted and pellet was washed again in double distilled water 3 times. Cleaned frustules valves were then stored in ethanol to avoid contamination and bacteria growth.

Cleaned frustules valves were then stored in ethanol to avoid contamination and bacteria growth. SEM images were taken by JEOL, JSM-6390LV, INCAx-sight EDX detector.

XRD patterns were collected by using Rigaku Miniflex diffractometer with $\text{CuK}\alpha$ radiation ($\lambda=1.5405 \text{ \AA}$). UV-Vis absorption spectroscopy was performed by Shimadzu 2450 Ultra violet visible spectrophotometer. PL spectroscopy was done by Perkin Elmer LS 55 and time resolved PL spectroscopy by Eddinburg Instruments, Model: FSP920 were also carried out to investigate the optical properties of the fresh water diatom frustules.

6.1.2 Structural and Morphological properties

Morphological studies of Diatoms were carried out with SEM. Figure 6.2 (a) is the SEM picture of Diatom *Cyclotella Meneghiniana*. EDX analysis (Figure 6.2 (b)) showed that this species of diatom has silicon of 9.9 atomic % which is maximum among all other elements. Figure 6.1 (C) is the histogram of pore size distribution. Average pore size is found to be 63 nm.

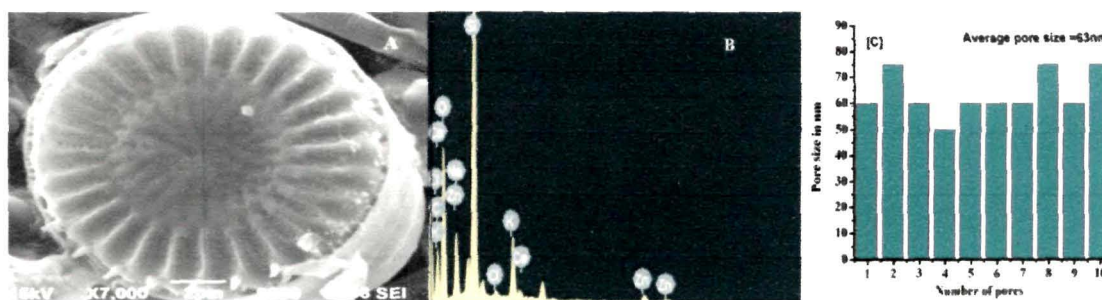


Figure 6.2: (A) SEM pictures of *Cyclotella Meneghiniana* of fresh water diatom, (B) EDX of the same species, (C) Histogram of pore size distribution

Figure 6.3 shows XRD pattern of the frustules of *Cyclotella Meneghiniana* species of diatom which confirms peaks of Alpha quartz, a crystalline form of quartz. The calculated average crystallite size is 39 nm and nanoporous silica crystallizes in tetragonal structure. In research articles, it was suggested that marine diatom frustule is composed of amorphous silica only but here in this case, peaks of alpha quartz are found in XRD pattern of fresh water diatom *Cyclotella Meneghiniana*.

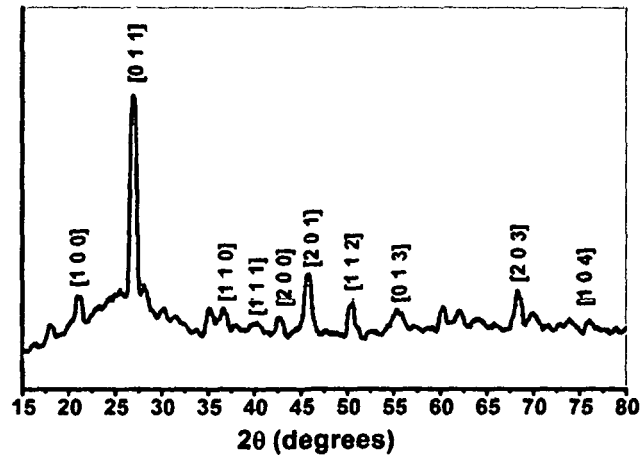


Figure 6.3: XRD pattern of diatom *Cyclotella Meneghiniana* frustules

6.1.3 Optical properties

From the ultraviolet-visible spectroscopy of the same species of diatom as shown in Figure 6.4, it is seen that this species of diatom absorb ultraviolet light with peak absorption at 274 nm.

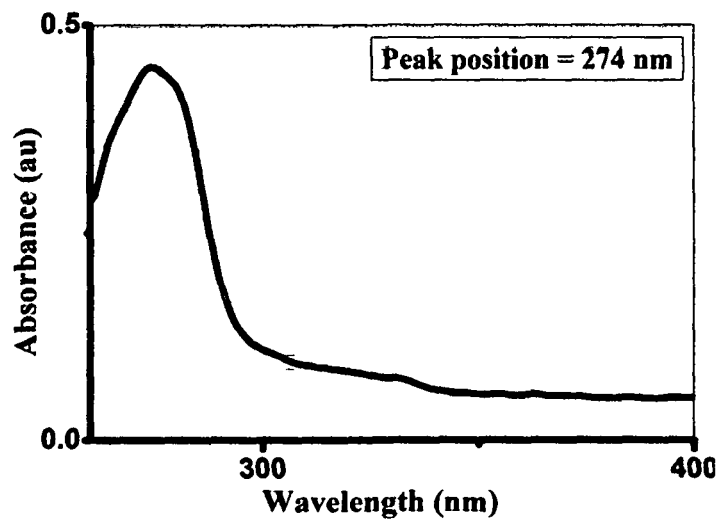


Figure 6.4: UV-Vis absorption spectroscopy of Diatom *Cyclotella Meneghiniana* frustules

In PL spectrum as shown in Figure 6.5, excitation at 4.5 eV gives rise to peak centered at 2.74 eV. Since PL properties of diatom frustules reveal similarity of properties to those of porous silicon supporting the most recent model developed for porous silicon (PS) taking into account the quantum confinement (QC) in silicon nanoparticles followed by de-excitation. This model is called QC/PL center model [2]. Quantum confinement effect is used to describe group of phenomena occurred when the diameter of the particle is of the same order of magnitude as the wavelength of the electron wave function. In that event, the optical and electronic properties of the material exhibit significant deviations from their bulk materials.

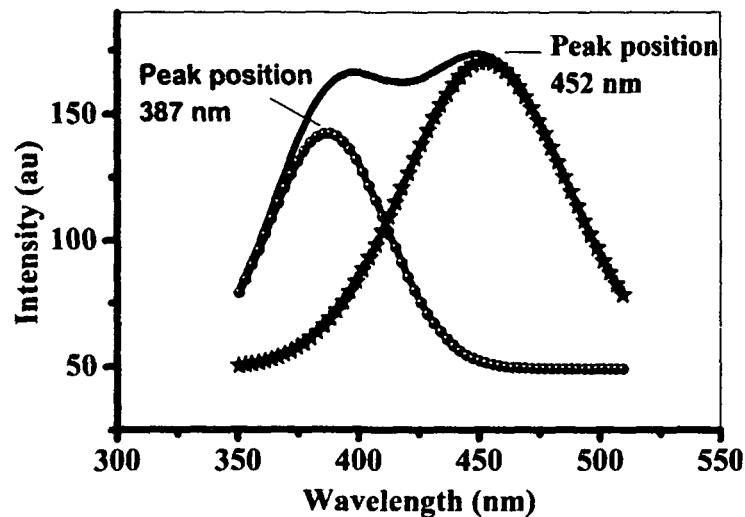


Figure 6.5: PL spectra of Diatom *Cyclotella Meneghiniana* frustules

The band gap of quantum confined nanostructures turn out to be higher than the band gap of bulk material. Consequently, 2.74 eV de-excitation observed in PL cannot be explained by band to band transition of porous silica in diatom frustules. Most possible reason for PL from diatoms with peaks at 387 nm and 452 nm are by self-trapped excitons under quantum confinement effect. The optical excitation of materials results in a sudden change of electronic charge distribution, thus generating potential well destroying the balance of interatomic forces and forming excited electrons and valence hole. The bound pair of electron and hole is referred to as the free exciton (FE). Self trapping process is caused by a localization of free exciton (FE) in the lattice which

results in excitonic energy reduction. As a result STE state occurs below the FE ones [3]. The electrons and holes can cause large distortions in the structure surrounding them. If the distortion energy is high, electrons and holes are made immovable and are self-trapped, because the self-trapped state is more stable than the one in which they would move dragging the distortions. By definition, self-trapped exciton (STE) means that the exciton becomes stabilized by localizing themselves in the potential well due to the self-induced lattice distortion. As Kanemitsu et al. suggested [4] the non-uniform and highly asymmetric size distribution of nanoparticles could be caused by a size step effect on a single atomic layer step, which is used to explain multiple PL peak in porous silicon. Since porous silicon and porous silica has similarity in property and fresh water diatom frustules consisted of porous silica it can be concluded that multiple peaks in PL as shown in Figure 6.5 is due to non-uniform crystallite size of the frustules.

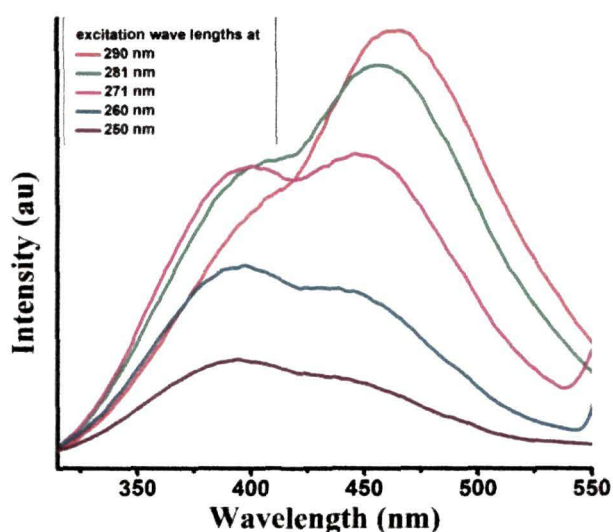


Figure 6.6: PL peak position for different excitation wavelengths

Here in the above Figure 6.6, it is seen that in case of Silica frustules, the PL peak position do not vary much with variation in excitonic wavelength. So it is possible that STE luminescence is independent of excitonic wavelength as they correspond to same energy level.

PL excitation (PLE) spectroscopy is a technique in which one monitors the intensity of light emission at a fixed wavelength as a function of the wavelength of the incident excitation light. Therefore PLE involves both absorption and recombination processes. PLE is unique in its ability to directly identify absorption mechanisms leading to the emission process of interest [5]. PLE spectra of diatom frustules are shown in Figure 6.7. Here detection wavelengths are 464 nm, 454 nm, 444 nm and 434 nm. The observed peaks show no special characteristic change except that increase in peak intensity with decrease in detection wavelength.

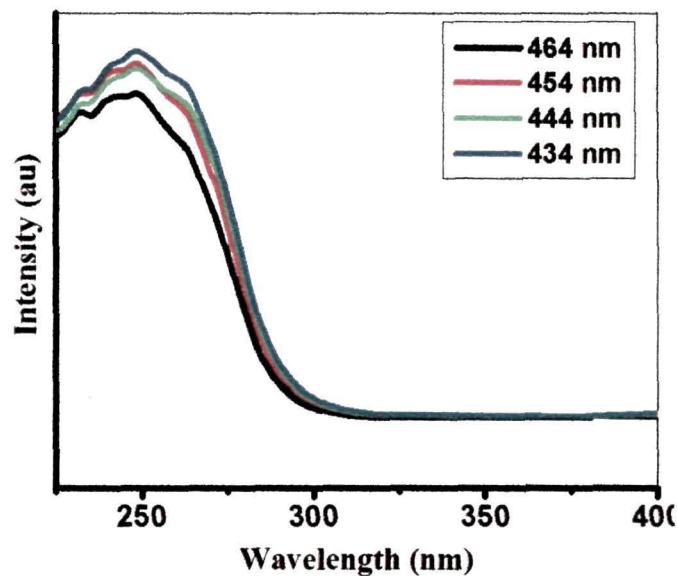


Figure 6.7: PLE spectra of Diatom *Cyclotella Meneghiniana*

Time resolved PL spectroscopy (TRPL) was taken for the same sample as shown in Figure 6.8. It was found after fitting the parameters that the decay best fits for bi-exponential decay which obeys the following law

$$I(t) = I(0)[A_1 \exp\left(-\frac{t}{\tau_1}\right) + A_2 \exp\left(-\frac{t}{\tau_2}\right)]$$

where A_1 and A_2 are amplitudes and τ_1 and τ_2 are their lifetimes. Here excitation wavelength is 271 nm and τ_1 is 5.8 ns and τ_2 is 1ns. As a system of coupled electron

spins (electron and hole), the STE has a triplet with long life time and a singlet with fast lifetime. The lifetimes of TRPL spectroscopy are due to these two components [6, 7].

Fresh water Diatom *Cyclotella Meneghiniana* shows PL in the visible range when irradiated with ultra violet light. This species of diatom has two PL peaks at the wavelengths 387 nm and 452 nm due to non uniform pore size of nanostructures in the frustules of fresh water diatom *Cyclotella Meneghiniana*. In most of the literature it is sited that diatoms have amorphous silica frustules. But the frustules of the species that has been cultured is found to be composed of crystalline alpha quartz having defects generated by self-trapped excitons as confirmed by PL and TRPL. It may be noted that this variety of uniform crystalline porous silica structures are not obtained easily by chemical synthesis.

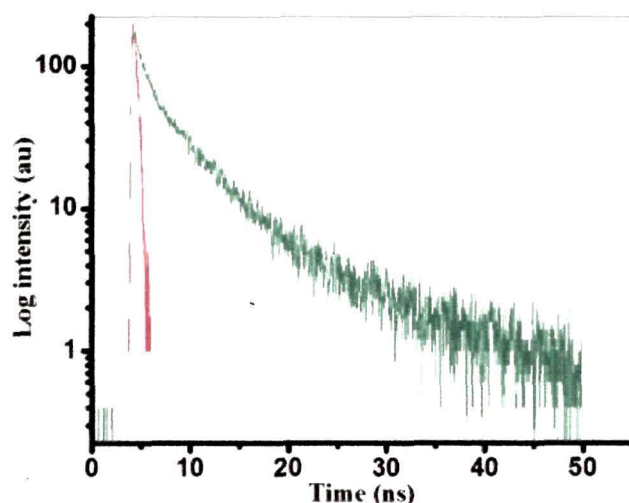


Figure 6.8: PL decay curves corresponding to emission wavelength 330 nm along with instrumental response function

6.2. Ferromagnetic CdO nanoparticles inserted in Diatom Frustules

Diatoms are unicellular microalgae that form microscale silica walls called frustules. These frustules are complex two and three dimensional nanopatterns which are species

specific [8]. These biological nanostructures display versatile morphologies and may have potential applications in solar cells [9-12], PL based biosensors [13], drug delivery systems [14], electroluminescent/photoluminescent devices [15] and selective membranes [16]. But the dielectric nature of these ornate nanopatterns has limited its use for optoelectronic device-applications. Consequently, enormous efforts have recently been given to modify the silica into technologically more suitable functional materials while preserving the frustule architecture. Frustule composition have been altered to or by functional materials such as TiO_2 , BaTiO_2 , SrTiO_2 , MgO , NiSO_4 , $\text{Zn}_2\text{SiO}_4\text{:Mn}$, $\text{Y}_2\text{SiO}_5\text{:Eu}^{3+}$ and Silicon-Germanium nanocomposites [17-23]. Diatom frustules have also been chemically modified for the attachment of antibodies for medical applications. Sol-gel process, atomic layer deposition, chemical bath deposition, inkjet printing process, biosynthesis and low-temperature magnesiothermic reaction is some of the methods that have been used to modify chemical composition of the frustule.

In this study, a simple and low cost method is used to combine diatom frustule with semiconductor nanoparticles. Combining basic materials such as Diatom frustule with semiconductor nanoparticles, change in optical properties of frustules was achieved and it will enable producing low cost light emitting devices which is economically very important. In this work, optical and magnetic properties of Silica frustules were investigated after precipitating CdO semiconductor nanoparticles of size 25 nm into the frustules. Synthesis and properties of CdO nanoparticles are discussed in chapter II, IV and VI. Especially in chapter VI, luminescence and magnetic properties of vacuum annealed CdO nanoparticles are discussed. CdO nanoparticles show enhanced luminescence and magnetic properties when these particles are dried in vacuum. So, after precipitating CdO nanoparticles onto Diatom frustules, the combined system is dried in vacuum. Before precipitation, the frustules are also dried in vacuum so that there are no air inside the pores which may prevent nanoparticles from going inside the pores. Surface of the frustules with the CdO nanoparticles are investigated by HR-TEM. Optical properties are investigated by UV-Vis absorption spectroscopy and PL spectroscopy. Till date people were trying to synthesize porous silica by chemical method and combined magnetic nanoparticles such as Iron Oxide and transition metal such as Nickel with it [24].

6.2.1 Structural and Optical properties

Transmission electron microscope image is shown in Figure 6.9. TEM images are taken by TEM Model: JEM-100 CX II with specific resolution of 3 Å to 1.4 Å. In the image it can be seen that nanoparticles are precipitated there inside the pores.

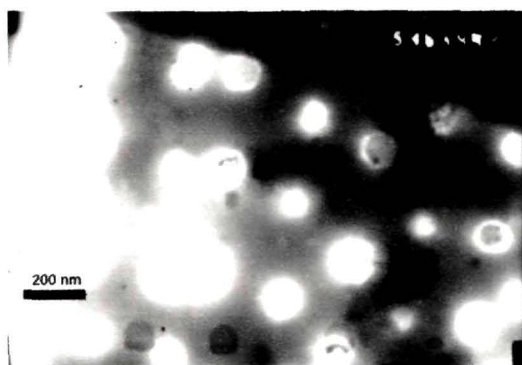


Figure 6.9: TEM image of Diatom frustules with CdO nanoparticles

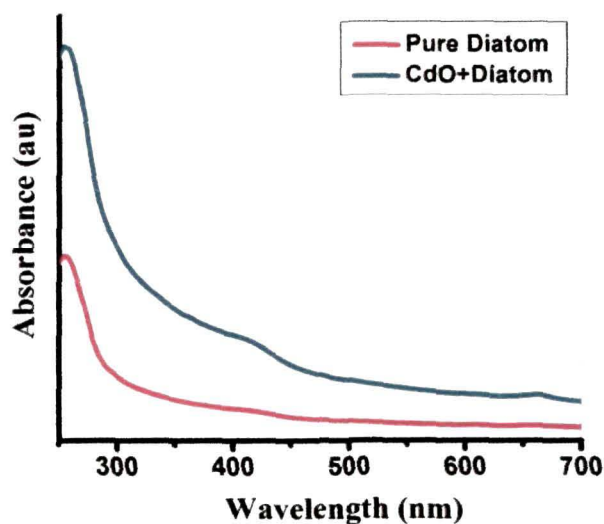


Figure 6.10: UV-Vis absorption Spectra of Diatom Frustules with and without CdO nanoparticles

Comparison between absorption spectra of pure diatom frustule and frustules containing CdO nanoparticles is shown in Figure 6.10. Pure diatom frustule shows absorption peak at 270 nm. There is specific peak due to CdO nanoparticles which shows absorption at around 370 nm. PL spectra of the same are shown in Figure 6.11.

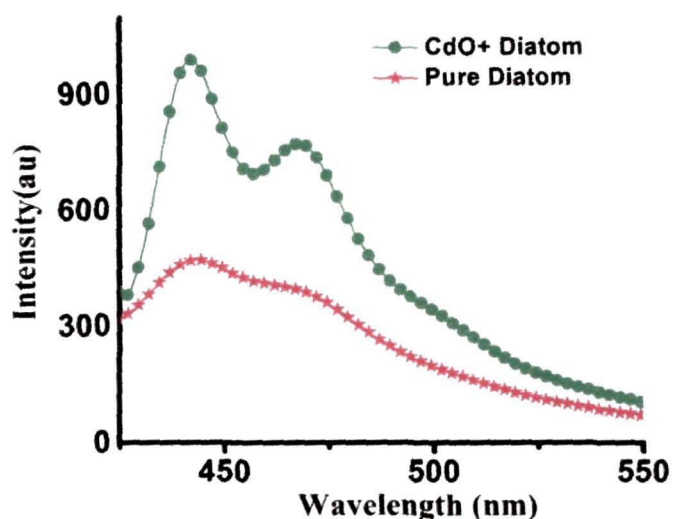


Figure 6.11: Comparison of PL spectra of Diatom Frustules with and without CdO nanoparticles

From PL spectroscopy as shown in Figure 6.11, it can be seen that blue luminescence intensity of diatom frustules with nanoparticles is increased to a great extent than that of pure diatom frustules. Pure diatom frustules show blue luminescence peak which actually consists of two peaks. This increase in luminescence intensity of the combined structure may be attributed to increase in scattering of light inside the pores which lead to increase in luminescence intensity of the frustules. The observed blue luminescence peaks for pure diatom frustules is ascribed to self trapped excitons (STE) as explained earlier. CdO nanoparticles do not show good luminescence intensity but inserting them into the Diatom frustules increase luminescence intensity of the frustules. Although extra peak due to the nanoparticles was not found but their presence inside the pores increases luminescence intensity of the combined structure.

6.2.2 Study of Magnetic property

Magnetic measurements are performed by SQUID magnetometer. Magnetic hysteresis (M-H) loops at room temperature for pure diatom frustules and diatom frustules with CdO nanoparticles are shown in Figure 6.12. Both samples show ferromagnetism at room temperature. Coercive fields for pure diatom frustules and the combined structures were found to be 100 Oe and 232 Oe and the saturation magnetization (M_s) values for both the samples are found to be 0.0001 emu/gm and 0.17 emu/gm respectively.

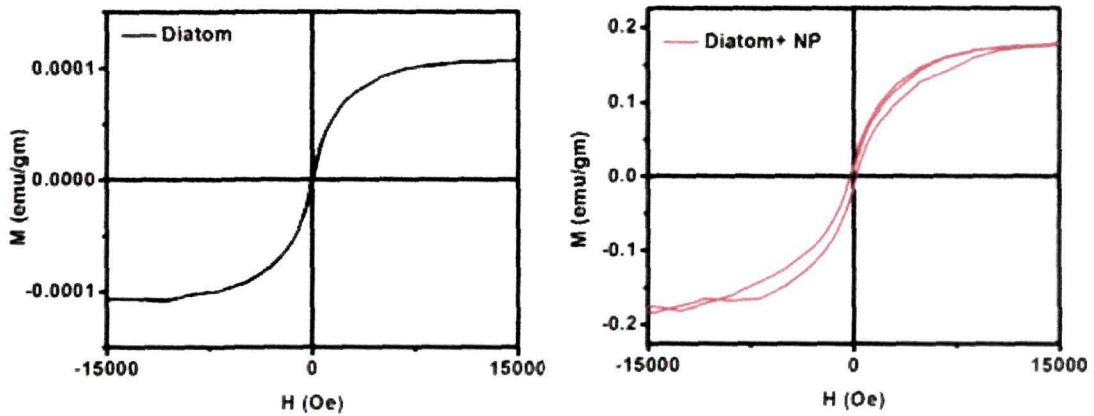


Figure 6.12: M-H curve for Pure Diatom frustules and Diatom frustules with CdO nanoparticles

With insertion of ferromagnetic CdO nanoparticles, the saturation magnetization and coercivity of pure Diatom porous silica increased to a great extent. This may be due to insertion of ferromagnetic CdO nanoparticles.

6.3. Conclusion

Culture of fresh water nanoporous diatom *Cyclotella Meneghiniana* was explained showing PL in the visible range when irradiated with ultra violet light. The important and novel findings in our work which are summarized in the following points:

Chapter VI

- This species of diatom has two PL peaks at the wavelengths 387 nm and 452 nm due to non uniform pore size of nanostructures in the frustules of fresh water diatom *Cyclotella Meneghiniana*.
- In most of the literature it is sited that diatoms have amorphous silica frustules. But the frustules of the species that has been cultured is found to be composed of crystalline alpha quartz having defects generated by self-trapped exciton as confirmed by PL and TRPL.
- A simple and cost effective method was proposed to combine basic material such as diatom frustules with nanoparticles. The combined structure of diatom frustules with CdO nanoparticles shows good luminescence properties as well as good magnetic properties. This kind of combined structure is studied for the first time.

References:

1. Guillard, R.R.L. & Lorenzen, C.J. Yellow-Green algae with chlorophyllide C, *J. Phycol.* **8** (1), 10--14, 1972.
2. Qin, G.G. & Jia, Y.Q. Mechanism of the visible luminescence in porous silicon, *Solid State Commun.* **86** (9), 559--563, 1993.
3. Glinka, Y.D. et al. Size effect in self-trapped exciton PL from SiO₂-based nanoscale materials, *Phys. Rev. B* **64**, 085421--11, 2001.
4. Kanemitsu, Y. et al. On the origin of visible PL in nanometer-size Ge crystallites, *Appl. Phys. Lett.* **61** (18), 2187--2189, 1992.
5. Feng, Z.C. Tsu, R. (ed.) *Porous silicon*, World Scientific, Singapore, 1994.
6. Kobitski, A.Y. Self-trapped exciton recombination in silicon nanocrystals, 2001, *Phys. Rev. B* **63**, 115423--5, 2001.
7. Glinka, Y.D. Time-resolved PL study of silica nanoparticles as compared to bulk type-III fused silica, *Phys. Rev. B* **66**, 035404--10, 2002.

8. Werner, D. *The Biology of Diatoms*, University of California Press, Berkeley, 1977.
9. Jiang, H. et al. PL Properties of ZnSe/SiO₂ Composite Thin Films Prepared by Sol-gel Method, *T. Nonferr. Metal. Soc.* **16**, 266--269, 2006.
10. Fan, S.Q. et al. Highly efficient quantum-dot-sensitized TiO₂ Photoelectrodes for Solar Cell Applications, *Electrochem. Commun.* **11**(6), 1337--1339, 2009.
11. Reiss, P. et al. Low Polydispersity Core/shell Nanocrystals of CdSe/ZnSe and CdSe/ZnSe/ZnS Type: Preparation and Optical Studies, *Synthetic Met.* **139** (3), 649--652, 2003.
12. Chen, J. et al. An Oleic Acid-capped CdSe Quantum-dot Sensitized Solar Cell *Appl. Phys. Lett.* **94** (15), 153115--2, 2009.
13. Song, M.K. et al. Nanostructured electrodes for lithium-ion and lithium-air batteries: the latest developments, challenges, and perspectives, *Mater. Sci. Eng.* **72** (11), 203--252, 2011.
14. Gale, D.K. et al. PL detection of biomolecules by antibody-functionalized diatom biosilica, *Adv. Funct. Mater.* **19** (6), 926--933, 2009.
15. Zhang, Y. et al. Development of a micro-swimming robot using optimized giant magnetostrictive thin films, *Appl. Bionics Biomech.* **3** (3), 161--170, 2006.
16. Jeffryes, C. et al. Electroluminescence and PL from nanostructured diatom frustules containing metabolically inserted Germanium, *Adv. Mater.* **20** (13), 2633--2637, 2008.
17. Dudley, S. et al. Conversion of SiO₂ diatom frustules to BaTiO₃ and SrTiO₃, *J. Am. Ceram. Soc.* **89** (8), 2434--2439, 2006.
18. D. Losic, D. et al. Controlled pore structure modification of diatoms by atomic layer deposition of TiO₂, *J. Mater. Chem.* **16** (41), 4029--4034, 2006.
19. Weatherspoon, M.R. et al. Sol-gel synthesis on self-replicating single-cell scaffolds: applying complex chemistries to nature's 3-D nanostructured templates, *Chem. Commun.* (5), 651--653, 2005.
20. Townley, H.E. et al. Modification of the physical and optical properties of the frustule of the diatom *Coscinodiscus wailesii* by nickel sulfate, *Nanotechnology*, **18** (29), 295101--5, 2007.

Chapter VI

21. Cai, Y. et al. Three-dimensional magnesia-based nanocrystal assemblies via low-temperature magnesiothermic reaction of diatom microshells, *J. Am. Ceram. Soc.* **88** (7), 2005--2010, 2005.
22. Lee, D.H. et al. Nanofabrication of green luminescent ZnSiO₄: Mn using biogenic silica, *Electrochem. Solid-State Lett.* **10** (7), 13--16, 2007.
23. Jeffryes, C. et al. Two-stage photobioreactor process for the metabolic insertion of nanostructured germanium into the silica microstructure of the diatom *Pinnularia* sp, *Mat. Sci. and Eng. C* **28** (1), 107--118, 2008.
24. Granitzer, P. et al. Magnetic Nanoparticles Embedded in a Silicon Matrix, *Materials* **4** (5), 908--928, 2011.

Chapter VII: Concluding remarks and future directions

7.1 Thesis Conclusion

The salient points found in this thesis are:

1. CdSe nanoparticles can be synthesized by a one pot synthesis method without inert atmosphere. They show good luminescence properties. But to gain both good luminescence and magnetic properties in the same material is a challenge for us. Transition metal doping in II-VI semiconductor nanoparticle like CdSe is an exigent task. Manganese was doped into CdSe in diluted amounts that are in 1 %, 2.5 % and 5 % molar concentrations. For 1 % doping concentration, manganese ions are well incorporated inside the CdSe lattice as evidenced by X-ray diffraction (XRD) and photoluminescence (PL) spectra. Since Mn^{2+} doped CdSe nanoparticles with diameter higher than 3.3 nm do not show pseudo-tetrahedral Mn^{2+} (${}^4\text{T}_1 \rightarrow {}^6\text{A}_1$) transitions, Mn^{2+} related luminescence is not obtained. It is observed that presence of Mn dopants leads to partial quenching of luminescence intensity. The reason behind partial quenching of photoluminescence intensity is the shrinking distance between Mn-Mn. For 5 % doping concentration, dopants are not properly incorporated inside the lattice. So it was found that not all dopant concentrations are able to be doped into host. This is because of a phenomenon called self purification for which CdSe nanoparticles expels dopants.
2. EPR spectroscopy of 1 % manganese doping in CdSe nanoparticles is actually composed of two spectra with a hyperfine structure with six lines and a broad spectrum. The smaller Mn^{2+} ion is expected to distort the CdSe lattice by replacing Cd^{2+} . The EPR data suggest that the Mn site is trigonally or tetragonally distorted which leads to the observation of forbidden EPR transitions. A broadening effect is seen with increase in Mn concentration. This broadening effect with increase in Mn concentration is due to Mn-Mn interaction.
3. Room temperature ferromagnetism is found in CdMnSe samples. Origin of ferromagnetism in Mn doped CdSe is attributed to F-centre mediated exchange

Chapter VII

mechanism. An F-centre is a selenium vacancy with a trapped electron. This trapped electron occupies an extensive orbital state that overlaps with the d shells of some nearby transition metal atoms. The radius of this trapped electron orbital is predictable to be of the order of a_0 , where a_0 is the Bohr radius. This pair is called bound magnetic polaron (BMP). The BMP will align in a parallel arrangement with the surrounding individual dopant ion spins by sp-d exchange interaction.

4. pH of the precursor solution of CdSe nanoparticles was varied to see the changes incurred. It was found that for pH 11, CdSe nanoparticles show highest luminescence. CdSe nanoparticles are coated by organic capping agent Thioglycolic acid (TGA). From PL and Fourier transform infrared (FTIR) spectra, it is confirmed that at pH levels of 8, 9, 10, some of the TGA molecules may depart from the CdSe nanoparticles into the solvent until a dynamic equilibrium is established between the adsorbing and desorbing of TGA from the NPs surfaces. At pH 11, this dynamic equilibrium is established. And that is why at this pH, crystallinity is found in CdSe nanoparticles.
5. Among all other II-VI semiconductors, CdO fall in the group of transparent conducting oxides also. On the contrary to CdSe nanoparticles, CdO nanoparticles do not show good luminescence properties. Good luminescence was found in CdO nanoparticles by annealing them in vacuum environment. Annealing in vacuum leads to creation of more and more oxygen vacancies. Increase in number of oxygen vacancies is responsible for enhanced green luminescence in CdO nanoparticles.
6. Changes in the properties of CdO nanoparticles were seen by varying the annealing temperature in air. It has been found that with increase in temperature cadmium interstitials which are Frenkel defects and unstable move towards the surface and after getting enough energy they get oxidized. So, blue luminescence intensity corresponding to Cd-interstitials decreases with rise in temperature. On the contrary, number of oxygen vacancies increase with rise in temperature, so

green luminescence intensity corresponding to oxygen vacancies increase with ascending temperature. Also, since F^{2+}/F^+ centres are present in the samples so with rise in temperature, electrons trapped in oxygen vacancies get sufficient energy and become free electrons with rise in temperature. Hence conductivity and charge density increase with rise in temperature.

7. EPR spectra show presence of Cd^+ ions in pure CdO nanoparticles. These ions were formed from Cd^{2+} ions formed by F^{2+} centres by donating one electron to their neighboring Cd^{2+} centres. From the broad EPR peak in vacuum annealed nanoparticles, one can conclude increase in Cd^+ ions in the system which again indicates increase in oxygen vacancies. Origin of ferromagnetism in CdO nanoparticles can be attributed to bound magnetic polaron (BMP) model. These BMPs are formed by Cd^+ ions with F^+ centres. Increase in number of BMPs in the system lead to ferromagnetism in CdO nanoparticles.
8. Incorporation of manganese in the host CdO nanoparticles leads to decrease in band gap. Also there is a partial quenching of luminescence intensity due to Auger non-radiative transitions. There are no secondary oxide phases of manganese in the manganese doped CdO nanoparticles. The origin of room temperature ferromagnetism can be assigned to formation of bound magnetic polarons.
9. Analyzing both pristine and doped CdSe and CdO nanoparticles, it was found that vacuum annealed CdO nanoparticles show enhanced luminescence as well as magnetic properties. Insertion of these nanoparticles into diatom frustule which are made up of porous silica can bring new possibilities of manufacturing devices like low cost light emitting diodes. This species of diatom has two PL peaks at the wave lengths 387 nm and 452 nm due to non uniform pore size of nanostructures of Diatom porous silica (DPS). In most of the literature, is sited that DPS has amorphous silica frustules. But the frustules of the species that has been cultured is found to be composed of crystalline alpha quartz having defects

generated by self-trapped exciton as confirmed by photoluminescence spectra and time resolved photoluminescence spectra. A simple and cost effective method was proposed to combine basic material such as DPS with nanoparticles. The combined structure of diatom frustule with CdO nanoparticles shows good luminescence properties as well as good magnetic properties.

7.2 Future directions

CdO and CdSe nanoparticles have been used in many applications like light-emitting diodes, lasers etc and as transparent conducting oxide in LED, LCD and solar cell applications respectively. Pure CdSe nanoparticles show enhanced luminescence. But to get both good optical and magnetic properties in the same system is a challenge. Band gap was modified by incorporating transition metal in CdSe. But incorporation of transition metal leads to partial quenching of luminescence. Next to get luminescence and magnetic properties in CdO nanoparticles which do not have good luminescent properties, manganese was incorporated in it. It was found that luminescence intensity of CdO nanoparticles in the case of manganese incorporation is also reduced. CdO nanoparticles show enhanced luminescence only when these particles are annealed in vacuum. Increase in the number of oxygen vacancies lead to changes in optical and magnetic properties. Both visible luminescence and ferromagnetism were found in these vacuum annealed CdO nanoparticles. Researchers have been trying hard to make nanoporous silica structures till date by various methods. But such structures are abundant in nature itself and are easily available in sea and fresh water. Porous silica containing nanoparticles are especially important because of their numerous practical applications like low cost light emitting devices [1, 2]. A detail analysis on the defects present in CdO nanoparticles and DPS will be carried out using deep-level transient spectroscopy in future. And to know other material properties of both CdO nanoparticles and DPS, spectroscopic ellipsometry will also be done. The combined structure of CdO nanoparticles and DPS shows enhanced optical and magnetic properties. Thorough studies of

Chapter VII

magnetic and optical properties of the combined structure of DPS and other nanoparticles will be carried out in future.

References:

1. Jarimavičiūtė-Žvalionienė, R et al. Photoluminescence Properties of Porous Silicon with CdSe/ZnS Quantum Dots, *Mater. Science*, **17** (3), 1392--1320, 2011
2. Gutu, T et al. Electron Microscopy and Optical Characterization of Cadmium Sulphide Nanocrystals Deposited on the Patterned Surface of Diatom Biosilica, *J. of Nanomat.*, **2009**, 1--7, 2009

List of publications

Papers published

1. B. Goswami, A. Choudhury, Alak K. Buragohain, Luminescence properties of a nanoporous freshwater diatom, *Luminescence*, 27 (1), 16--19, 2012.
2. B. Goswami, A. Choudhury, Dopant induced changes in optical and structural properties of Cadmium Selenide nanoparticles, *International Conference on Advanced Nanomaterials and Emerging Engineering Technologies (ICANMEET)*, IEEE, Chennai, 2013.
3. Enhanced visible luminescence and modification in morphological properties of Cadmium Oxide nanoparticles induced by annealing, *Journal of experimental nanoscience*, DOI:10.1080/17458080.2014.933492, 2014

Papers communicated/accepted

1. Oxygen Vacancy generated Room Temperature Ferromagnetism and Optical Properties of CdO Nanoparticles (accepted)
2. Modulation of Optical properties of CdSe nanoparticles by varying synthesis conditions (communicated)
3. Magnetic properties of Manganese Doped CdSe nanoparticles (communicated)

International Conferences

1. Poster presented in International conference on Advanced Nanomaterials and Nanotechnologies-2009 (ICANN-2009)
2. Poster presented and full paper submitted in 4th International conference on Recent Advances in Composite Materials-2013 (ICRACM-2013)

National Conferences

1. Poster presented in National Seminar on Photonics and Quantum Structures'09, TU, ASSAM.
2. Poster presented in National Conference on smart Nanostructures'2011
3. Poster presented in National Workshop on Nuclear and Atomic Techniques based Pure and Applied Sciences'2011

Seminars attended:

1. Condensed Matter Days 2006 held in Tezpur University, Assam.
2. OSI annual conference 2007 held in Tezpur University, Assam.